Title
Registration of Musculoskeletal Images for the Analysis of Bone Structure

Author
Goldenstein, Janet Helene

Publication Date
2009

Peer reviewed|Thesis/dissertation

Registration of Musculoskeletal Images for the Analysis of Bone Structure

by

Janet Helene Goldenstein

DISSERTATION

Submitted in partial satisfaction of the requirements for the degree of

DOCTOR OF PHILOSOPHY

in

Bioengineering

in the

GRADUATE DIVISION

of the

UNIVERSITY OF CALIFORNIA, SAN FRANCISCO

AND

Acknowledgments

I would like to express deep gratitude to my advisor, Dr. Sharmila Majumdar, for her support of my work, for being a wonderful role model, and for giving me the freedom to explore the research topics that most interested me. I would also like to thank the other members of my dissertation committee, Dr. Colin Studholme and Dr. Thomas Link, whose time and effort is gratefully acknowledged. Dr. Thomas Link provided useful and interesting practitioner insights that ensured my research was practical and clinically relevant. Dr. Colin Studholme provided a much needed resource for my image processing questions and he dedicated many hours to discussing technical nuances that enabled my research to be more technically precise.

I feel extremely privileged to have worked in the Musculosketal and Quantitative Imaging Research group (MQIR) at UCSF. It is a truly unique group, where researchers from different backgrounds can collaborate in an encouraging and ethical environment and where the pursuit of excellence fuels success and not competition. Thank you to Gabby Blumenkrantz, whose encouragement and support, especially during the early years of the project, are greatly appreciated. Thank you to Dr. Julio Carballido-Gamio, who spent many hours scanning alongside me to help get my first abstract accepted and my first paper published and who served as a research mentor until I felt comfortable enough to independently pursue research questions. Thank you to Dr. Roland Krug, Miki Sode, Andrew Burghardt, Dr. Jin Zuo, Dr. Dana Carpenter, Dr. Suchandrima Banerjee, Karl Saldanha, Bryan Hermannsson, Dr. Xiaojuan Li, Dr. Richard Souza, Joe Schooler, Daniel Kuo, Jason Crane, and Eugene Ozhinsky for making day-to-day research life more enjoyable and conference trips more memorable, as well as providing support,

cooperation, and discussions. Thank you to “Julio’s Angles,” Ana Rodriguez and Dr. Jenny Folkesson, for adding a “feminine touch” to the image processing group. Thank you to Dr. Galateia Kazakia for providing me with additional mentorship and for being an exceptional role model.

Thank you to my qualifying committee, including Dr. Ruzena Bajcsy and Dr. Sarah Nelson, whose time and effort ensured my research was well thought out. A special thanks to Dr. Steve Conolly, who not only served on my qualifying committee, but spent many hours teaching me the basics of MR, discussing the medical imaging industry, and providing support and encouragement during those moments it was most needed.

Many thanks to my parents, Sharon and Dennis, and brother, Stephen, for their encouragement in my technical pursuits. I would like to especially thank my father, who nurtured my scientific curiosity by sharing his. Thank you to my husband, Jonathan, who provides unyielding encouragement and support despite not entirely understanding my dissertation.

Writing these acknowledgements causes me to realize how many people I rely on each day to succeed and I feel truly grateful to have them all of the in my life.

Funding for this thesis project was provided by a grant from Merck & Co and NIH grant award program numbers ROI-AR49701 and ROI-AG017762. Graduate student funding was provided by an ARCS Foundation Fellowship, an UCSF Graduate Dean's Health Science Fellowship, and an Evnin-Wright Fellowship.

Abstract

Registration of Musculoskeletal Images for the Analysis of Bone Structure

By
Janet Helene Goldenstein

The accurate and early diagnosis of osteoporosis and the assessment in response to therapy are critical for patient management but still remain a challenge for clinicians. There have been recent advancements in diagnostic imaging techniques to improve the assessment of bone quality. There are several different imaging techniques which can be used for the assessment of bone quality both in vivo and in vitro including multi-detector Quantitative Computed Tomography (QCT), High Resolution peripheral Quantitative Computed Tomography (HR-pQCT), Micro Computed Tomography (μCT), Synchrotron Radiation Micro Computed Tomography(SRμCT), and Magnetic Resonance Imaging (MRI) which each have advantages and limitations. The purpose of this thesis is to develop robust image registration techniques for CT and MR-based musculoskeletal images and determine if there is an improvement in the accuracy of longitudinal studies or an enhancement in the understanding of bone quality by combining images from different imaging techniques.

An automatic inter-modal rigid registration method based on normalized mutual information was implemented to allow for the direct spatial comparison of tissue mineralization distributions of ex vivo bone tissue specimens in μCT and SRμCT images. The registration method successfully aligned images acquired using μCT and SRμCT in five specimens of the femoral head, four specimens of the vertebral body, and five

specimens of the proximal tibia. This allowed the first direct comparison of tissue mineral density (TMD) between the two modalities.

A normalized mutual information registration method was applied to a set of 49 radius images and 51 tibia images of postmenopausal osteopenic women acquired on MRI and HR-pQCT. The registration method successfully registered all images and the robustness of the method was established. The amount of cortical porosity identified in the HR-pQCT images that contained bone marrow as visualized on the MR images was then quantified.

Image registration methodologies to align MR images in longitudinal studies were also developed. An automatic registration method based on a mutual information measure was implemented for the alignment of high-resolution MR images of trabecular bone in vivo. The robustness and reproducibly of the registration method was established on MR images of the proximal femur of six normal healthy volunteers. The improvement in measurement accuracy in a longitudinal study was demonstrated on MR images of the proximal femur of twenty-four postmenopausal osteopenic women who were scanned at 0 and 12 months.

The automatic registration method was then extended to prospective registration that allowed follow-up images to be acquired in the same orientation as baseline images. The feasibility of prospective registration for MR images of trabecular bone was demonstrated on the distal tibia of five volunteers and the knee of one volunteer. The prospective registration ensured that the same region was analyzed in both the baseline and follow-up images, saved post processing time, preserved the reproducibility of the trabecular bone parameters, and required no interpolation.

The results of this project suggest that the adoption of image registration into the analysis of musculoskeletal images of bone improves the accuracy, reproducibility, and precision of longitudinal and comparative studies.

Table of Contents

List of Tables

List of Figures

Chapter 1

Introduction

1.1 Motivation

Bone quality encompasses trabecular bone and cortical bone architecture, bone turnover, damage accumulation (micro-damage), and mineralization(1). It is an essential component in determining bone strength. Therefore bone quality is an important parameter in the diagnosis of Osteoporosis, a metabolic disease characterized by low bone mass and structural deterioration of bone tissue resulting in bone fracture(2). Because the medical and financial toll of Osteoporosis is likely to increase over the next 20 years as the population of the United States ages, noninvasive assessment of bone quality has recently received considerable attention. By 2025, the number of fractures and the associated costs are predicted to rise by 48%, to more than 3 million fractures at a cost of $25.3 billion(3). However, the advancement of diagnostic imaging techniques to assess bone quality will help with early diagnosis as well as the evaluation of the efficacy of treatment and preventative therapies.

The evaluation and monitoring of bone quality is an important part of assessing fracture risk. Patterns of change in trabecular and cortical bone can be indicative of disease state or progression. Monitoring these patterns provides useful information to further the understanding of disease processes, to improve the accuracy of early diagnosis, and to assess the efficacy of disease treatment.

Assessment of bone fracture risk and diagnosis of Osteoporosis is currently performed using areal bone mineral density (BMD) derived from Dual Energy X-ray Absorptiometry (DXA)(4). However, BMD alone does not entirely predict bone fracture

and does not adequately explain the efficacy of new treatments(5,6). Several imaging methods exist for analyzing both in vivo and ex vivo bone quality beyond BMD, such as high-resolution Magnetic Resonance Imaging (MRI), micro–Computed Tomography (μCT), Synchrotron Radiation micro-Computed Tomography (SRμCT), and High-Resolution peripheral Quantitative Computed Tomography (HR-pQCT). Each of these imaging methods has unique advantages and limitations. SRμCT and μCT are limited to ex vivo examinations while MRI and HR-pQCT are in vivo techniques. SRμCT provides an ex vivo non-invasive method for determining bone tissue mineral density (TMD) but due to its cost and scarcity of these SR facilities, it is often inaccessible to researchers. μCT is a conventional desktop system that also allows for the ex vivo non-invasive assessment of TMD, but additional analysis is required to assess its robustness. HR-pQCT is an emerging technique that allows for the direct visualization of bone at a very high resolution but cannot visualize soft-tissue and is restricted to peripheral skeletal sites. MRI results in superior soft tissue contrast without ionizing radiation, but only has an indirect visualization of bone at a lower resolution.

Image registration, the alignment of images, allows researchers to more accurately compare these different imaging modalities to establish accuracy, efficiency, and robustness of each. In addition, image registration combines the unique information obtained from each imaging method to help enhance the understanding of disease processes.

Image registration also improves the accuracy of longitudinal studies. High resolution MR images of trabecular bone is an established non-invasive three dimensional technique(7-9). The ability to distinguish between osteoporotic and non-

fracture population based on MR image derived trabecular bone parameters have been reported in literature for a large number of studies(7,10-12). To achieve efficient longitudinal monitoring of trabecular bone changes due to disease progression or treatment, it is often desirable to accurately measure small amounts of structural change with short inter-scan intervals (typically months or years). This requires accurate and reliable methods of measuring small trabecular bone structural changes under conditions of anatomical variation, such as the inherent trabecular heterogeneity within an anatomical site. Image registration can improve the accuracy of longitudinal studies involving MR images of trabecular bone by ensuring that the same anatomical region is analyzed at different time points.

1.2 Thesis Aims and Contributions

The purpose of this thesis is to develop robust image registration methodologies for musculoskeletal images and determine if there is an improvement in the accuracy of longitudinal studies or an enhancement in the understanding of bone quality by combining images from different imaging techniques.

The primary contributions of the thesis include:

1) To demonstrate the application of image registration for the direct comparison of ex vivo μCT and SRμCT tissue mineral density (TMD) values
2) To develop a method of combining HR-pQCT and MR images using image registration to identify cortical porosity containing bone marrow in the tibia and radius of a clinical study group of osteopenic women

3) To implement and optimize an automatic registration method that provides an accurate image registration solution for the alignment of serial high-resolution trabecular bone images
4) To demonstrate the improvement in the accuracy of trabecular bone changes in the proximal femur using a clinical study group of osteopenic women
5) To develop a prospective registration methodology to acquire follow-up musculoskeletal MR images in the same orientation as baseline images

1.3 Chapter Organization

The remainder of the thesis is organized as follows:

Chapter 2 provides background on osteoporosis and bone strength, methods for imaging bone anatomy, and image registration.

Chapter 3 presents the alignment of ex vivo μCT and SRμCT images for a direct voxel to voxel comparison of TMD measurements.

Chapter 4 presents a new analysis for cortical porosity by using image registration to combine HR-pQCT and MR images of the distal tibia and distal radius in a clinical study group of osteopenic women.

Chapter 5 presents the implementation of three dimensional image registration for the alignment of high-resolution in vivo trabecular bone MR images of the proximal femur. Robustness of the algorithm and effects of interpolation on trabecular bone parameters are assessed.

Chapter 6 applies image registration method presented in chapter five to a longitudinal clinical study assessing the efficacy of drug treatment and demonstrates an improvement in measurement accuracy.

Chapter 7 proposes an automated prospective registration methodology to acquire follow-up tibia MR images of trabecular bone in the same orientation as baseline images.

Chapter 8 extends the prospective registration algorithm presented in chapter seven to sagittal and coronal imaging planes.

Chapter 9 summarizes the work presented in Chapters 3-8 and discusses the advantages, limitations and scope of future improvement.

Chapter 2

Background

2.1 Bone

Bone is organized into cortical bone and trabecular bone. Cortical bone consists of dense bone tissue and forms the outer shell of the bone as well as much of the diaphysis, the shaft-like portion of long bones. In contrast, trabecular bone is relatively porous with bony spicules called trabeculae spanning pores. Trabecular bone is found in skeletal sites such as the vertebrae and the proximal and distal parts of the appendicular skeleton.

Bone consists of living cells widely scattered within a nonliving material called the matrix. The bone matrix is composed of 40% organic substrate consisting mainly of type I collagen, 45% mineral crystals of non-stoichiometric calcium hydroxyapatite and %15 water. It is formed by osteoblasts, cells that are constantly renewed in the bone. Osteoblasts make and secrete the protein collagen type I, which makes bones elastic, and mineral crystals salts, which impart the bone's hardness. As bone tissue matures, osteoblasts transform into osteocytes, mature bone cells that carry out daily cellular activities. An osteoclast is a type of bone cell that removes bone tissue by removing its mineralized matrix and breaking up the organic bone. Remodeling or bone turnover is the process of osteoclast resorption followed by osteoblast replacement of bone. Osteoblasts and osteoclasts, coupled together via paracrine cell signaling, are referred to as Bone Remodeling Units.

2.2 Osteoporosis and Bone Strength

Osteoporosis is a disorder that results in bone with decreased mechanical strength and increased fracture risk. Approximately one in two white women and one in five men are affected by osteoporosis in their lifetime(1,2). Osteoporosis is responsible for millions of fractures annually involving mostly vertebral bodies, the proximal femur, and the distal radius. The direct financial cost attributable to osteoporotic fracture in the United States is $14 billion and is expected to increase 3-to-8 fold over the next 50 years(13). Treatments, such as bisphosphonates, are available that have shown significant reduction of fracture incidence(14,15). Early diagnosis is paramount for intervention, yet signs of the disease cannot be routinely and reliably detected until a fragility fracture occurs. For this reason there exists intense interest within the medical community for developing accurate early diagnostic techniques.

Bone fracture risk and bone strength are influenced by many complex factors including architecture, turnover, damage accumulation, and mineralization. Assessment of bone fracture risk is currently performed using areal bone mineral density (BMD) derived from Dual Energy X-ray Absorptiometry (DXA). In 1994, the World Health Organization developed criteria for osteoporotic status based on T score values as determined by (DXA)(4). However, BMD does not entirely predict bone fracture(5,16,17) or adequately asses therapeutic intervention(6) and there exists considerable overlap of BMD measurements for patients with and without fragility fractures(18). BMD has been found to explain less than half of the effect of drug therapy on fracture rates(16,17).

BMD does not characterize the changes that occur in both cortical and trabecular bone with Osteoporosis. Trabecular bone micro-architecture is of particular importance to

bone strength(19) and cortical bone has a complex structure that also plays an important role in bone strength(20). Since trabecular bone has a higher metabolic activity and is highly responsive to hormonal changes, substantial efforts have focused on diagnosing early trabecular bone loss(21). Changes in the trabecular bone are characterized by both thinning and loss of structure(22). Structure and mechanical properties of cortical bone have been reported to change due to age(23,24), gender(25), and osteoporotic status(26). Additionally, the improvement in cortical thickness and cortical porosity due to anti-resorptive therapies highlights the importance of cortical bone in overall bone quality maintenance(27,28).

The degree of mineralization in trabecular bone or tissue mineral density (TMD) may play a role in bone strength that cannot be accounted for by bone mineral density (BMD) or bone micro-architecture alone. TMD has been shown to influence tissue-level mechanical properties(29). Increased mineralization has been linked to greater amounts of tissue damage(30) and hyper-mineralized sites may lead to crack initiation(31). Additionally the distribution of TMD within the bone tissue may also have an effect on tissue properties(32,33).

2.3 Imaging Bone

Many different imaging techniques exist to visualize measure bone structure. Dual X-ray Absorptiometry is a two dimensional method that measures BMD, the current gold standard in assessing osteoporotic status. However, many three dimensional methods exist including Micro Computed Tomography (μCT), Synchrotron Radiation Micro Computed Tomography(SRμCT), multi-detector Quantitative Computed Tomography (QCT), High Resolution peripheral Quantitative Computed Tomography

(HR-pQCT), and Magnetic Resonance Imaging (MRI). The three dimensional analysis provides additional information about bone allows for a three dimensional quantification of bone parameters. In this next section, a review of these different modalities with the advantages and limitations of each will be provided.

2.3.1 Micro Computed Tomography

Micro Computed Tomography (μCT), is a miniaturized version QCT which is able to achieve resolution of up to resolutions up to 6μm isotropic. It can therefore be used to visualize fine trabecular structure in ex vivo specimens. Structure parameters obtained from μCT correlate well with those from traditional histology(34,35) and therefore μCT is often used as a gold standard of reference. Researchers are currently using mineral phantoms and beam hardening corrected reconstruction algorithms in μCT systems to produce tissue mineralization data. μCT techniques are limited to imaging biopsies and small animals; bore sizes are too small and radiation doses too high for human use.

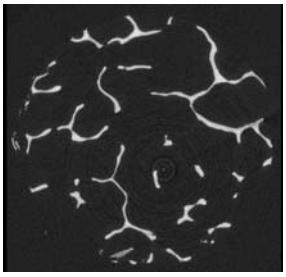

Figure 2.1.: Ex vivo μCT image of a vertebral body specimen.

2.3.2 Synchrotron Radiation Micro Computed Tomography

Synchrotron Radiation Micro Computed Tomography (SRμCT) is a mono-chromatic x-ray based imaging technique that requires a high photon flux in a small area. It is able to achieve resolution up to 6μm with very high signal to noise (SNR). Non-invasive high resolution three dimensional

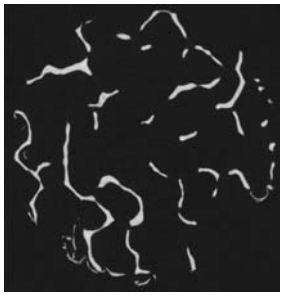

Figure 2.2.: Ex vivo SRμCT image of a vertebral body specimen.

assessment of tissue mineral density (TMD) can be performed using SRμCT(36,37). However, synchrotron radiation sources can only be found at a synchrotron radiation (SR) facility. This limitation causes SRμCT to be inaccessible to most researchers due to the scarcity of these SR facilities. Similar to μCT systems, SRμCT is also limited to imaging biopsies and cannot be used for in vivo human scanning.

2.3.3 Dual X-ray Absorptiometry

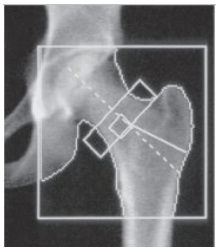

Figure 2.3.: In vivo DXA image of the proximal femur.

Clinically BMD is currently measured using a projection imaging technique called Dual x-ray Absorptiometry (DXA). In DXA, X-ray beams of two different peak energies are produced to optimize the separation of mineralized bone and soft tissue components of the area analyzed. A low energy and a high energy x ray beam are created by rapidly switching the voltage from 70 to 140 kpV. Since DXA is a projection technique, it only measures areal BMD. The advantages of DXA include low radiation dose, low cost, ease of use, and rapidity of measurement. However, limitations are inherent to DXA measurements. This two-dimensional technique cannot distinguish between cortical and trabecular bone, and cannot discriminate changes due to bone geometry (e.g., increases in the third dimension) from those purely due to increased bone density (within a fixed volume of bone).

2.3.4 Quantitative Computed Tomography

In Quantitative Computed Tomography (QCT), x-ray attenuation measurements through an object at different positions and different projection angles are made. A radiation source produces X-rays that pass through the object of interest to a detector on

the opposite side. The source and detector rotate about the imaged object, and the attenuated X-rays are obtained as a set of projections which are used to produce a three-dimensional data set of the spatial variation in X-ray attenuation within the object. Calibration phantoms are used to convert attenuation to mineral density, yielding volumetric BMD (g/cm3). In QCT the phantom, which contains five different amounts of calcium hydroxyapatite, is placed below the object of interest. A linear relationship exists between the x-ray attenuation and the amount of calcium hydroxyapatite so that attenuations can then be mapped back to density of calcium hydroxyapatite and volumetric BMD. The important advantage of QCT over DXA is the three-dimensional spatial resolution, which provides the ability to assess both volumetric BMD and macro-architecture. However, Clinical QCT scanners have a high radiation dose and do not have sufficient resolution to image individual trabeculae.

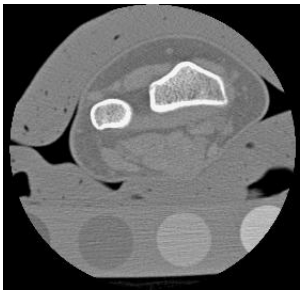

Figure 2.4.: In vivo QCT image of the distal radius.

2.3.5 High Resolution peripheral Quantitative Computed Tomography (HR-pQCT)

A recent development in QCT technology is the availability of High Resolution peripheral QCT (HR-pQCT) scanners which can achieve an isotropic nominal resolution of 82μm. These scanners produce three-dimensional mineralization data in appendicular sites, commonly the distal radius and distal tibia. As with traditional clinical QCT, trabecular and cortical compartments can be isolated and studied individually. However, because of the high resolution, individual trabeculae can

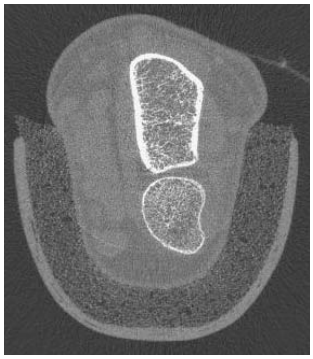

Figure 2.5.: In vivo HR-pQCT image of the distal radius.

also be depicted. From HR-pQCT images, a three dimensional technique can quantify structural measures synonymous with histomorphometric measures such as trabecular bone volume fraction (BV/TV), trabecular thickness (Tb.Th), trabecular spacing (Tb.Sp), and trabecular number (Tb.N)(38,39). Peripheral scanners make QCT technology less expensive, easier to use, and more accessible than traditional whole-body QCT scanners. Additionally, pQCT scans present a lower radiation dose to the central body. The greatest advantage of these machines, however, is the ability to image at a resolution that allows for trabecular visualization. A disadvantage of the technique is that it is confined to peripheral sites, and thus is not capable of providing images or direct measures within the spine or proximal femur.

2.3.6 Magnetic Resonance Imaging

Magnetic Resonance (MR) imaging is the only imaging method without ionizing radiation to access in vivo, non-invasively, three dimensional trabecular bone structure. Hydrogen, a proton present in water, is the most frequently studied component in MR imaging. However, bone tissue has a very low water content (~15%). Additionally, the protons within bone tissue water have a very short T2 relaxation time (250 microseconds) (40). As a result bone has a relatively low MR-detectable magnetization and gives no signal in standard MR images. Bone is instead revealed indirectly through bone marrow visualization, which has a high water and fat content. In high resolution MR images bone tissue appears black while bone marrow, due to its

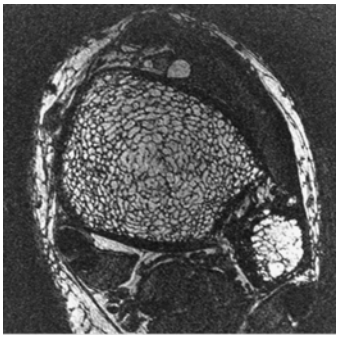

Figure 2.6.: In vivo MR image of the distal tibia.

sufficient amounts of water and fat, produces a high signal. Figure 2.6 shows an MR image of the trabecular bone structure of the distal tibia where the dark intensity network represents the trabecular bone network and the high intensity represent bone marrow in the trabecular spaces.

The ability to visualize and quantify the trabecular bone structure depends on the MR pulse sequence implemented. The pulse sequence needs to allow for high resolution which will ensure the voxel size is on the order of the trabecular structure (80-150μm) and allow for an artifact free image with high Signal to Noise (SNR). It needs to allow for scanning of a large volume while keeping scan time within the limits of the patient's tolerance (10 to 15 minutes). Pulse sequences which meet these needs and are used for imaging trabecular bone are variants of the basic gradient-echo sequence, Gradient-Recalled Acquisition in Steady State (GRASS) and spoiled GRASS (SPGR), a spin-echo-based Fast Large-Angle Spin-Echo (FLASE)(41) sequence, and a balanced Steady-State Free Precession (SSFP) sequence(42). There are trade-offs with all of these pulse sequences in terms of time, SNR, signal distortions which may effect the quantification of trabecular bone(42-44).

In order to quantify trabecular bone structure, first each pixel pertaining to bone or to bone marrow needs to be identified. This binarization step becomes problematic in the presence of partial volume blurring. The spatial resolution of the image, especially in the slice direction is greater than the dimension of the trabecular bone, causes each pixel in the volume of interest (VOI) to contain a varying mixture of bone and marrow, not just one type of tissue (partial volume effects). Initially, a histogram of the distribution of signal intensities in the VOI is plotted. Due to the partial volume effects, the histogram

does not have two distinct peaks corresponding to bone and marrow, but rather a single peak and an asymmetric tail. Therefore it is difficult to select an intensity to binarize the VOI into trabecular bone and marrow. The two main methods developed were a histogram deconvolution algorithm (HDA)(45) and standardized histogram intensity based method(7).

Many techniques have been developed to evaluate and quantify trabecular bone structure using MRI. Most MR studies investigating trabecular bone structure have used MR-derived trabecular bone parameters analogous to those using in bone histomorphometry. Majumdar et al.(8) successfully adapted histomorphometric methods to MRI. For each slice in the VOI the total number of pixels contributing to the bone phase, Pp, are normalized to the total number of pixels. The total number of trabecular bone marrow boundaries that cross a set of parallel rays at a given angle, θ, through the image are counted to obtain PL(θ). The mean intercept length (MIL), an index of trabecular width, at a given angle, θ, is then computed as the ratio between the total area of trabecular bone and half the number of edges between bone and bone marrow that intersect the set f parallel rays passing through the image at that angle.

$$MIL(\theta) = 2\ Pp/PL(\theta) \qquad (2.1)$$

The mean value of the MIL for all angles provides a measurement of trabecular width, Tb.Th, such that Tb.Th = ½ average value of MIL(θ). From the measurements of Pp and Tb.Th, other histomorphometry measurements such as trabecular number, Tb.N. = Area fraction of bone/Tb.Th and trabecular spacing, Tb.Sp = (1/Tb.N)-Tb.Th can be calculated. High spatial resolution MR images of trabecular bone have voxel sizes on the order of trabecular thickness, thus partial volume, when each voxel in the image could

represent more than one tissue type, effects MR-based trabecular structure assessment. MR images may not depict very thin trabeculae or may represent an average or projection of a few trabeculae. For this reason, MR-derived trabecular bone parameters are commonly termed "apparent" measures. A study conducted by Majumdar et al.(8) demonstrated the feasibility of using this technique to MR images to quantify trabecular structure.

2.4 Image Registration

2.4.1 Introduction

Image registration is the process of aligning two images. The goal is to find a transformation that aligns or matches the anatomical regions of the two images. It is useful for comparing images of the same modality that are taken at different time points and to allow the fusion of comparison of two images acquired with different imaging modalities. Image registration has many clinical and research applications(46-49).

There are two main categories of image registration: feature-based and intensity based. In feature-based methods salient features are either manually or automatically extracted from the images and are then aligned. In contrast, in intensity-based methods all the voxel intensity values in the image help to determine alignment of the images. Because segmentation of bone images is difficult due to their shape or vague boundaries, especially in MR images, an intensity-based approach is most reasonable. Intensity-based methods require three steps: specify the type of transformation, select a similarity measure, and determine the optimal method to search for the transformation which results in the best similarity measure. Each of these steps will be described in the following sections.

2.4.2 Transformations

In order to change the position, orientation, or shape of anatomical structures in an image, a spatial transformation is applied. Mathematically a spatial transformation is expressed as a set of equations relating the original image coordinates to the new ones. These equations are often restricted to limit the possible deformations in the image. The transformation is often described by its Degrees of Freedom (DOF), which is the number of independent ways that the transformation can be changed. Increasing the number of degrees of freedom allows the transformation greater scope to make one image match another. The three most common transformations are rigid (6 DOF), non-rigid (12 DOF) and deformable (>12 DOF). In a rigid transformation only rotations and translations are allowed. A non-rigid transformation allows skew and scaling in addition to rotation and translation. A deformable transformation defines a free-form mapping from one image to another and can require a constraint to preserve topology of the mapping.

One of the most commonly used affine transformation methods in medical imaging is the 3D similarity transform, also known as Helmert transformation or 7-paramter transformation(50). When it is applied to an image, it has the effect of rotating, translating, and scaling points with respect to the Cartesian coordinate axes.

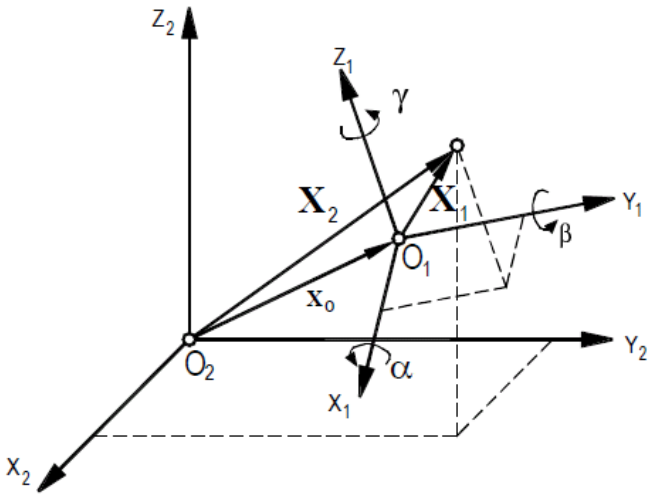

Figure 2.7.: Three dimensional similarity transform, also known as Herlmert transformation or 7-paramter transformation.

Two data sets of three dimensional coordinates defined in two different coordinate systems X_1 and X_2 (Figure 2.7) can be related to each other using a 3D similarity transform:

$$\begin{pmatrix} X_2 \\ Y_2 \\ Z_2 \end{pmatrix} = \begin{pmatrix} \delta x \\ \delta y \\ \delta z \end{pmatrix} + \mu \cdot \boldsymbol{R}(\alpha,\beta,\gamma) \cdot \begin{pmatrix} X_1 \\ Y_1 \\ Z_1 \end{pmatrix} \tag{2.2}$$

Where:

$\begin{pmatrix} X_1 \\ Y_1 \\ Z_1 \end{pmatrix}$ denotes the coordinates of a point in the first coordinate system;

$\begin{pmatrix} X_2 \\ Y_2 \\ Z_2 \end{pmatrix}$ denotes the coordinates of a point in the second coordinate system;

(α,β,γ) denotes the three rotation angles around the x, y, and z axis respectively which are also referred to as three Euler angles;

μ denotes the scale factor;

$\boldsymbol{R}$ denotes the total rotation matrix with is the product of the three individual rotation matrices:

$$\boldsymbol{R} = \boldsymbol{R}(\alpha,\beta,\gamma) = \boldsymbol{R}_1(\alpha)\cdot\boldsymbol{R}_2(\beta)\cdot\boldsymbol{R}_3(\gamma) \tag{2.3}$$

$$= \begin{bmatrix} \cos\alpha & \sin\alpha & 0 \\ -\sin\alpha & \cos\alpha & 0 \\ 0 & 0 & 1 \end{bmatrix} \cdot \begin{bmatrix} \cos\beta & 0 & -\sin\beta \\ 0 & 1 & 0 \\ \sin\beta & 0 & \cos\beta \end{bmatrix} \cdot \begin{bmatrix} 1 & 0 & 0 \\ 0 & \cos\gamma & \sin\gamma \\ 0 & -\sin\gamma & \cos\gamma \end{bmatrix} \tag{2.4}$$

$$= \begin{bmatrix} \cos\beta\cos\alpha & \cos\gamma\sin\alpha + \sin\gamma\sin\beta\cos\alpha & \sin\gamma\sin\alpha - \cos\gamma\sin\beta\cos\alpha \\ -\cos\beta\sin\alpha & \cos\gamma\cos\alpha - \sin\gamma\sin\beta\sin\alpha & \sin\gamma\cos\alpha + \cos\gamma\sin\beta\sin\alpha \\ \sin\beta & -\sin\gamma\cos\beta & \cos\gamma\cos\beta \end{bmatrix} \tag{2.5}$$

A transformation with the scale factor is the same in all directions (x, y, and z) is called a similarity transform. When the scale factor is unity the transformation is called an orthogonal or rigid transformation. Due to the rigid nature of bone, this thesis focuses on rigid transforms in which the scale factor, μ, in equation 2.2 is equal to unity.

2.4.3 Interpolation

When a transform is applied to an image, resampling is required because the new coordinate points may not line up with the old coordinate points. Image resampling determines pixel values for the new coordinate points by generating a continuous function from a discrete one using an interpolation function and then sampling the continuous signal at a new set of positions(51,52). Exact resampling is only possible if the interpolation function is an ideal low pass filter (a rect function in the frequency domain). An ideal low pass filter is equivalent to convolving a sinc function which has infinite extent in the spatial domain (figure 2.7). However, a sinc function is not

physically realizable. Therefore, finite impulse response filters must be used as the interpolation function(53).

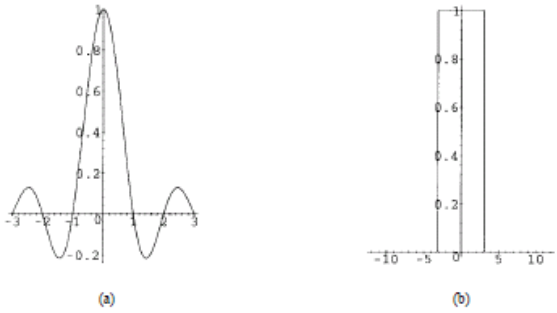

Figure 2.8.: Ideal Interpolation. (a) Kernel plotted for |x|<3. (b) Magnitude of the Fourier Transform. Taken from (53).

Nearest-Neighbor: The simplest interpolation function is nearest-neighbor, in which each interpolated output voxel is assigned the intensity of the nearest voxel in the input image. Therefore only one supporting point is required. Nearest-neighbor interpolation can be achieved by convolving the input image with a rect function in the spatial domain and is therefore equivalent to multiplying by a sinc function in the frequency domain (figure 2.9). Mathematically, the nearest neighbor expression is given by

$$h(x) = \begin{cases} 0 & x < \dfrac{-1}{2} \\ 1 & \dfrac{-1}{2} \le x > \dfrac{1}{2} \\ 0 & \dfrac{1}{2} \le x \end{cases} \tag{2.6}$$

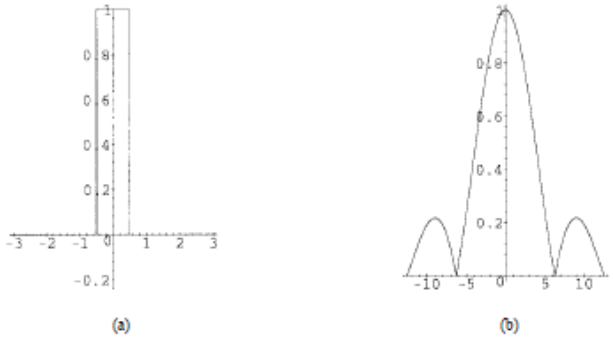

Figure 2.9.: Nearest Neighbor Interpolation. (a) Kernel. (b) Magnitude of the Fourier Transform. Taken from (53).

Linear Interpolation: Linear interpolation the simplest interpolator that builds a continuous function out of a sequence of discrete samples. It is made from the convolution of a square pulse with itself, which yields a triangle, sometimes also named a hat or a tent function (figure 2.10). The output voxel intensity is assigned a value that is weighted by the values of the direct neighbors. In 2D, also called bilinear interpolation, its implementation requires four samples, and in 3D, where it is called trilinear interpolation, it requires six samples (eight in the non-separable case). Trilinear interpolation (54) is the extension of linear interpolation to three dimensional spaces. Trilinear interpolation computes inter-slice voxel values as a distance-weighted average of the voxel values assigned to the eight nearest neighbors. The expression for 1D linear interpolation:

$$h(x) = \begin{cases} 1 - |x| & |x| < 1 \\ 0 & 1 \le x \end{cases} \tag{2.7}$$

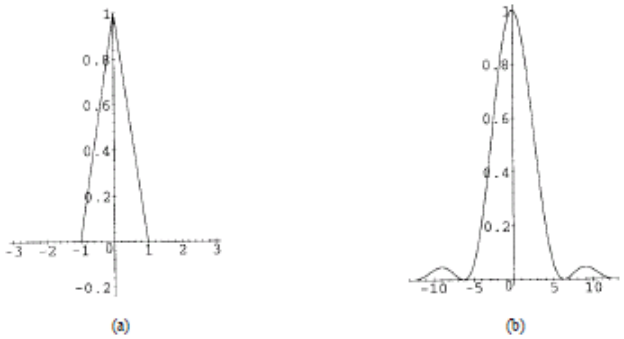

Figure 2.10.: Linear Interpolation. (a) Kernel. (b) Magnitude of the Fourier Transform. Taken from (53).

B-Spline Approximation: B-splines have also been proposed for an interpolation function. B-splines use low-degree polynomials in each of the intervals, and select the polynomial pieces such that they fit smoothly together. A B-spline function of degree n is derived through n convolutions of the box filter. Since, the B-spline function is an approximating function that passes near the points but not necessarily through them, the data will still be modified if the image is resampled to the same grid. The B-spline function is therefore often called B-spline approximation and is expressed:

$$\beta^0(x) = \begin{cases} 1 & |x| < \frac{1}{2} \\ \frac{1}{2} & |x| = \frac{1}{2} \\ 0 & |x| > \frac{1}{2} \end{cases} \tag{2.8}$$

and

$$\beta^n(x) = \sum_{k=0}^{n+1} \frac{(-1)^k (n+1)}{(n+1-k)!k!} \left(\tfrac{n+1}{2} + x - k\right)_+^n \quad \forall x \in R, \forall n \in N_* \tag{2.9}$$

where

$$(x)_+^n = (\max(0, x))^n \quad n > 0 \tag{2.10}$$

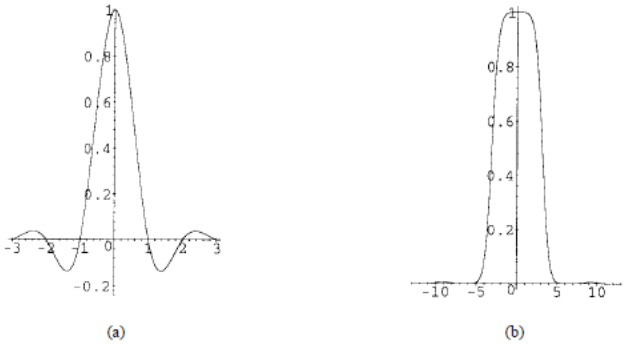

Figure 2.11.: Cubic B-spline Approximation. (a) Kernel. (b) Magnitude of the Fourier Transform. Taken from (53).

Often the precise value of the intensity at a point in the image is important and the choice of interpolation can be significant. However, for many registration algorithms it is sufficient that the interpolated intensity is similar to the surrounding tissue and the choice of interpolation method is not critical as long as it is smooth or continuous. Therefore, trilinear interpolation is most commonly used, due to its simplicity and speed, during the main registration calculations and then a more accurate interpolation method is applied when creating the final image.

2.4.4 Similarity Functions

Within the registration algorithm framework, the similarity function component is perhaps the most critical. The similarity function quantitatively measures how similar or aligned images are after a spatial transformation has been applied where better-aligned images are given a larger similarity value. Given a similarity function, an alignment between two images is achieved by systematically trying different transformations to find out which transformation results in the maximum similarity value. The selection of similarity function is highly dependent on the target images – some similarly functions are only suitable for mono-modality registration or cannot handle the presence of

intensity gradients in the images. While there are many similarity functions, in this section several of the more popularly used similarity functions are reviewed.

Mean Squares: The mean squares similarity function computes the mean squared pixel-wise difference in intensity between two images.

$$\mathrm{MS}(\mathrm{A},\mathrm{B}) = \frac{1}{\mathrm{N}}\sum_{\mathrm{i}=1}^{\mathrm{N}}(\mathrm{A}_{\mathrm{i}} - \mathrm{B}_{\mathrm{i}})^2 \tag{2.11}$$

A_i = the i-th pixel of Image A
B_i = the i-th pixel of Image B
N is the number of pixels

The optimal value of the means squares similarity function is zero and poor alignment between images results in a large value. The means squares similarity function is simple to compute but relies on the assumption that intensity representing the same homologous point is the same in both images. Hence, its use is restricted to images of the same modality. Additionally, any linear changes in the intensity result in a poor alignment.

Normalized Cross Correlation: The normalized cross correlation similarity function computes pixel-wise cross correlation between two images and normalizes it by the square root of the autocorrelation of each image.

$$NCC = -1 \times \frac{\sum_{i=1}^{N}(A_i \cdot B_i)}{\sqrt{\sum_{i=1}^{N}A_i^2 \cdot \sum_{i=1}^{N}B_i^2}} \tag{2.12}$$

Because of the -1 factor in the computation, the similarity function is optimal when its minimum is reached, when two images are identical the measure equals -1 and misalignments between the two images result in small measure values. The use of this similarity function is limited to images of the same imaging modality and it is insensitive

to multiplicative factors between the two images. However, it has a relatively small capture radius.

Mutual Information Metric: The mutual information is computed from the joint probability distribution of the images' intensity. When two images are aligned, they should provide maximal information about each other and the joint probability distribution results in a high mutual information value. The information contributed by each of the two images, denoted image *A* and image *B*, is entropy which measures the dispersion of a probability distribution. The entropy measure of an image is defined as

$$H(A) = -\sum p_A(a) \log[p_A(a)] \tag{2.13}$$

Here, p_A is the marginal probability distribution, the likelihood of finding pixels of a given intensity throughout the imaging volume. The joint entropy of the two imaging volumes A and B is defined as

$$H(A,B) = -\sum\sum\ p(a,b) \log[p(a,b)] \tag{2.14}$$

The mutual information of two images can be defined as the degree of dependence between image *A* and image *B* given by the distance between the joint distribution, *p(a,b)*, and the distribution associated with the case of complete independence, *pA(a)·pB(b)*

$$MI(A,B) = \sum\sum\ p_{AB}(a,b) \log[\frac{p_{AB}(a,b)}{p_A(a) \cdot p_B(b)}] \tag{2.15}$$

$$= H(A) + H(B) - H(A,B)$$

The advantage of using a mutual information similarity function is that the actual form of dependency between the two random variables does not have to be specified so that

complex mappings between two images can be modeled. Therefore, the mutual information similarity is very robust and well suited for multi-modality registration.

Typically, direct access to the marginal and joint probability densities of an image's intensities is not available and the densities need to be estimated from the image data. Parzen windowing, also known as kernel density estimation, can be used to estimate the densities by randomly sampling from the image to form a set S (55). A density function is then constructed by super-positioning a kernel function, K(s), centered on the elements of S along the intensity of grey-level axis. Mathematically the density estimate is given by:

$$P^*(a) = \frac{1}{N_S} \sum_{S_j \in S} K(a - s_j) \tag{2.16}$$

N_s = the number of samples
S = the set
K = the kernel

A number of functions can be used as the kernel, K, as long as they satisfy the requirements that they are symmetric, have zero mean, and integrate to one. Gaussian, box and B-spline functions all meet these criteria and can be used as the kernel. A smoothing parameter can also be used to scale the kernel function where the larger the smoothing parameter, the wider the kernel function and the smoother the density estimate. Using the density estimate, P^*, the entropy integral can be approximated by evaluating at discrete positions or bins uniformly spread within the dynamic range of the images. The entropy is then approximated by summing over the bins.

Normalized Mutual Information Metric: Studholme et al. (56,57) proposed a normalized measure of mutual information to address some of the limitations of the mutual information metric due to the size of the overlapping part of the images to be

registered. Studholme et al. demonstrated that with increasing mis-registration, the mutual information may actually increase when the relative areas of the object and background even out and the sum of the marginal entropies increases faster than the joint entropy. The normalized measure of mutual information, which is less sensitive to changes in overlap is calculated by:

$$\mathrm{NMI}(A,B) = \frac{H(A) + H(B)}{H(A,B)} \tag{2.17}$$

2.4.5 Optimization

Due to the complexity of similarity functions, there is usually no direct calculable analytical solution available and so the best transform which aligns the two images but be found by searching or optimization. In a registration algorithm, choosing an appropriate optimization is crucial because it is the most time-consuming part of the registration process and if the optimization gives inaccurate results then the overall alignment will be poor regardless of the similarity function or the transformation. The optimization needs to be fast and robust to local maxima or minima. While there are many optimizers, in this section will review on more popularly used optimizers. For more details on optimizers, there are various resources (58,59) on optimization.

Powell's Direction Set Method: Powell's direction set method optimizes each transformation parameter in turn and the result depends on the order of parameters being optimized. It does not require the gradient of the similarity function to be computed but it is fairly sensitive to local minimum.

Downhill Simplex Method: The downhill simplex method only requires similarity function evaluations and does not require derivatives, but because it considers all degrees of freedom simultaneously, it is not very fast.

Gradient Decent Optimizer: Starting from an initial guess for the transformation parameters, gradient decent is an iterative procedure that uses the partial derivatives of the similarity function, F(p), to construct and improve an estimate for the transformation. With each iteration, each transformation parameter (p) is updated by

$$p \leftarrow p + \lambda \frac{\partial F(p)}{\partial p} \tag{2.18}$$

λ is the learning rate which must be carefully chosen. If too small p might take a long time to approach a maximum. If chosen correctly p will converge toward the maximum relatively rapidly. Gradient decent optimization does not use a lot of storage and good for multidimensional problems.

2.4.6 Summary

Image registration algorithms require a transformation, a similarity function, and an optimization method. In order to choose a successful registration algorithm, it is important to select the appropriate transformation, similarity function, and optimization method given the images to be aligned. The transformation model selected must suit the registration problem. If an exact match between two images is required, but the anatomy is different in the two images, then a high DOF transform is required. However, if the images have the exact same anatomy then a rigid transform can be used because it enforces the correct constraints. In general lower DOF transforms are less sensitive to image quality and are therefore more robust. The selection of similarity function

determines the complexity of mapping between intensities. Some similarity functions only allow change in global brightness and contrast while others allow arbitrary intensity relationships. The optimization method is the final component in a registration algorithm and primarily determines not only the speed and robustness of the algorithm, but also effects the alignment accuracy. While state of the art registration algorithms are fairly robust, there is always the possibility that the resulting transformation is incorrect. No registration algorithm can guarantee to find the best transformation every time and may occasionally find a local maximum instead of the global maximum. Therefore, it is always advisable to visually check the registration results.

Chapter 3

Three-dimensional rigid body registration of synchrotron radiation micro-computed tomography and micro-computed tomography trabecular bone images

---

3.1 Introduction

Bone fracture risk and bone strength are influenced by many complex factors including architecture, turnover, damage accumulation, and mineralization. Assessment of bone fracture risk is currently performed using areal bone mineral density (BMD) derived from Dual Energy X-ray Absorptiometry (DXA). But BMD does not entirely predict bone fracture or adequately asses therapeutic interventions. The degree of mineralization in trabecular bone or tissue mineral density (TMD) may play a role in bone strength which cannot be accounted for by bone mineral density (BMD) or bone micro-architecture alone. TMD has been shown to influence tissue-level mechanical properties(29). Increased mineralization has been linked to greater amounts of tissue damage(30) and hyper-mineralized sites may lead to crack initiation(31). Additionally the distribution of TMD within the bone tissue may also have an effect on tissue properties(32,33).

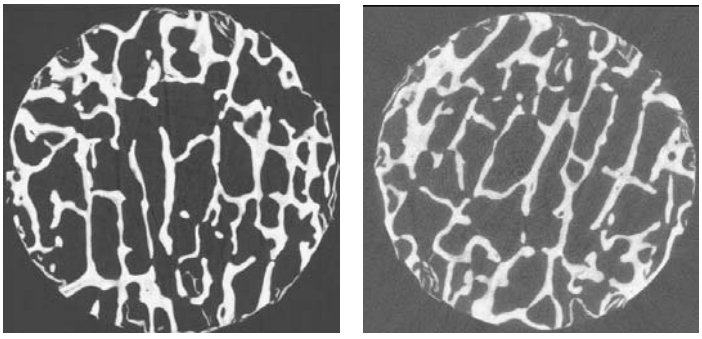

Figure 3.1: Proximal tibia specimen imaged with SRμCT (left) and μCT (right).

Unfortunately most common techniques for evaluating TMD do not provide three dimensional information and are destructive. These techniques include nanoindentation, Fourier-transform infrared spectroscopy, ashing, backscattered electron microsopy, and microradiography. Non-invasive high resolution three dimensional assessment of TMD can be performed using synchrotron radiation microcumputed tomography (SRμCT)(36,37) (Figure 3.1). However, SRμCT requires a high photon flux in a small area which can only be found at a synchrotron radiation (SR) facility. This limitation causes SRμCT to be inaccessible to most researchers due to the scarcity of these SR facilities. Conventional desktop micro computed tomography (μCT) (Figure 3.1) are widely available and may be a promising alternative to SRμCT. Several studies have begun to compare measures of bone micro-architecture(60) and TMD(61-63) between SRμCT and μCT. However more work is necessary to determine the appropriate mineralization calibrations and beam hardening correction algorithms as well as characterize volume-fraction dependent errors.

In order to accurately compare TMD measurements and distribution between SRμCT and μCT, image registration between these two modalities is required. Registration of two different imaging modalities is called *inter*-modal image registration for which the normalized mutual information measure(64,65) was specifically developed. Accompanying the choice of a registration similarity measure is the choice of a method to interpolate the 3D data into different spatial positions. Interpolators have important implications on the registration accuracy and efficiency, and three commonly used interpolators, in the order of increasing complexity, include nearest neighbor, linear and *b*-spline interpolation. There are many possible combinations of registration measures

and interpolators, and none of these techniques were specifically designed for SRμCT and μCT data where the high periodicity of the trabecular micro-structure could result in mis-registration. Furthermore, large data sets (i.e., >1GB data) will require efficient registration techniques, such as multi-resolution registration, and effective pre-processing.

The normalized mutual information similarity measure is a well-established method that is versatile for both intra- and inter-modal registration. Thus, it was hypothesized that the normalized mutual information measure in combination with a bspline interpolator for the final transform will provide accurate and efficient 3D image registration for high-resolution SRμCT to μCT trabecular bone images. The purpose of this study was three-fold:

1) To evaluate an established rigid registration approach (56,66) for aligning 3D SRμCT to μCT images of bone micro-architecture and determine which interpolator best preserves trabecular bone edges.
2) To evaluate TMD measurements between SRμCT and μCT using aligned images which allows for the direct comparison of TMD distributions.
3) To examine smoothing of the μCT images and how it affects the TMD compared to SRμCT values.

3.2 Methods

3.2.1 Specimens

Cylinders of trabecular bone (8mm diameter, 4mm length) were machined from specimens of the femoral head, vertebral body, and proximal tibia. The 5 femoral head specimens were surgically excised during hip arthroplasty procedures at UCSF. The four

tibia specimens and five vertebral body specimens were harvested from human cadavers (National Disease Research Interchange, Philadelphia, PA).

3.2.2 Image Acquisition

Each specimen was imaged on a conventional polychromatic μCT system (μCT 40 Scanco Medical AG., Buttisellen, Switzerland) and on beamline X2B of the National Synchrotron Light Source (Brookhaven National Laboratory, Upton, NY). The μCT images were scanned at an isotropic voxel size of 8μm with a source potential of 70 kV and tube current of 114 μA. The SRμCT images were scanned at an isotropic voxel size of 7.5 μm with a 26 KeV beam. Phantoms were also scanned with both modalities for beam hardening correction and tissue mineral density (TMD) calibration.

3.2.3 Registration and Interpolation

Both the μCT and the SRμCT images were imported as signed 16 bit data files and the SRμCT images were resampled to a voxel size of 8μm. Due to the size of the images (>1GB), the images were cropped to the diameter of the specimen (8mm) and the middle 100 slices (0.8mm). The cropped SRμCT images were registered to the cropped μCT with Rview (56,66) registration program. Rview performed the 3D rigid registration using a normalized mutual information metric, tri-linear interpolation, and a multi-resolution hill climbing optimizer(56). The final transform, consisting of 6 transformation parameters (Δx, Δy, Δz, α, β, γ) which aligned the SRμCT image to the corresponding μCT image, was saved. Here, Δx, Δy, Δz represent the required translational displacements in μm along the x-axis, y-axis, and z-axis respectively, while α, β, γ represent the required rotation angles in degrees around the x-axis, y-axis, and z-axis

respectively. To evaluate the effect of the interpolators the final transform was applied to one of the SRμCT images the with three different interopolators; nearest neighbor interpolation, linear interpolation, and b-spline approximation. The final transform was also applied to all of the SRμCT images with b-spline approximation. Registration and interpolation were performed on a Sun workstation (Sun Ultra 40, AMD Opteron Dual Core processor, 2.4 Ghz, 8 GB RAM, Sun Microsystems, CA).

A Gaussian filter (σ = 1, 3x3 kernel) was applied to the μCT, SRμCT, and the registered SRμCT to remove high frequency noise. Fixed global threshesholds for each image were determined manually and verified through visual comparison to the original grayscale image. Finally, all images were binarized in order to calculation the amount of voxel overlap between the μCT and SRμCT images. Voxel overlap is defined as $N_{overlap}/N_{total}$ where $N_{overlap}$ and N_{total} represent the number of μCT voxels that overlap SRμCT voxels and the total number of SRμCT present in the 3D volume respectively. The voxel overlap was calculated between the μCT images and the orginal SRμCT as well as the registered SRμCT images.

3.2.4 Evaluation of Tissue Mineral Density

Images were transformed to TMD maps using linear regression determined by the phantom calibrations(63). The μCT TMD maps are more affected by noise and imaging artifactsion, and have generally lower TMD concentrations. In order to compare differences in image equality and evaluate the effect of smoother of the μCT images, the trabecular bone images of both modalities were normalized to zero mean and unit variance. The μCT images were smoothed using a Gaussian(67) of increasing scales (σ = 1,2,3,4, and 5). The mean squared error (MSE) between the images was computed as a

function of smoothing over the region defined by the union of bone locations from the μCT and registered SRμCT images.

3.3 Results

The total time to register a μCT and SRμCT image and save the transformation, including uploading the images, is approximately 5 minutes. The parameters of the transforms that resulted from the registration algorithm are shown in Table 3.1. Rotations ranged from -67.1^o to 203.37^o and translations ranged from -879.1μm to 570μm.

Table 3.1: The output of the registration algorithm, a transform with three translations and three rotations for all 14 specimens.

	Specimen Number	ΔX (μm)	ΔY (μm)	ΔZ (μm)	α (o)	β (o)	γ (o)
Proximal Femurs	1	418.0	572.0	124.0	0.48	1.91	24.10
	2	43.6	17.0	164.0	1.91	179.05	80.95
	3	-11.3	5.7	-862.4	0.00	-0.34	203.37
	4	0.0	-45.3	-879.1	-1.43	-0.48	87.61
	5	-24.0	0.0	352.0	-1.91	0.95	-58.09
Proximal Tibiae	6	-36.0	36.0	-400.0	0.49	180.00	-39.27
	7	-80.0	-24.0	108.0	2.39	182.39	-67.14
	8	8.0	12.0	476.0	-0.48	1.91	-22.14
	9	-36.0	0.0	72.0	-0.95	184.30	25.43
Vertebral Bodies	10	-32.0	-60.0	244.0	0.48	-0.95	15.52
	11	-36.0	68.0	52.0	0.67	178.65	145.95
	12	-276.0	-100.0	-340.0	-5.25	-1.43	-0.95
	13	20.0	-64.0	-280.0	0.48	0.00	100.43
	14	-88.0	-20.0	-408.0	1.35	180.00	49.33
	average	-9.3	28.4	-112.7	-0.13	77.57	38.94
	st.dev	144.6	162.4	423.5	1.9	92.7	78.2

The computation time for nearest neighbor interpolation and linear interpolation was less than 60 seconds, while for b-spline approximation the computation time was on average 30 minutes. In Figure 3.2 the effects of the interpolation can be assessed visually. The linear interpolator appears to smooth the pixel intensities the most and the nearest neighbor interpolator exaggerates the edges of the trabeculae. The Bspline approximator

is able to preserve the distribution of pixel intensities with little smoothing and maintain the integrity of the trabeculae edges. Table 3.2. shows the mean and standard deviations of a slice selected at random for each of the interpolators and the SRμCT original image.

Table 3.2: Average pixel grey values for a single slice

Interpolation Method	Average Pixel Value	Standard Deviation
Original SRμCT image	652.5	32
Nearest Neighbor Interpolation	651.6	36
Linear Interpolation	653.1	33.6
Bspline Approximation	652.7	34.1

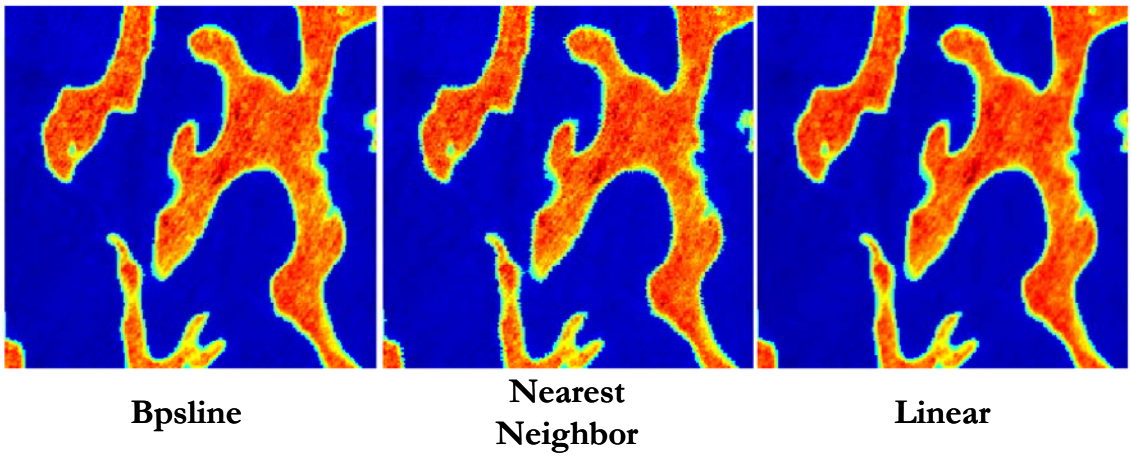

Figure 3.2: The effects of the gray-level interpolation can be assessed visually with a colormap. Registered SRμCT images with linear interpolation, nearest-neighbor interpolation, and b-spline approximation for the final transform are shown.

The success of the registration was evaluated both qualitatively and quantitatively. Visual examination of registration results showed improved voxel overlap between the μCT and SRμCT images. Figure 3.3 is an example of the close alignment of between the μCT and SRμCT image of one specimen. The improved image alignment was also assessed quantitatively by calculating the improvement in voxel overlap. Figure

3.4 shows the considerable improvement in the percentage of voxels that overlap between the μCT and SRμCT with registration. With registration there was a 49% - 70% improvement in the percentage of voxels that overlap.

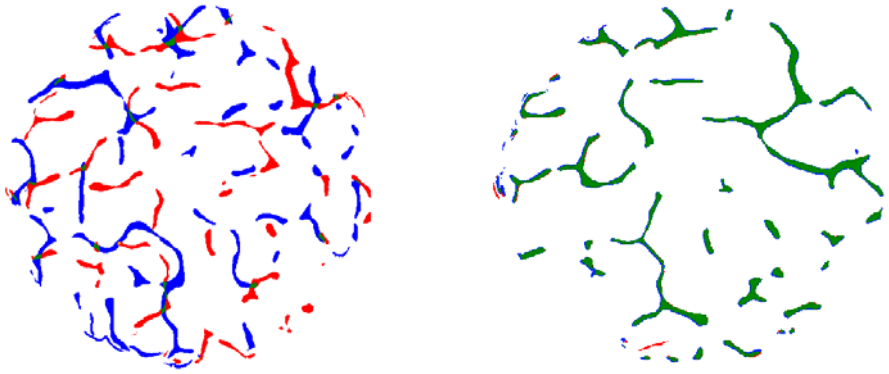

Figure 3.3:. An example mid-slice from μCT (blue) and SRμCT (red) before (left) and after (right) registration overlaid onto each other with green representing the regions of μCT and SRμCT overlap.

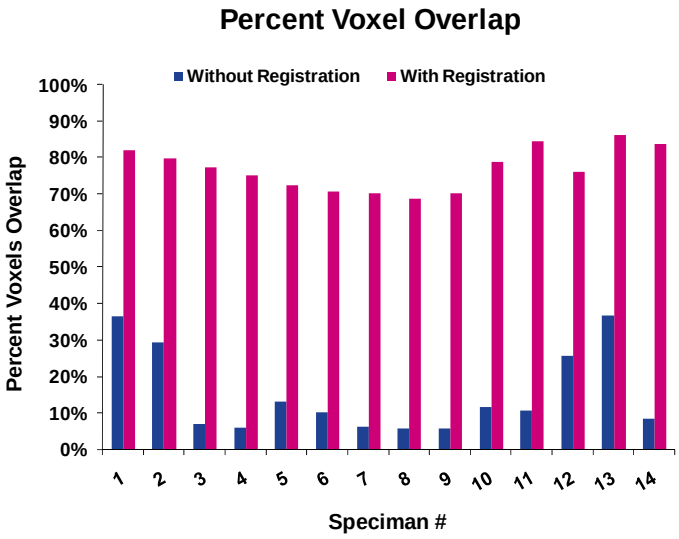

Figure 3.4: Comparison of voxel overlap before and after image registration for the fourteen 3D trabecular bone specimen images.

The MSE between SRμCT and μCT images reaches a minimum at σ = 2 (figure 3.5). The MSE of the normalized images has a mean of 0.38, the MSE of the normalized images when the CT image has been smoothed with a Gaussian with σ = 2 is 0.22.

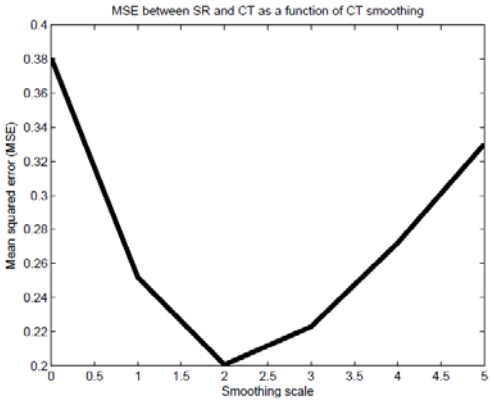

Figure 3.5: Mean MSE between normalized images as a function of μCT smoothing for the 14 specimens.

Smoothing with σ = 2 was then applied to the TMD maps (figure 3.6) and the improvement in TMD correlation between μCT and SRμCT was determined (figure 3.7).

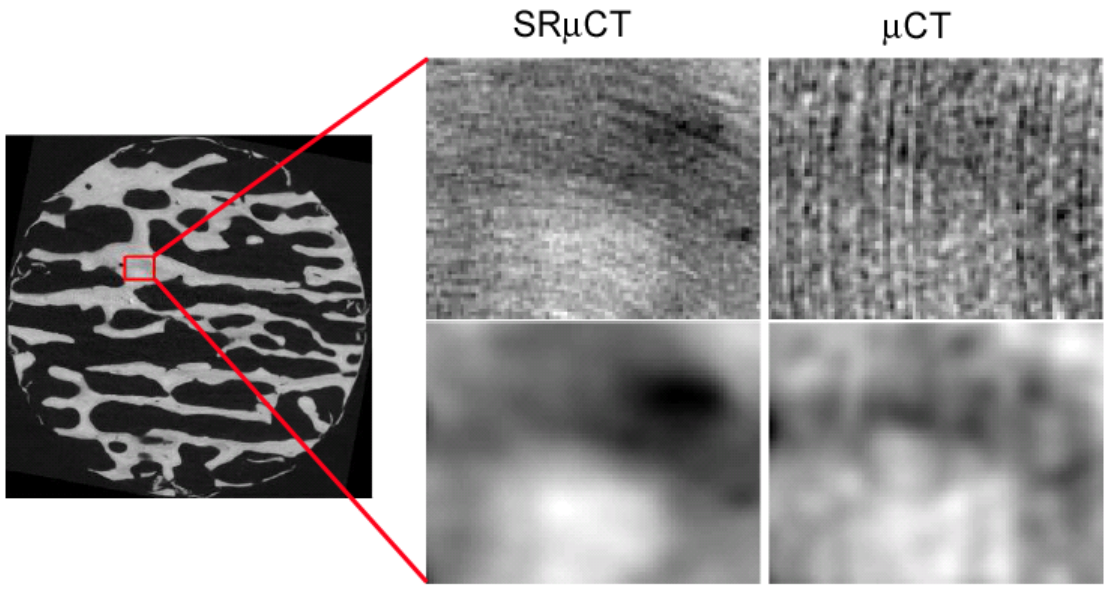

Figure 3.6: Example image where the region within the box is examined in greater detail Top left: part of SR image, top right: same part of CT image. Bottom left: SR image smoothed with a Gaussian (σ = 2), bottom right: CT image smoothed the same way. Note how after smoothing similar patterns can be visualized in both images.

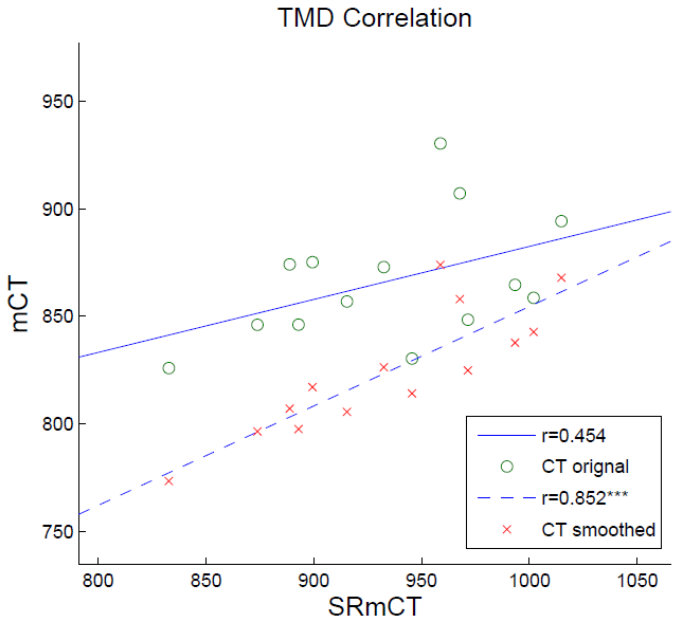

Figure 3.7: TMD correlation between SRμCT and μCT with and without Gaussian smoothing (σ = 2).***p<0.001

Figure 3.8 shows TMD topography maps for one slice of one of the specimens for the registered SRμCT and μCT images. The μCT was Gaussian smoothed (σ = 2) and then adjusted according to the linear regression established in figure 3.7. By visually inspecting the images in Figure 3.8, the μCT images with Gaussian smoothing and adjusted values appear more similar than μCT images without linear regression.

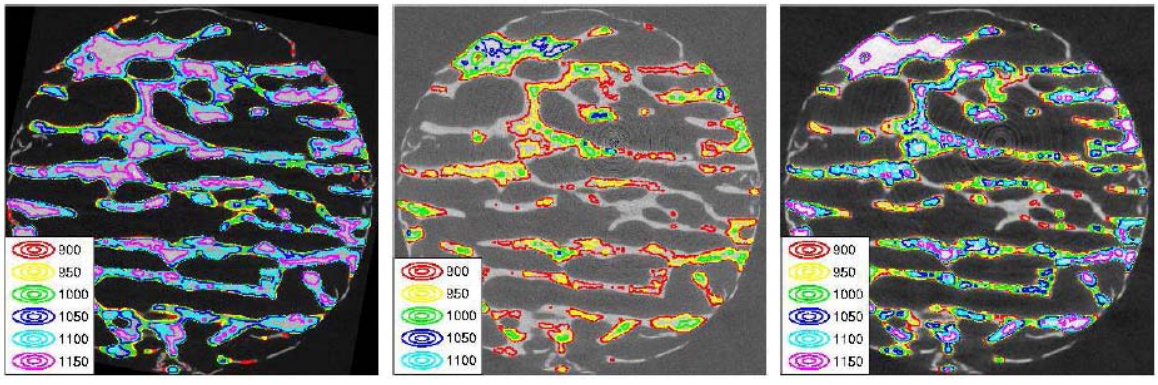

Figure 3.8: The registered SRμCT (left), the μCT (middle) TMD topography maps for one slices of corresponding structures. Each color corresponds to a level of TMD in mgHA/cm^3 specified. The μCT

TMD topography map after smoothing and adjusting the values according to the linear regression established in figure 3.7 (right).

3.4 Discussion and Conclusion

The degree distribution of trabecular bone tissue mineralization (TMD) has been recently linked to bone mechanical strength and fracture risk(29-33). μCT and SRμCT are both imaging methods which allow for the three dimensional evaluation of TMD. However, more work is necessary determine the accuracy and reliability of TMD measurements. In order to accurately compare TMD measurements and distribution between SRμCT and μCT, it is crucial to match the 3D volume analyzed. Any mismatch between the volumes may result in large variations in mineralization measures due to the heterogeneity of bone tissue mineral. In this work, we have demonstrated the feasibility and efficiency of the first fast multi-modal registration of 3D trabecular bone images. The alignment of these SRμCT and μCT images will ensure accurate TMD comparisons between the modalities.

In mineralization studies, the grayscale value of the trabecular bone in an image is mapped to a mineralization value. A calibration phantom containing different concentrations of K_2HPO_4 is imaged under identical experimental conditions and is used to convert the grayscale values to mineralization (hydroxyapatite concentration in gm/cm3). It is important to ensure that the different interpolation methods during image transformation do not severely effect grayscale values. In this study, we demonstrated that b-spline approximation is best able to preserve grayscale values. Linear interpolation smoothed the grayscale values and Nearest Neighbor created edge effects. While b-spline approximation may still smooth the grayscale values slightly, mineralization studies typically smooth images with a median filter(36) or Gaussian filter(63) prior to

mineralization quantification to reduce image noise. The disadvantage of using a b-spline approximation remains processing speed. In our studies, we are able to compromise speed, but if more samples need to be processed within the same about of time, it may be better to use a linear interpolator.

The image registration algorithm proposed in this study was able to successfully align SRμCT and μCT images. Voxel overlap measures and visual inspection both demonstrated the successful alignment. Although greatly improved, percentage voxel overlap between the registered SRμCT and μCT was still less than 100%. This is due to specimen non-rigid deformation between scans during handling and transport. Additionally bean hardening artifacts cause geometric non-uniformity.

The SRμCT and μCT images seem to convey similar TMD information although the μCT images are noisier. Applying Gaussian smoothing on a scale $\sigma = 2$ reduces the noise in the μCT images while still preserving sufficient image information so that correlation between SRμCT and μCT can be improved. The correlation between mean SRμCT and μCT TMD values was highly improved with smoothing of the μCT images ($r = 0:85$; $p < 0.0002$) compared to without smoothing ($r = 0:45$; $p < 0.2$). Additionally, by applying the Gaussian smoothing and applying a TMD value adjustment according to the linear regression, the TMD values and distribution of the μCT image visually appeared more similar to the SRμCT image. The results suggest that noise removal applied to μCT images can contribute to increased reliability of TMD estimates. Future work is needed to further evaluate TMD calibration methods and different beam hardening corrections for μCT images.

Registration is able to ensure accurate image alignment and therefore eliminate sources of error associated with the imprecision of unmatched volumes. This work demonstrated the feasibility of using a normalized mutual information based method to automatically register μCT and SRμCT image of trabecular bone. Additionally a direct comparison between SRμCT and μCT trabecular bone images from 14 specimens was performed and a smoothing strategy was established.

Chapter 4

In vivo Evaluation of the Presence of Bone Marrow in Cortical Porosity in Postmenopausal Osteopenic Women

---

4.1 Introduction

Cortical bone has a complex structure that plays an important role in bone strength(20). Structure and mechanical properties of cortical bone have been reported to change due to age(23,24), gender(25), and osteoporotic status(26). Additionally, the improvement in cortical thickness and cortical porosity due to anti-resorptive therapies highlights the importance of cortical bone in overall bone quality maintenance(27,28).

Recently studies have focused on porosity of the cortical bone(68-71). Macro-porosity has been defined as porosity with a diameter greater than 0.385 mm and is reported to increase with age(69). While the exact mechanism behind the formation of cortical macro-porosity is unknown, the existence of large cortical pores has been attributed to resorption spaces, merging of haversional canals, reduction in the rate of closure of haversion canals, and a clustering of osteons(68,72-75).

Cortical porosity has a significant impact on mechanical properties of cortical bone(76-79). Yeni et al. reported that femoral and tibial cortical bone toughness decreases with increasing cortical porosity (76). Additionally Young's modulus, a measure of stiffness, and the ultimate stress of cortical bone have both been shown to decrease with increasing porosity(77-79). Therefore, characterizing cortical porosity and enhancing our understanding of the formation of cortical porosity will contribute to the ability to estimate bone strength and predict fracture risk.

Hydraulic strengthening (HS) of bone refers to the theory that pressure due to bone fluids found in the cavities of bone might hydraulically strengthen bone by reducing

bone stresses during dynamic loading. If bone cavity fluid pressures are substantial, they may increase the load bearing capacity of bone. Several studies have estimated the fluid flow contribution or HS effect on trabecular bone mechanical properties (80-82) and cortical bone apparent modulus(83). However, the precise nature (viscosity and compressibility) of bone fluid present in cortical porosity is unknown(84) and accuracy of HS models depend greatly on defining appropriate bone pore fluid properties(83,85). The nature of the bone fluid may affect the bone's ability to withstand dynamic loading, therefore a more precise characterization of cortical bone fluid may help improve the accuracy of HS models.

High-resolution peripheral computed tomography (HR-pQCT) is an emerging imaging technique which achieves an isotropic nominal resolution of 82μm, allowing for visualization of cortical macro-porosity in vivo at peripheral sites such as the tibia and radius(86,87). Magnetic Resonance (MR) imaging is an imaging technique that allows visualization of soft tissues such as bone marrow. It is our hypothesis that by combining these two imaging techniques, visualization of bone marrow within cortical porosity is possible. Our goal is to observe the amount of cortical porosity that contains bone marrow in post-menopausal osteopenic women and determine if there is a relationship between pore size and the existence of bone marrow.

4.2 Methods

4.2.1 Subjects

The subjects in this study were 52 postmenopausal women (age 56$\pm$3.7) who were recruited for a double-blind study investigating the longitudinal effects of alendronate versus placebo on bone microarchitecture. Only women between the ages of

45 and 65 yr that had been postmenopausal for at least 1 year but not more than six years were included. They were required to be defined as osteopenic by the WHO criteria(88) and had no history of disease or treatment known to affect bone metabolism. The study protocol was approved by the UCSF Committee on Human Research and all women provided written informed consent.

Images in this study were taken from the baseline time-point prior to alendronate treatment. Imaging using both HR-pQCT and MR was attempted on all 52 subjects. However, three of the subjects could not tolerate the prone position required for the MR radius scan and one tibia MR image was excluded from the study due to motion artifact and poor image quality. Therefore this study analyzed radius images of 49 subjects and the tibia images of 51 subjects.

4.2.2 MR Imaging

MR images were acquired on a 3T (GE Signa) MR scanner. Images of the distal radius were acquired with the subject in a prone position using a transmit receive quadrature wrist coil (Mayo Foundation for Medical Education and Research) and images of the distal tibia were acquired with the subject in a supine position using a four channel dual paddle coil (Nova Medical). Images were obtained with a balanced steady state free precession (bSSFP) pulse sequence(42). Pulse sequence parameters were 512x384 matrix, 60^{o} flip angle, 122 Hz/pixel BW, 8cm FOV. The tibia images had a 16.8-17.8/6.5 ms TR/TE and scan time of 15 minutes and the radius images had a 14.4-15.21/3.3-3.9 ms TR/TE and scan time of 10 minutes. The image acquisition resulted in an image resolution of 156x156x500μm. Images were originally acquired with optimal scanning

parameters for trabecular bone quantification. However the bSSFP sequence also has superior signal-to-noise ratio and maximizes bone marrow signal(42,44).

4.2.3 HR-pQCT Imaging

HR-pQCT images of the tibia and radius were acquired on an XtremeCT in vivo scanner (Scanco Medical AG) with a 60 kVp source potential, 900μA tube current, and 100ms integration time. An image with 110 slices, beginning 22.5 mm and 9.5mm proximal to the endplate for the tibia and radius respectively, and with an isotropic nominal resolution of 82μm resulted from the 3 minute image acquisition. Immediately after image acquisition, the images were visually evaluated for motion artifacts and scans with obvious motion artifacts were repeated.

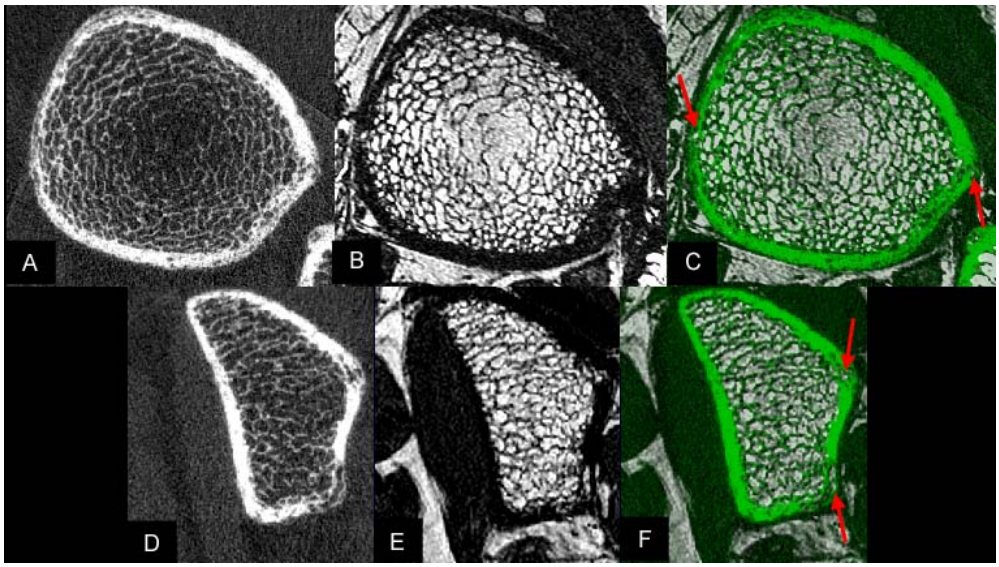

Figure 4.1: Representative tibia (A-C) and (D-F) radius images. A,D) HR-pQCT image B,E)Registered MR image C,F) Overlay between HR-pQCT (green) and MR image with cortical porosity containing bone marrow highlighted with red arrows.

4.2.4 MR and HR-pQCT Image Alignment

Visualization of bone marrow in cortical porosity identified in the HR-pQCT requires precise image alignment between the MR and HR-pQCT image. Image registration is the process of finding a transformation that aligns the anatomical regions of two images. Because bone is a rigid structure, a global rigid transform applied to the MR image aligning it to HR-pQCT image is desired. A registration algorithm based on mutual information has been shown to efficiently determine accurate transformations between different imaging modalities based on the joint probability distribution of their intensities(89,90). For each of the image pairs, Rview(66), a robust registration algorithm based on a normalized mutual information measure, was used to determine a rigid transformation consisting of three Euler angles and a translation vector. This rigid transformation was then applied to the MR image, using b-spline approximation for interpolation, to align and resample the MR image to the HR-pQCT image. Transformation and interpolation was not performed on the HR-pQCT image to ensure accurate measurement of cortical bone pore sizes. The registration and transformation was performed on a Sun workstation (Sun Ultra 40, AMD Opteron Dual Core processor, 2.4 Ghz, 8 GB RAM, Sun Microsystems, CA). The computation time for the registration was approximately one minute and for the application of the transformation was approximately 5 minutes.

The robustness of the registration was assessed using a technique similar to that presented by Studholme et al.(91) using one of the tibia and one of the radius image sets. We defined a series of 30 mis-alignments corresponding to a translation of 5mm and a rotation of 5^{o} to simulate different starting values. Each of the 30 mis-alignments was

determined by randomly selecting a point on the surface of spheres in translational and rotational parameter space. Each mis-alignment was selected as the initial starting guess for the registration. The resulting 30 transforms were recorded and applied to each pixel to calculate the root mean square error for each pixel in the volume.

4.2.5 Cortical Porosity Analysis

The HR-pQCT data were segmented and the periosteal surface was identified using evaluation routines provided by the manufacturer. A semi-automated edge-defining algorithm was applied to the original grayscale image to identify the periosteal surface. Then a previously described post processing protocol (92,93) was performed in which a low-pass guassian filter (σ = 2.0, support =3) and then a fixed global threshold was applied to identify the cortical compartment and segment the bone from background.

Code developed using MATLAB identified the cortical porosity in the HR-pQCT image and determined the existence of bone marrow in the aligned MR image. The process is depicted in Figure 4.2. To locate cortical porosity a two-dimensional mathematical morphologic hole filling algorithm(94) identified groups of connected components within the cortex. The area of each connected component (each cortical pore) was determined and the percent of cortical porosity for each slice was calculated by dividing the total area of the connected components by the entire cortical area (area of the cortical bone plus area of cortical porosity). The total number of cortical pores, the area of each cortical pore, and the average cortical pore area for each subject was recorded. MR images were segmented to identify bone marrow using a histogram thresholding technique(95) generally implemented to identify bone marrow in the trabecular region. Segmented HR-pQCT images with cortical porosity identified were then subtracted from

the segmented and aligned MR images to highlight cortical porosity filled with marrow. The number of cortical pores with marrow, the size of area cortical pore with marrow, and the average cortical pore area with marrow was recorded for each subject. The percent of cortical porosity filled with marrow was calculated by dividing the number of cortical pores with marrow by the total number of cortical pores for each subject.

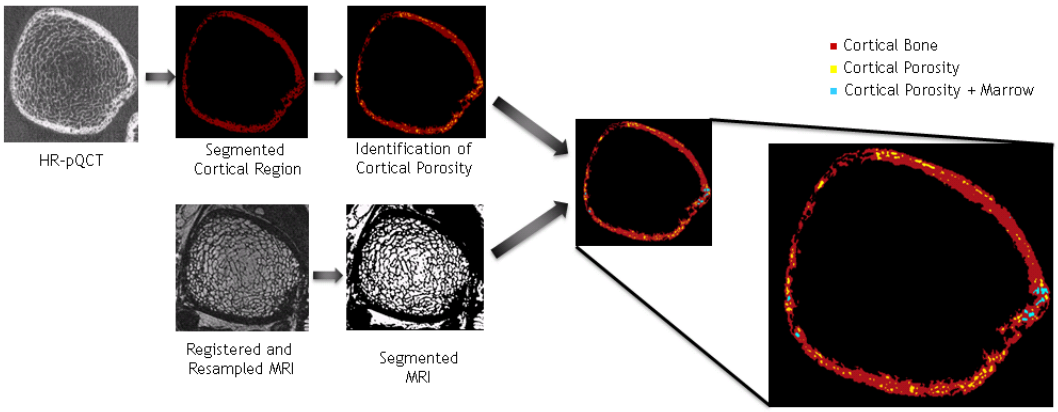

Figure 4.2: Diagram demonstrating image processing steps. The HR-pQCT image is smoothed and thresholded to identify the cortical compartment. The bone marrow in the MR image is segmented using histogram thresholding. The segmented MR image and the cortical region of the segmented HR-pQCT image are then combined.

4.2.6 Statistical Analysis

The Shapiro-Wilk W test was used to test the normality of the data and nonparametric methods were employed for all analyses of measurements that were not normally distributed. The significance of differences in the measurements between tibia and radius were determined using Wilcoxon signed rank test with significance set at $p < 0.05$. To examine relationships between measurements, linear regression analyses were performed and Spearman's coefficient, r, was obtained for the correlation. The changes in

measurements along the length of images regions was determined using Pearsons correlations and paired Student's t-tests or Wilcoxon signed rank tests where appropriate.

4.3 Results

By visual assessment registration of the MR image to the HR-pQCT image was successful for all of the tibia and radius image datasets. See Figure 4.1 for a representative tibia and radius example. For the tibia, mean translations in x,y,z were 0.10mm$\pm$1.61, -2.75mm$\pm$2.83, 3.06mm$\pm$2.92 and mean rotations in x,y,z were 5.16$^o\pm$3.55, -1.32$^o\pm$2.57, -2.60$^o\pm$6.49. For the radius, mean translations in x,y,z were 5.00mm$\pm$4.92, -4.09mm$\pm$4.47, -2.13mm$\pm$2.91 and mean rotations in x,y,z were -4.79$^o\pm$5.35, 174.57$^o\pm$3.80, 77.97$^o\pm$8.93. The large rotations in y and z for the radius are due to the different positioning required between HR-pQCT and MR scans. Therefore all registrations for the radius were initialized with at least 180^o in y and 80^o in z. The results from the assessment of the robustness of the registration showed that the RMS error for initial misalignments of 5mm and 5^o ranged from 0.029mm to 1.892mm (mean 0.420mm$\pm$0.912) with the larger RMS errors at the periphery of the image volume. Therefore, as long as the initial mis-alignment was within 5mm and 5^o the registration was successful within approximately 0.420mm. However, ten of the tibia sets and twenty-one of the radius sets had initial mis-alignments beyond 5mm and 5^o and registration was repeated with manual starting estimates to ensure an initial mis-alignment within the acceptable range for successful registration.

Cortical porosity was evident in all of the HR-pQCT images. The histograms for all subjects' percent cortical porosity, total number of cortical pores, and average cortical

pore area are shown in figure 4. The total number of cortical pores detected within each subject for the tibia ranged from 2805 to 13272 with a mean of 8027±2567 and the radius ranged from 397 to 4110 with a mean of 1615±783. The average percent of cortical porosity for all subjects for the tibia was 4.36%±1.6 and for the radius was 1.6%±0.8. The average cortical pore area for each subject is shown in figure 4.3 and the distribution for all cortical pores areas observed are shown in figure 4.4. The average area of the cortical pores for the tibia was $0.0585mm^2$±0.08 and for the radius was $0.0487mm^2$±0.06.

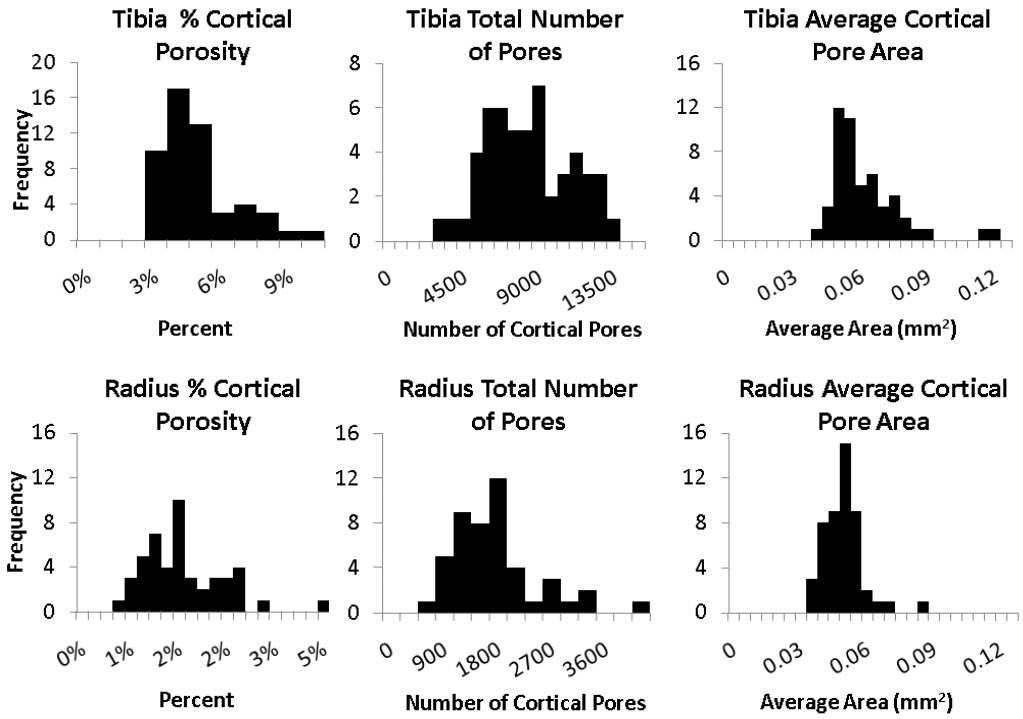

Figure 4.3: Histograms for percent cortical porosity, total number of cortical pores for each subject, and average cortical pore area for all tibiae (top row) and radii (bottom row). All measurements are significantly different in the tibia than the radius ($p<0.001$).

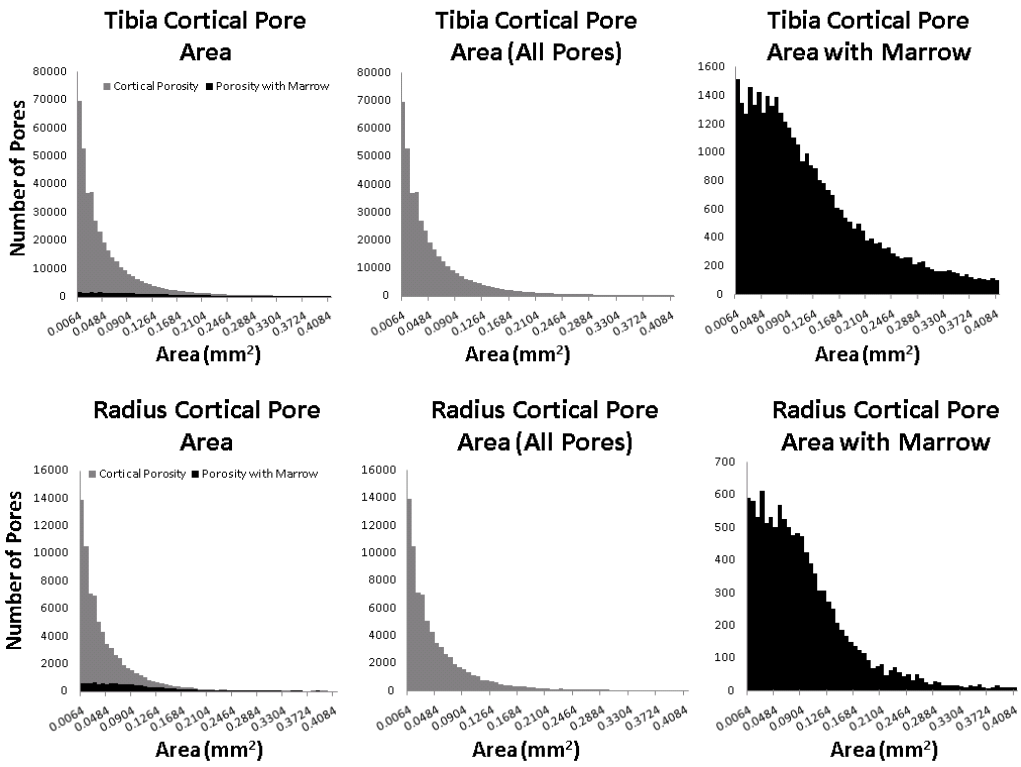

Figure 4.4: Histograms of the area for all of the cortical pores identified and all cortical pores with marrow for all tibiae (top row) and radii (bottom row).

Cortical porosity was observed both containing and not containing bone marrow in each subject in both the tibia and radius. Figure 4.5 shows histograms for all subjects' percent cortical porosity containing marrow, the number of cortical pores containing bone marrow, and the average area of cortical pores containing marrow. The number of cortical pores containing marrow for the tibia ranged from 152 to 2145 with a mean of 841±734 and for the radius ranged from 122 to 699 with a mean 266±108. The average percent cortical porosity containing marrow for all subjects for the tibia was 10.0%±6.3 and for the radius was 19.1%±8.9. The distribution of the areas of all cortical pores containing marrow observed are shown in figure 4.4 and the average cortical pore area for each subject is shown in figure 4.5. The average area of cortical pores containing marrow for the tibia was 0.155 mm^2±0.1 and for the radius was 0.093 mm^2±0.1.

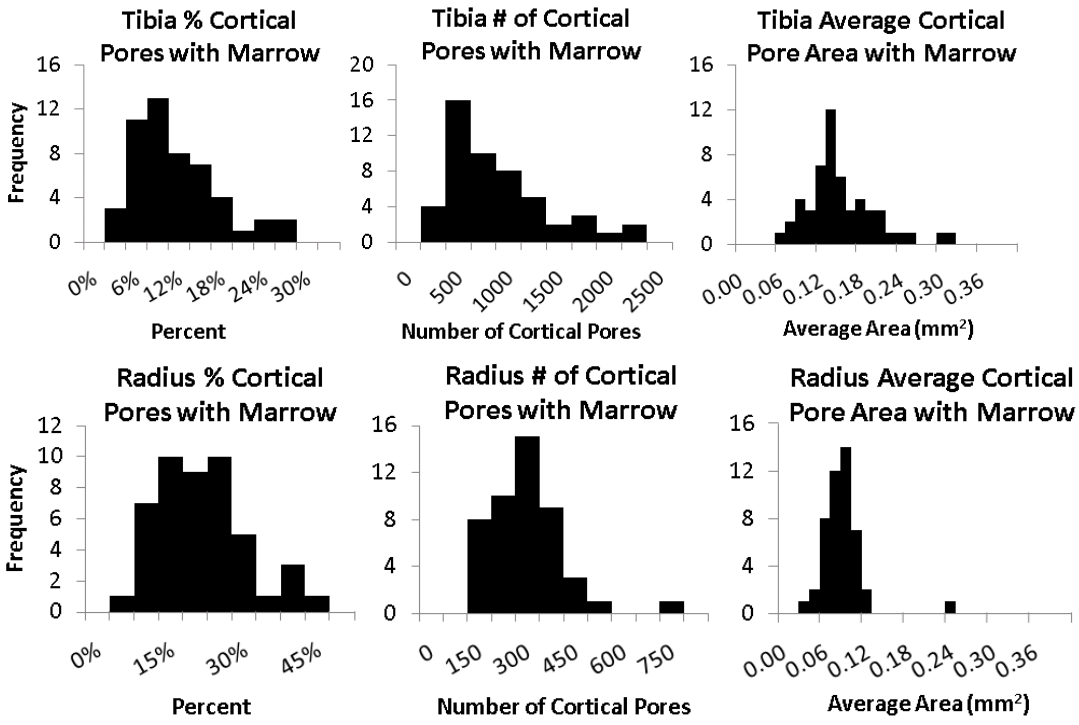

Figure 4.5: Histograms for percent cortical porosity containing marrow, total number of cortical pores containing marrow, and average cortical pore area containing marrow for all tibiae (top row) and radii (bottom row). All measurements are significantly different in the tibia than the radius ($p<0.001$).

The mean area of cortical pores containing marrow was significantly higher than the mean area of all the cortical pores ($p<0.001$) for both the radius and tibia. The mean area of all cortical pores within a subject ranged from 0.039mm^2 to 0.119 mm^2 in the tibia and from 0.032 mm^2 to 0.080 mm^2 in the radius while the mean area of cortical pores containing marrow ranged from 0.057mm^2 to 0.314mm^2 in the tibia and from 0.027mm^2 to 0.238mm^2 in the radius. However there was no relationship between the percent of cortical porosity and the percent cortical pores that contained marrow ($p>0.05$) nor the average cortical pore area and the percent of cortical pores containing marrow ($p>0.05$).

In figure 4.6 the average number of cortical pores and the average number of cortical pores with marrow are plotted to show variations as a function of distance from

the joint line (from distal to proximal). There was an increase in both the number of cortical pores and the number of cortical pores containing marrow with distance along the shaft for the tibia ($p<0.001$) but no relationship was determined for the radius. Figure 4.7 visually demonstrates the variations in cortical porosity in one subject in which there are fewer cortical pores in the most distal slice than in the most proximal slice. Additionally there was no significant increasing or decreasing trend for cortical pore area variations in the radius or the tibia ($p>0.005$).

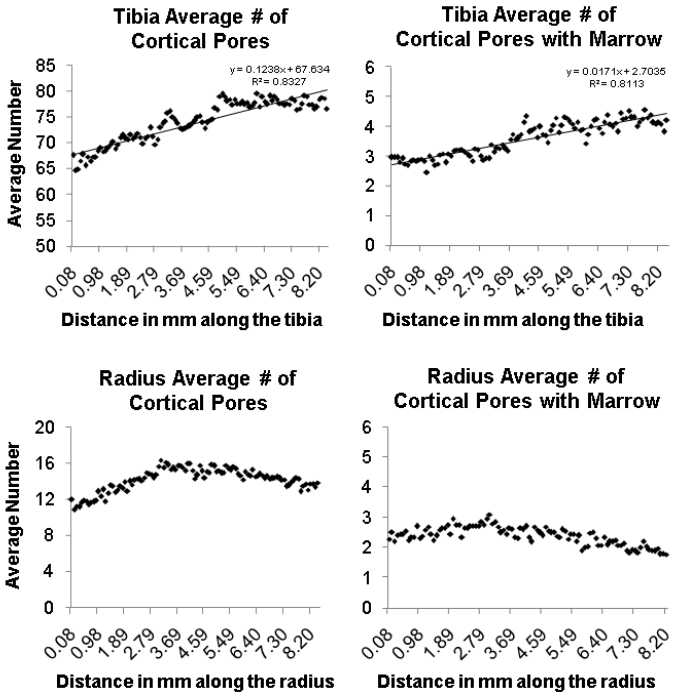

Figure 4.6: Plots of the average number of cortical pores with and without marrow with distance from the joint line (distal to proximal) for the radius and tibia. There was an increasing trend determined for the tibia ($p<0.001$) and no trend found for the radius($p>0.05$).

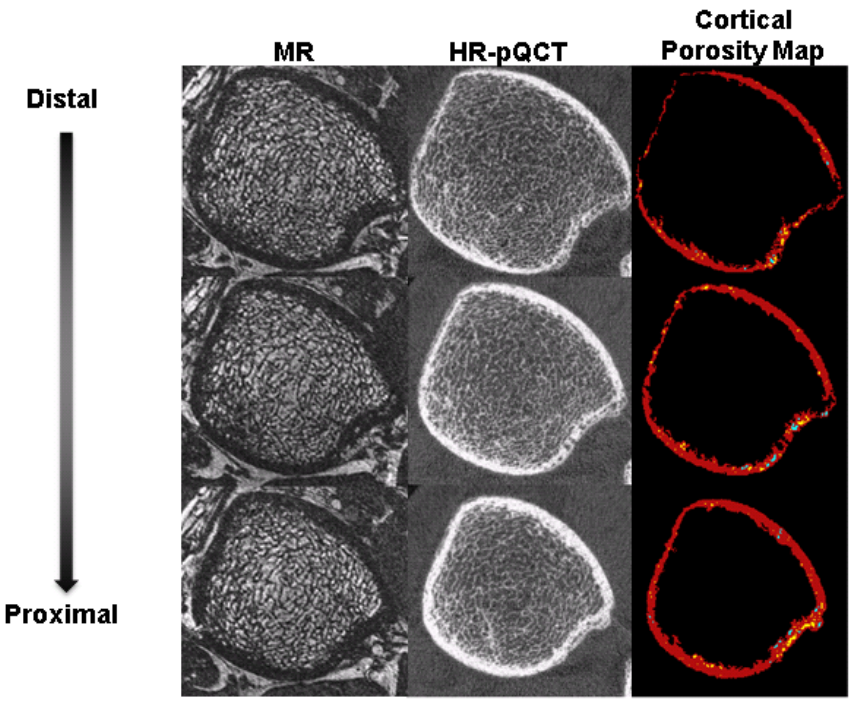

Figure 4.7: Axial images starting with the most distal slice through the most proximal slice in the analysis region for one subject. The MR images depict cortical and travecular bone as signal void and marrow as higher in intensity, while the HR-pQCT depict bone as higher in intensity. The cortical porosity map shows cortical bone in red, cortical pores without marrow in yellow, and cortical pores with marrow in blue.

4.4 Discussion and Conclusion

In this study, we examined cortical porosity using images of both HR-pQCT and MR of the distal tibia and distal radius of postmenopausal osteopenic women. All HR-pQCT images contained cortical porosity in both the tibia and the radius. By combining the HR-pQCT and MR images, the data revealed that all subjects had cortical pores which both contained and did not contain bone marrow. The data suggest that cortical pore spaces may contain different components. This implies that there may be more than one mechanism for the development of cortical porosity and more than one type of bone fluid present in cortical pores.

While most previous studies have focused on ex vivo examinations of the cortical porosity of the femoral shaft (68,69,72), this study is the first study to examine cortical

porosity of the tibia and radius using two complimentary in vivo imaging techniques. Jordan et al. (72) found an average percent cortical porosity of 10.72%±4.2 in femoral shaft biopsies using histology sections. Similarly Cooper et al.(68) reported an average percent cortical porosity of 9.82%±9.19 in femoral shaft specimens from females using micro-CT imaging and morphological analysis. The percent cortical porosity in this study is lower, 4.36%±1.6 for the tibia and 1.6%±0.8 for the radius. The reason for the difference is likely due to the difference in imaging and analysis methods, anatomical region analyzed, or fracture status. Histology sections have a much higher resolution than HR-pQCT and can therefore visualize smaller cortical pores, which accounts for the higher porosity measurement using histology sections. The smallest pore area that can be measured on the HR-pQCT is 0.0067 mm^2 due to resolution constraints, while cortical porosity at the scale of lacunae and canaliculi can have diameters as small as 10 μm and 0.5μm respectively(96,97). Additionally, the femur, the tibia, and the radius have different mechanical environment and may therefore have different metabolic activities which may illustrate why the radius has a lower percent of cortical porosity. Cortical porosity in this study was determined from in vivo images of postmenopausal women who had not sustained a fracture while previous studies determined cortical porosity from fractured femoral neck biopsies of women or femoral midshaft specimens of male cadavers. This difference in fracture status or gender may impact the percent of cortical porosity observed.

Alendronate and risedronate are second and third-generation bisphosphonates that have been shown to reduce hip fractures in postmenopausal women(16,98,99). Studies have demonstrated that alendronate inhibits osteoclastic bone resorption, reduces bone

turnover, increases hip BMD, produces more uniform mineralization in cortical bone, and decreases cortical porosity(16,28,98,100). Roschger et al.(28) observed a 46% reduction in cortical porosity in an alendronate-treated group compared with a placebo-treated group which highlights the importance of cortical porosity in overall bone quality maintenance. Similarly Borah et al.(101) recently reported a 18 to 25% reduction in cortical porosity in a risedronate-treated group compared with no reduction in a placebo-treated group. Determining how cortical porosity changes in response to aldendronate treatment is important in assessing drug efficacy. However, the images in this study were acquired prior to alendronate treatment and longitudinal changes in the amount of cortical porosity and the visualization of bone marrow within cortical pores will be assessed after follow-up analysis is performed.

Cortical porosity was visualized with and without bone marrow in every subject in this study. There was a large range in the percent of cortical porosity with bone marrow across subjects. While the amount of cortical porosity ranged from 2.1% to 9.2% in the tibia and 0.4% to 5.0% in the radius across all subjects, the range of percent of porosity containing marrow was much higher, 1.6% to 21.0% in the tibia and 4.96% to 41.75% in the radius. This suggests that while the amount of cortical porosity did not vary greatly between subjects, the type of cortical pore, containing bone marrow versus not containing bone marrow, varied highly between subjects. Additionally, the number of cortical pores containing bone marrow did not depend on the percent of cortical porosity and pores for all visible cortical pore areas (>0.0067 mm^2) were observed with and without bone marrow (figure 4.4). The regional variation in tibia cortical porosity observed in this study (figure 4.6) may have considerable impact when assessing cortical

porosity using a single slice technique and also demonstrates the importance of consistent analysis regions in longitudinal or cross-sectional studies investigating cortical porosity.

Bone fluids within the bone cavities of the cortical bone have been assumed to be homogeneous across all cavities(84). Although the viscosity and compressibility of the bone fluid has never been measured, it is assumed to behave like salt water(83,84,102). However, this study suggests there may exist variability in bone fluid composition. Since the viscosity and compressibility of the bone fluid impact the hydrostatic strengthening (HS) of cortical bone(83,85), knowledge of bone fluid composition and distribution may help improve the accuracy of HS models and further help predict bone strength.

Bone marrow consists of both hematopoietic (red) and fatty (yellow) components. Red marrow consists of approximately 40% water, 40% fat and 20% protein while yellow marrow consists of approximately 15% water, 80% fat, and 5% protein(103). Normal physiological conversion to the adult pattern, conversion from red to yellow marrow, completes by the age of 25 at which time red marrow is predominantly concentrated in the axial skeleton and yellow marrow is predominately concentrated in peripheral regions such as the tibia and radius(104,105). When imaging bone marrow using MR, fat is the predominate contributor due to its short T1 relaxation time compared with the longer T1 relaxation time of water(106). Due to this difference, yellow marrow appears much brighter on an MR image with T1 weighting(107). The assumption for peripheral regions, such as the tibia and radius, is that all marrow present is yellow marrow. However, the possibility that red marrow may be present cannot be eliminated and exact percentage of fat within the marrow is unknown, as well as the amount of saturated, monounsaturated, and polyunsaturated triglycerides. Proton MR spectroscopy is a

promising tool for determining the composition of bone marrow(108,109) and Ultrashort TE (UTE) pulse sequences have been shown to visualize tissues with a very short T2 relaxation component(110,111) which may be helpful in future studies to determine the exact constituents of the bone marrow fluid in cortical pores. In this study, cortical pores visualized without bone marrow may be likely to contain bone fluid with a high water content and therefore a longer T1 which results in a loss of MR signal. However, further studies are warranted to fully explain the loss of MR signal observed in many of the cortical pores.

Cortical pores containing bone marrow are not likely to be large haversion canals with blood vessels but rather resorption spaces that been infiltrated by bone marrow. Most likely these are resorption spaces in the cortex that have broken the endosteal boundary allowing the infiltration of bone marrow. While this study evaluated cortical porosity using two dimensional techniques, a three dimensional analysis of the cortical porosity may clarify whether cortical pores containing marrow connect to the trabecular bone marrow compartment. Additionally, a previous study has shown that cortical bone loss may vary spatially(112). A future direction may be to assess the primary location of cortical porosity and the spatial distribution of cortical pores containing marrow versus cortical pores not containing bone marrow. Previous studies have demonstrated that age is highly correlated with increased cortical porosity(68,113-115), therefore an additional future direction may be to assess the relationship between age and the percent of cortical pores containing marrow.

There were several limitations in this study related to imaging and post-processing restrictions. Davis et al. (93) describe inaccuracies of the cortical bone

segmentation which is highly dependent on the gaussian blurring step to smooth the finer trabecular bone structure. This dilution may cause thin segments of the cortex and highly porous regions of cortical bone to be identified as trabecular bone. Therefore, cortical pores in this study that were located inside thin segments of the cortex, within highly porous regions, or closer to the endosteal surface may have been excluded and this study may underestimate the actual amount of cortical porosity. Additionally, MR images are acquired at a lower resolution than the HR-pQCT images and then resampled to match the HR-pQCT image resolution. Therefore due to partial volume effects, marrow in some pores may not have been visualized while marrow in cortical pore sizes less than 0.024 mm^2 (the resolution of the original MR image) may be exaggerated. However, we propose that our technique is able to successfully visualize the presence of bone marrow in the majority of cortical pores and within these cortical pores, estimate the number and size of cortical pores containing bone marrow.

This promising first study observes cortical porosity in vivo in postmenopausal osteopenic women and combines data from two different imaging modalities, HR-pQCT and MRI to further study the nature of cortical porosity. Data suggest that cortical porosity in the distal tibia and distal radius is prevalent in this population and that the constituents of cortical pore fluid may vary. The number of cortical pores containing bone marrow varies between subjects but is not dependent on the amount of cortical porosity. Future investigation will be required to fully examine and interpret the observations in this study and to determine whether the spatial distribution of bone marrow in cortical porosity has an impact on bone strength.

Chapter 5

Three-dimensional image registration of MR proximal femur images for the analysis of trabecular bone parameters

5.1 Introduction

The proximal femur is the most important site for osteoporotic fractures. After six months 85% of osteoporotic hip fracture patients need assistance with walking (cannot walk across a room without help) and 20% of patients die within one year(116). Assessment of osteoporosis at the proximal femur is typically performed using areal bone mineral density derived from dual energy x-ray absorptiometry (DXA); this technique measures the combined mineral density of both cortical and trabecular bone(117). To better characterize early bone loss and increased fracture risk a noninvasive technique to assess trabecular architecture would be desirable. However, until recently there existed no method without ionizing radiation to access in vivo, non-invasively, three dimensional trabecular bone structure of the proximal femur. Previously, high-spatial resolution MR imaging of trabecular bone was restricted to peripheral sites, and deep-seated regions of the skeleton such as the proximal femur were limited by signal to noise ratio. Due to advances in MR pulse sequence development and higher magnetic field strength (3 Tesla), recent studies have been conducted which investigated the feasibility of using high-spatial resolution MRI to evaluate trabecular bone structure of the proximal femur and promising results were found(118),(119). If bone loss or response to therapy is monitored in a longitudinal study, consistent positioning between baseline and follow-up proximal femur scans is required but it is very difficult due to the complex femoral shape. Primary sources of error for MR-derived trabecular bone parameter reproducibility were

previously identified in the distal radius and the distal tibia as involuntary patient motion and failure to accurately match the analysis volumes(120). Despite the complex femoral shape, the same region must be consistently scanned and analyzed between baseline and follow-up image acquisitions.

Image registration may be able to ensure correct volume of interest (VOI) selection for analysis. Techniques for image registration of MR musculoskeletal images have been reported in recent scientific literature(121,122), however they are not fully automatic since they involve image segmentation. The considerable amount of textural information and limited contrast inherent in high-spatial resolution trabecular bone images makes segmentation time consuming and difficult making the registration technique prone to fail. Investigators have implemented a mutual information registration technique(89,90) which requires no segmentation for the registration of brain MR images(123). This same technique was first adapted to make automatic registration possible for trabecular bone images of the distal tibia(124) and later successfully modified to incorporate a cross correlation metric(125).

Image registration involves transforming an image, which requires interpolation of the voxel intensities to produce a new image. Since gray-value errors are commonly introduced by interpolation, it is also necessary to evaluate the effects of interpolation on the measurement of trabecular bone parameters.

Thus the purpose of this investigation was fourfold:

(i) to evaluate the feasibility of proximal femur automatic image registration in short-term and long-term studies

(ii) to compare the effects of three methods of gray-level interpolation on MR-

derived trabecular bone parameters

(iii) to determine the effect of misalignment of VOIs between repeat scans on MR-derived trabecular bone parameters

(iv) to assess the difference in the coefficient of variation (CV) between MR-derived trabecular bone parameters determined from follow-up images with and without automatic image registration in a short term study

5.2 Methods

5.2.1 MR Imaging

Coronal MR scans of the right proximal femur were obtained with a 3 Tesla Signa system (General Electric, Milwaukee, WI, USA) using a four-element phased array coil and a multi-acquisition balanced steady state free precession (b-SSFP) sequence. Image acquisition and reconstruction were performed using a modified version of generalized autocalibrating partially parallel acquisition (GRAPPA), with an acceleration factor of two(126). Scans were acquired with a 512x384 matrix, 12cm FOV, 60º flip angle, TR/TE 10.3/3.6 ms, 1 mm slice thickness, a total of 74 slices and a scan time of approximately 10 minutes. Image voxel size was 0.234 x 0.234 x 1 mm^3. Figure 5.1 shows a representative high-spatial resolution MR image of the proximal femur. Because the orientation of the femur can vary dramatically based on the rotation of the foot, a color-

Figure 5.1.: Representative high-spatial resolution (0.234 x 0.234 x 1mm^3) image of the proximal femur. A rectangular parallelepiped masked the baseline image for the calculation of entropy (shown in orange). It was created by selecting a point on the first slice in which the greater trochanter appeared and last slice before the greater trochanter was no longer in view. The analysis region is outlined in red.

coded coil holder and foam foot wedge were used to provide limit the variation in coil and limb positioning during scanning to ±10mm and ±10 degrees (figure 5.2).

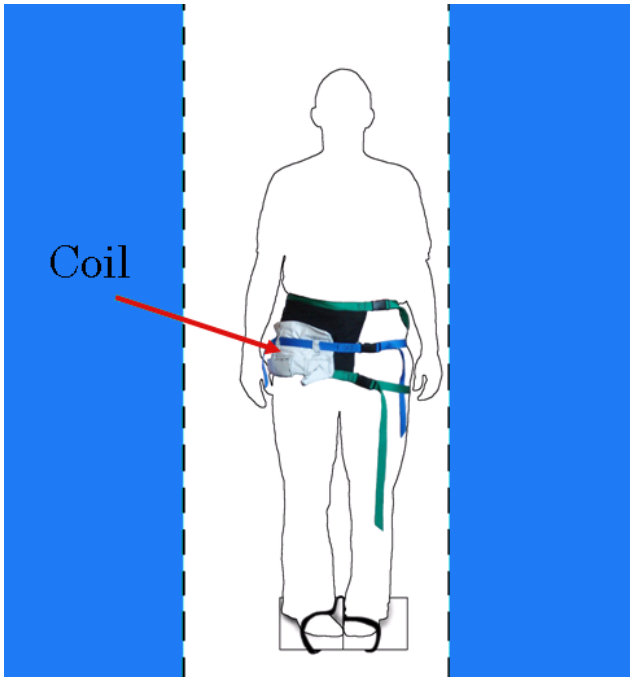

Figure 5.2.: Schematic of the coil holder and foam foot wedge used to ensure limit coil and limb positioning to ±10mm and ±10 degrees. Figure courtesy of Dana Carpenter.

Six healthy volunteers (age 26 ± 4 years) participated in a short-term study in which the baseline and follow-up images were acquired on the same day after repositioning. After baseline image was acquired the volunteer was removed from the scanner, allowed to rest for 15 minutes, and then repositioned for the follow-up scan. One of the volunteers was scanned twice without repositioning in order to assess the robustness of the registration algorithm to the capture range

. Additionally 10 patients (age 55 ± 4 years) were scanned for a long-term study in which the baseline and follow-up images were acquired one year apart in order to assess the feasibility of registration for a longitudinal time series.

5.2.2 Registration Approach

Image registration is the process of aligning two images. The goal is to find a transformation that aligns or matches the anatomical regions of the two images. A rigid transform with a rotation matrix, characterized by three Euler angles, and a translation vector composed of three translation parameters was used to align the proximal femur images. The rotation matrix and the translation vector defined the movement of a point from one image to the other, and image registration was performed by adjusting their parameters. The parameters were adjusted until a mutual information measure function was optimized and the transformation therefore aligned the two images. Mutual information registration with a conjugate gradient descent optimizer and a linear interpolator was performed using open-source image registration software (Insight Toolkit)(127). Registration was applied off-line retrospectively to the high-spatial resolution follow-up images to align them to their corresponding baseline images. Registration was performed on the images from the six volunteers with a short term follow-up and on the ten patients whose follow-up exam was a year later.

We assessed the robustness of the registration to the capture range using the same technique presented by Studholme et al.(91) using the image set with the follow-up image acquired without repositioning. We defined a series of 90 mis-alignments. Thirty of these corresponded to a mis-alignment by translation of 5mm and a rotation of 5^{o}, thirty by 10mm and 10^{o}, and thirty by 10mm and 20^{o}. Each set of thirty mis-alignments was determined by randomly selecting a point on the surface of spheres in translational and rotational parameter space. Each mis-alignment was selected as the initial starting guess for the registration. The deviation from the expected output was recorded.

5.2.3 Interpolation Approach

When a transform is applied to an image, resampling is required because the new coordinate points may not line up with the old coordinate points. In this study, all interpolation was performed using open-source image registration software (Insight Toolkit).

The registration algorithm implemented in this study used linear interpolation. The goal of the registration algorithm was to align the shape of the femur in the baseline and follow-up images. The texture information inherent to trabecular bone was not important for alignment and therefore the smoothing due to the linear interpolation is desired. However, for quantifying the trabecular bone structure, preserving the texture information in the image is paramount. Therefore a key step in aligning proximal femur images for trabecular bone structure analysis was the selection of the interpolation for the final transform.

To examine the effect of registration on trabecular bone structure parameters the registration outputs from the six sets of images from the short-term study were used. The output of the mutual information registration algorithm, three rotations and three translations, was applied to the follow-up image with different interpolators. Nearest-neighbor interpolation, trilinear interpolation(54), the extension of linear interpolation to three dimensional spaces, and a fifth order B-spline were compared. The same order of B-spline was used for each dimension and mirror boundary conditions were used(128).

Registration and interpolation were performed on a Sun workstation (Sun Ultra 40, AMD Opteron Dual Core processor, 2.4 Ghz, 8 GB RAM, Sun Microsystems, CA).

The three interpolation methods were compared by analyzing their effect on bone parameters and computational time.

5.2.4 Trabecular Bone Analysis

Proximal femur trabecular bone structure analysis was performed on the images using software developed at our institution implemented in IDL (Research Systems, Inc., Boulder, CO)(95). A VOI which included only trabecular bone and bone marrow contained between the epiphyseal line and the cortex of the greater trochanter (Figure 5.1), consisted of ten slices and was manually defined using a graphics cursor on a slice by slice basis. The same VOI was used on the baseline and registered follow-up images. The un-registered follow-up required a separate VOI definition. Due to the use of surface coils, a correction for the spatial variation in the coil detection sensitivity was required for accurate image analysis. The VOIs were intensity-corrected using a low-pass-filter based coil sensitivity correction(95). An image intensity histogram based thresholding technique was used to binarize the VOI into trabecular bone and marrow phases, and previously described methods(129) were then used to compute the apparent trabecular bone structural parameters: App.BV/TV, App.Tb.Sp, App.Tb.Th, and App.Tb.N.

5.2.5 Error Simulations

Error simulations were performed to demonstrate the influence of VOI location on MR-derived bone parameters and the importance of accurately aligning the VOI in baseline and follow-up images. The bone parameter variation associated with a shift in the analysis volume along the slice direction (anterior-posterior) was estimated. For one proximal femur image from the short term study, a VOI spanning 10 slices was shifted in

one-slice increments. Bone parameters were calculated for the VOI at each increment and the percent variation in trabecular bone parameters from the initial VOI position was calculated. To help explain why MR-derived bone parameters are affected by VOI location, regional variations in MR-derived trabecular bone parameters for the proximal femur were determined. MR-bone parameters, App.BV/TV, App.Tb.Sp, App.Tb.Th, and App.Tb.N were measured over a region of 1.5 cm thickness for all of the baseline proximal femur images from the short term study. The average percent variation in bone parameters was calculated.

5.2.6 Statistical Analysis

MR-derived apparent trabecular bone structural parameters determined for the short-term study with each of the three different gray-level interpolators were compared and analyzed using repeated measures of analysis of variance and the Bonferroni t-test. The coefficient of variation(130) was calculated between the baseline and follow-up images with and without image registration for the images in the short-term study.

5.3 Results

The total time to register a baseline and follow-up proximal femur image and save the transformation, including uploading the images and applying a mask, is approximately 5 minutes. The parameters of the transforms that resulted from the registration algorithm in the short-term study are shown in Table 5.1 and the long-term study in Table 5.2. Rotations and translations for both the short term and long term studies were in the same range. Short term rotations ranged from -7.74 ^{o} to 16.83 ^{o} and

long term rotations ranged from -8.32 ^{o} to 19.65 ^{o}. Short term translations ranged from -9.9mm to 9.85mm and long term translations ranged from -8.3mm to 7.88mm.

Table 5.1: The output of the registration algorithm, a transform with three translations and three rotations for the six subjects in the short-term study. The three planes are defined as Right/Left (R/L), Anterior/Posterior (A/P), and Inferior/Superior (I/S).

	R/L Trans (mm)	A/P Trans (mm)	I/S Trans (mm)	R/L Rot (^{o})	A/P Rot (^{o})	I/S Rot (^{o})
Subject 1	1.60	-3.33	-9.90	5.88	-2.69	14.19
Subject 2	-3.26	2.58	-0.09	-3.79	1.66	2.45
Subject 3	3.45	-1.62	1.77	2.58	-2.45	-5.70
Subject 4	9.85	4.34	-1.95	4.65	-1.78	16.83
Subject 5	3.59	-0.89	-4.55	-0.85	2.31	-7.74
Subject 6	5.67	-5.39	2.58	-1.49	-0.59	8.98
Average	3.48	-0.72	-2.02	1.16	-0.59	4.84
Standard Deviation	4.34	3.63	4.64	3.80	2.13	10.23

Table 5.2: The output of the registration algorithm for the ten subjects in the long-term study.

	R/L Trans (mm)	A/P Trans (mm)	I/S Trans (mm)	R/L Rot (^{o})	A/P Rot (^{o})	I/S Rot (^{o})
Subject 1	2.59	-1.35	1.23	-0.82	-2.13	6.19
Subject 2	-1.76	-0.86	-1.82	-3.51	-4.87	-2.96
Subject 3	-8.3	-1.53	0.92	5.1	2.13	-4.6
Subject 4	0.25	-1.64	5.4	19.65	1.85	-1.43
Subject 5	-1.92	-1.06	0.68	-0.09	0.41	1.15
Subject 6	-5.58	-4.78	-2.95	13.21	0.2	-2.24
Subject 7	-3.13	0.66	5.97	-0.6	5.14	-0.7
Subject 8	0.72	0.06	7.88	-6.35	-1.29	-8.32
Subject 9	0.36	-3.29	-0.8	-7.6	1.04	1.33
Subject 10	5.6	-2.3	5.85	0.1	-2.8	-2.8
Average	-1.12	-1.61	2.16	1.91	-0.03	-1.44
Standard Deviation	3.98	1.57	3.86	8.57	2.86	3.88

Figure 5.3 shows the results of the registration with subtraction images and surface renderings from two femurs. Figure 5.3a-d show results for a femur from the

short term study and Figure 5.3e-h show results for a femur in the long term study. As can be assessed by simple image subtraction in Figure 5.3a and 5.3c, and by surface rendering of the proximal femurs in Figure 5.3b and 5.3d, the follow-up image is better aligned to the baseline scan after registration. In Figure 5.3a and 5.3e the edges of the cortical bone are misaligned with higher intensities in the difference image, and clear separation of the red and green femoral renderings in Figure 5.3b and 5.3f is visible. In Figure 5.3c and 5.3g, the high intensity differences within the femoral edges are reduced, and there is considerable more overlap in the red and green femoral renderings in Figure 5.3d and 5.3h. The results from the assessment of the robustness of the registration to the capture range are show in Table 5.3. For the 30 mis-registrations of 5mm and 5^{o} the root mean square error (RMSE) for translations and rotations in Right/Left (R/L), Anterior/Posterior (A/P), and Inferior/Superior (I/S) were within half a pixel and half a degree. For the mis-registrations of 10mm and 10^{o} and 10mm and 20^{o} the RMSE for translations in R/L, A/P, and I/S were within one pixel, while the RMSE for rotations in R/L and A/P were within one degree and the rotations in I/S were within 1.75 degrees. Outside of a translation of 10mm and a rotation of 20^{o} the registration algorithm fails and is not able to align the images.

Figure 5.3: Comparison of follow-up with registration versus follow-up without registration for the short term study (a-d) and the long term study (e-h). (a and e) Subtraction of baseline and follow-up without registration. (b and f) 3D rendering of non-registered proximal femur surfaces (c and g) Subtraction of baseline and registered follow-up (d and h) 3D rendering of registered proximal femur surfaces (green= baseline, red= follow-up)

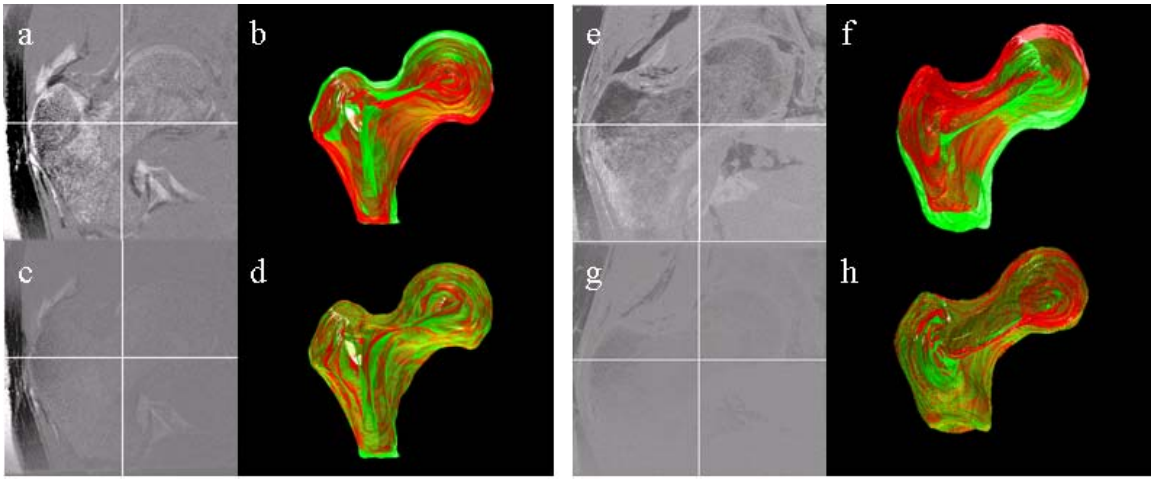

Table 5.3: The results from testing the robustness of the registration algorithm to the capture range. The average, standard deviation (St.Dev), and the root mean square error (RMSE) with respect to the expected output are shown. Initial mis-alignments of 5mm and 5°, 10mm and 10o, and 10mm and 20o were used.

		R/L Trans (mm)	A/P Trans (mm)	I/S Trans (mm)	R/L Rot (°)	A/P Rot (°)	I/S Rot (°)
5mm and 5°	Average	0.08	-0.04	-0.06	0.22	0.15	0.02
	St.Dev	0.07	0.27	0.11	0.30	0.14	0.32
	RMSE	0.10	0.26	0.12	0.36	0.24	0.31
10mm and 10°	Average	0.10	-0.22	-0.08	0.29	0.09	0.35
	St.Dev	0.14	1.02	0.18	0.43	0.22	1.40
	RMSE	0.17	1.02	0.20	0.51	0.26	1.42
10mm and 20°	Average	0.04	0.29	-0.17	0.63	0.07	-0.30
	St.Dev	0.22	1.28	0.12	0.80	0.19	1.74
	RMSE	0.22	1.30	0.20	1.00	0.22	1.74

The computation time for nearest neighbor interpolation and linear interpolation was less than 12 seconds, while for b-spline approximation the computation time was on average 9 minutes. The effects of different gray-level interpolators on trabecular bone parameters in the short term study are shown in Figure 5.4 and Figure 5.5. Trabecular bone structure parameters determined from follow-up images without and with automatic image registration using linear, nearest-neighbor, and b-spline kernels are shown in

Figure 5.4. Because no interpolation was performed when bone parameters were determined from baseline images, these images served as the reference value. The difference from the reference value for each of the interpolators is shown in Figure 5.4. All bone parameters were significantly different from the reference ($p<0.01$) with linear interpolation. However, nearest-neighbor interpolation and b-spline approximation resulted in no significant difference from the reference ($p>0.05$).

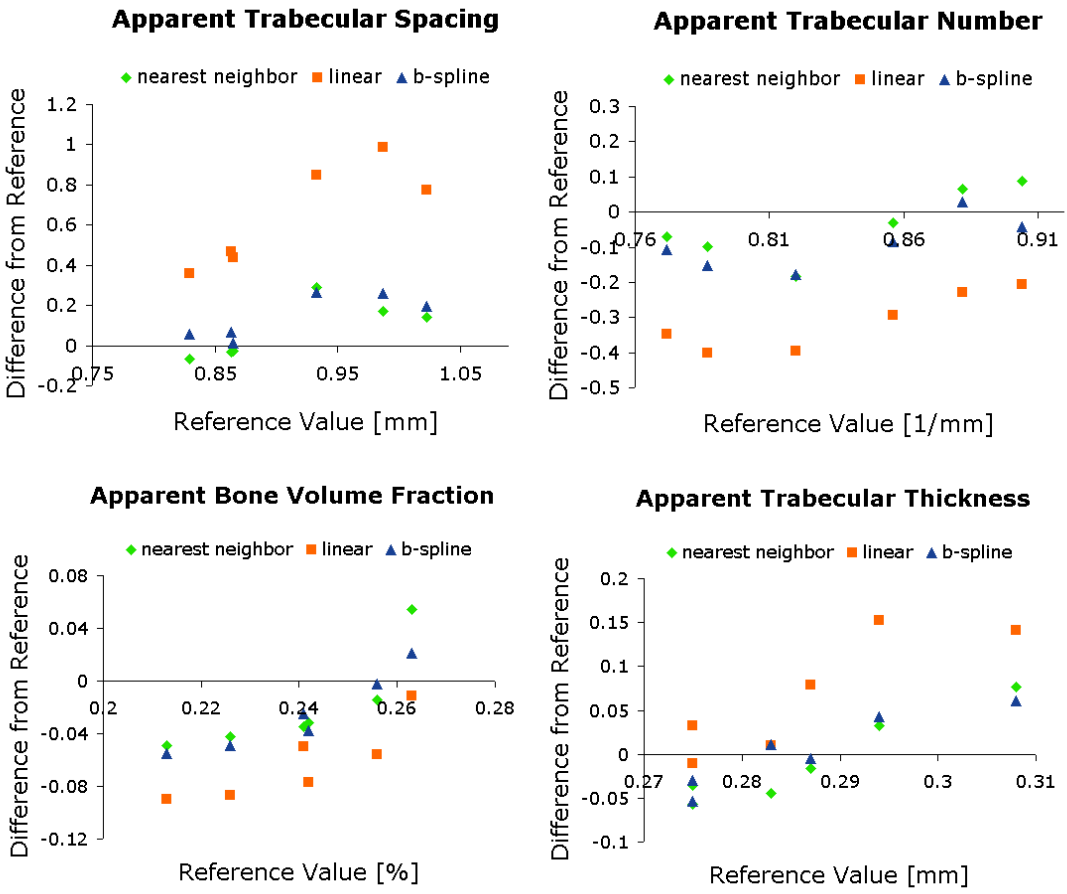

Figure 5.4: Assessment of different interpolators on the four trabecular bone structure parameters analyzed for the six subjects of the short-term study. Values determined from images with a linear interpolation were significantly different ($p< 0.01$), but b-spline approximation and nearest-neighbor interpolation did not change trabecular bone structure parameters significantly ($p>0.05$).

Additionally, in Figure 5.5 the effects of the gray-level interpolation can be assessed visually. Figure 5.5 shows that nearest-neighbor interpolation blurs out some of the trabeculae in some areas and exaggerates the trabeculae in others, but overall, the same number of pixels are designated to be bone as the in reference image. B-spline approximation maintains the most of the trabecular structure and therefore results in the same bone parameter measurements as the reference image. Linear interpolation clearly blurs out portions the trabecular structure causing the spacing between the trabeculae to increase and the number of trabeculae to decrease.

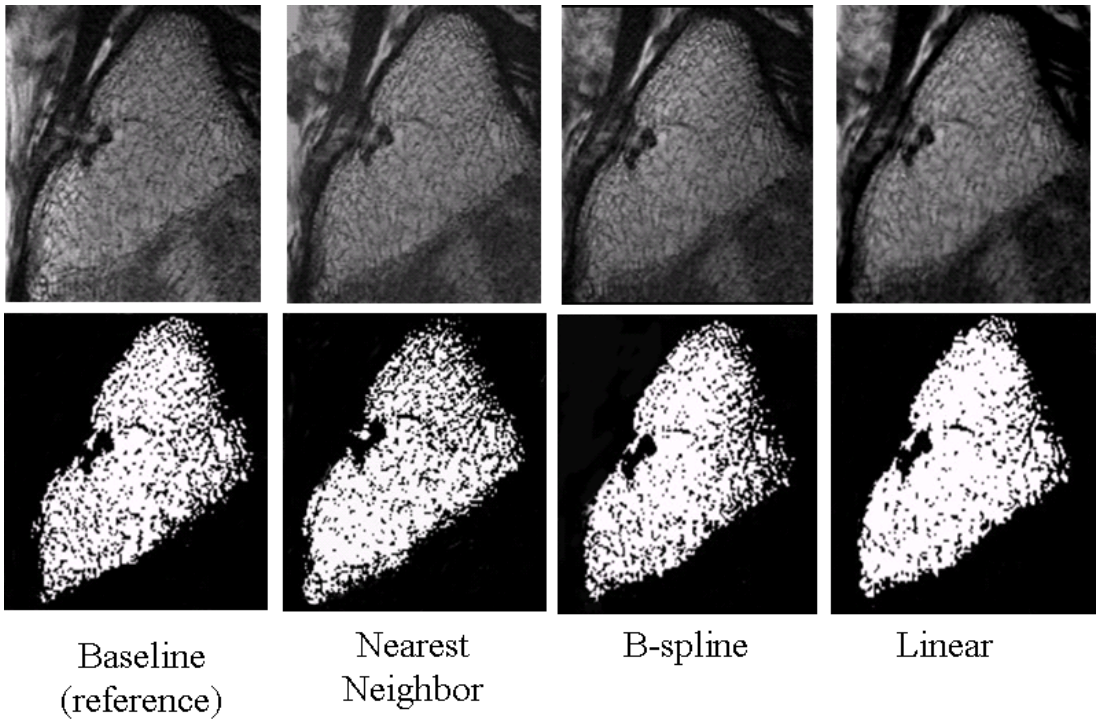

Figure 5.5: The effects of the gray-level interpolation can be assessed visually. One of the steps in the trabecular micro-architecture quantification process is thresholding to create a binary image. The top row displays the gray-scale image and the bottom row displays the same image after thresholding. The baseline image, which served as the reference image, and registered follow-up images with linear interpolation, nearest-neighbor interpolation, and b-spline approximation for the final transform are shown.

Reproducibility of bone parameters between the repeat scans in the short term study is shown in Figure 5.6. The CV was slightly better for registered follow-up images

than for non-registered follow-up images. The CV improved 0.48%-1.25% when the baseline images were compared to the registered follow-up images versus follow-up images without registration. However, the improvement in CV was not statistically significant ($p>0.05$).

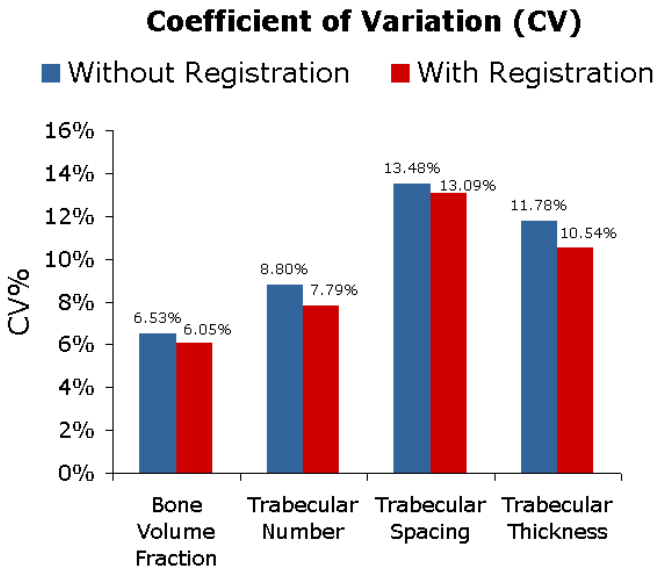

Figure 5.6: The improvement in coefficient of variation (CV) between baseline and follow-up due to registration (between 0.39% and 1.25%) was not statistically significant.

Average errors from a slice offset in VOI placement were significant (Figure 5.7a). The change in App.BV/TV, App.Tb.N, and App.Tb.Th increased linearly with a shift in the VOI along the slice (A/P) direction, while the change in App.Tb.Sp decreased linearly. The average percent change in bone parameters associated with a shift in the VOI along the slice direction was up to 6.37%. App. BV/TV and App.Tb.Sp had a higher percent change (over 5.7%) than App. Tb.N and App.Tb.Th (less than 3.6%).

Effects due to slice location within the proximal femur VOI were also significant (Figure 5.7b). App.BV/TV and App.Tb.N. increased, App.Tb.Sp. decreased, and

App.Tb.Th. remained fairly constant while moving anterior to posterior through the proximal femur image. The average percent change in bone parameters was up to 15.73% between the first and last slices.

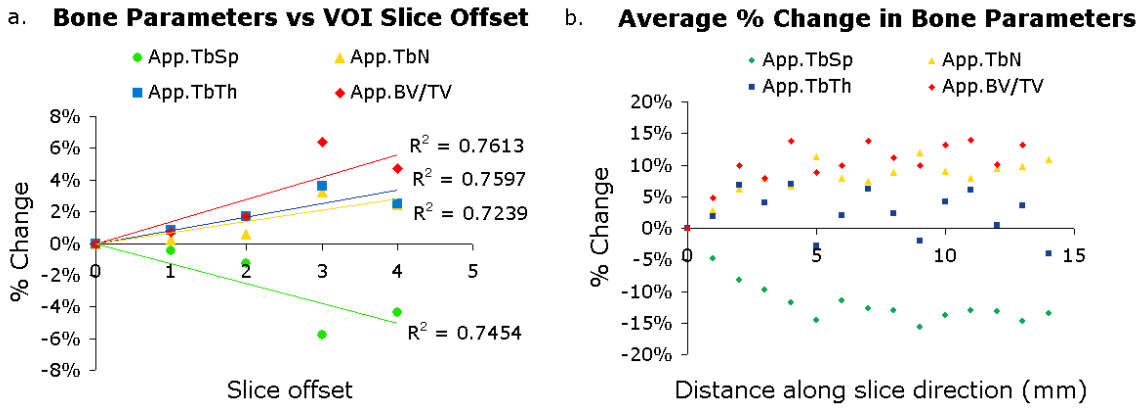

Figure 5.7: Results of error simulations. a) As the VOI was placed in shifted locations along the slice direction (a slice offset), the bone parameters changed up to 6.37%. b) Within the same VOI, bone parameters have a dependence on the slice position demonstrating the trabecular structural heterogeneity in the proximal femur. The average percent change in bone parameters across a VOI is up to 15.73%.

5.4 Discussion and Conclusion

The study of the progression of metabolic bone diseases or the efficacy of a treatment requires the proper analysis of corresponding regions of interest in repeat MRI scans. This study focused on the accuracy of VOI positioning for the evaluation of MR-derived trabecular bone parameters of the proximal femur. Errors due to VOI placement were assessed and quantified. This work also demonstrated the application of registration, without prior segmentation, of the proximal femur, as well as the effect of gray-level interpolators on trabecular bone parameters. Registration using the proper gray-level interpolator, such as b-spline approximation, to transform the final image may be used to avoid errors due to imprecise VOI placement.

Several investigators have observed significant variations in bone mineral content, morphometric indices, and mechanical properties within the proximal femur(19,131-

135). Brown et al. were among the first to conclude that trabecular bone of the proximal femur is a heterogeneous, anisotropic material by mapping contours of elastic modulus and yield strength(131). Morgan et al. attributed the observed variation in yield strain across anatomical sites, including the greater trochanter, to inter-site variations in trabecular structure(133). In their structural analysis of the greater trochanter, Link et al. noted that the trabecular structure was irregular and anisotropic(135). Similarly, this study found a variation in MR-derived trabecular bone parameters in the greater trochanter of the proximal femur. The variation of trabecular bone parameters in the slice (A/P) direction suggests that there is a biologically inherent heterogeneity in trabecular bone structure in the proximal femur. This heterogeneity resulted in an average 2.01%-15.73% variation in bone parameters between slices through a VOI 10mm long. This heterogeneity in trabecular bone structure of the greater trochanter resulted in measurement errors 0.25%-6.37% when there was a slice offset in VOI placement. This source of error demonstrates the importance of accurate VOI placement. These results are in agreement with a study by Gomberg et al.(120) which found errors in trabecular bone parameters up to 7.6% in the distal radius due to a VOI mismatch along the z-axis (I/S) direction. Additionally, Newitt et al.(95) determined that analysis region misalignment caused small but significant changes in some structural parameters.

The mutual information image registration algorithm proposed for use in this application was able to successfully register images from both a short term study and a long term study. The resulting transform parameters were within the same range for both studies. When the robustness to the capture range of the registration was tested, registration was successful for mis-registrations less than 10mm and 20^{o} which was

within the translations and rotations seen in both the long term and short term study. The registration algorithm was able to align images in translation within 1 pixel and rotation of 1^{o} in plane(R/L and A/P) and 1.75^{o} out of plane (I/S). For mis-registrations of 5mm and 5^{o}, sub-pixel accuracy was achieved. Therefore the registration algorithm will be successful for any likely initial mis-alignments in short term and long term studies.

The interpolation method implemented when transforming the final image can dramatically impact the quantification of trabecular bone structure parameters. Results suggest that when applying a transform to musculoskeletal images acquired for trabecular bone quantification, nearest-neighbor interpolation and b-spline approximation will maintain the integrity of the trabecular bone parameters involved in this study. Nearest-neighbor interpolation traditionally introduces aliasing to images, so interpolation results may appear surprising. However, as part of the standard trabecular bone structure quantification femoral images are thresholded. Therefore nearest-neighbor interpolation maintains the intensity values in a VOI and maintains the number of pixels thresholded. B-spline approximation performed as expected by maintaining the accuracy of the image information. If computational time becomes an issue, then nearest-neighbor interpolation would be preferred for interpolation of registered MR musculoskeletal images for trabecular bone analysis.

Carpenter et al.(119) performed a study investigating the short-term reproducibility of trabecular bone structure parameters in the proximal femur. In the study inter-operator variability was small (3.8%) and they suggested that the CVs, ranging from 6.5% to 13.5%, may be partially due to patient repositioning and mismatched analysis volumes between baseline and follow-up images. Krug et al.(118)

found similar CVs between 2% and 10% for proximal femur trabecular bone structure parameters when volunteers were rescanned four times. Registration is able to ensure accurate VOI placement and therefore eliminate sources of error associated with the imprecision of VOI placement. In this work we have demonstrated the feasibility of using a mutual information based method to automatically register MR images of the proximal femur. Although there was only a 0.48%-1.25% improvement in the CV between parameters determined from follow-up images with and without automatic registration, the registration ensures that the reproducibility error does not originate from inaccurate VOI placement. The improvement in reproducibility and the systematic method of VOI placement with automatic registration is required to establish the adequacy of MRI techniques for longitudinal studies assessing proximal-femur trabecular bone structure.

Chapter 6

Registration of MR trabecular bone images of the proximal femur in a longitudinal study

6.1 Introduction

The proximal femur is the most important site for osteoporotic fractures(116). Due to advances in MR pulse sequence and coil development as well as higher magnetic field strength (3 Tesla), recent studies have been conducted which investigate the feasibility of using high-spatial resolution MRI to evaluate trabecular bone structure of the proximal femur and have shown promising results(118). In reproducibility studies, primary sources of error for MR-derived trabecular bone parameters have previously identified as involuntary patient motion and failure to accurately match the analysis volumes(120). In the proximal femur, consistent positioning between baseline and follow-up scans is challenging due to its complex shape. Additionally, the inherent regional variations within this anatomic site have an impact on trabecular bone structure quantification(136). Despite the complex femoral shape, the same region must be consistently scanned and analyzed between baseline and follow-up image acquisition in repeat studies for improved trabecular bone structure measurement accuracy. Automatic image registration in the proximal femur has been shown to be accurate within 1 degree and 1 pixel and is able to ensure consistent volume of interest (VOI) selection for analysis baseline and follow-up images(136). This study demonstrates the feasibility of using the same automatic image registration technique to ensure accurate VOI placement in a longitudinal study investigating changes in trabecular bone structure in postmenopausal women.

6.2 Materials and methods

6.2.1 Subjects

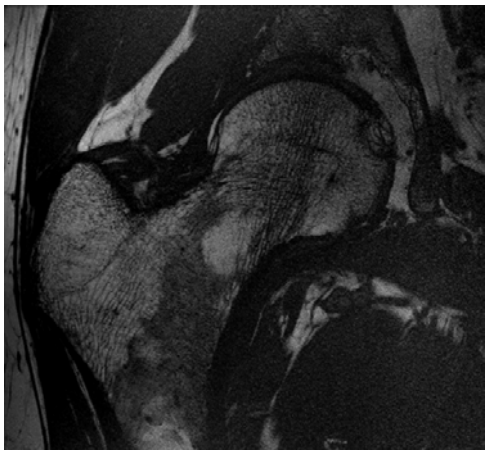

Figure 6.1: Representative high-spatial MR image of a postmenopausal osteopenic women. Note how the difference in signal intensity between red and yellow marrow.

The subjects in this study were a subset of 53 postmenopausal women recruited for a double-blind study investigating the longitudinal effects of aldendronte versus placebo on trabecular bone micro-architecture. Only women between the ages of 45 and 65 yr which had been postomenpausal for at least 1 year but not more than six years were included. They were required to be defined as osteopenic by the WHO criteria and had no history of diseases or receiving medication known to affect bone metabolism. Of the 53 women recruited only 24 women were included in this study. The study protocol was approved by the UCSF committee on Human Research and all women provided written informed consent.

6.2.2 MR Imaging

Coronal MR scans of the proximal femur were obtained with a 3 Tesla Signa system (General Electric, Milwaukee, WI, USA). The subject was scanned in the supine position using a using a four-element phased array coil (Nova Medical). A color-coded coil holder and foam foot wedge were used to provide consistent coil and limb positioning during scanning.

A multi-acquisition balanced steady state free precession (b-SSFP) using a modified version of generalized autocalibrating partially parallel acquisition (GRAPPA), with an acceleration factor of two(126) image was obtained. Scans were acquired with a 512x384 matrix, 12cm FOV, 60º flip angle, TR/TE 10.3/3.6 ms, 1 mm slice thickness, a total of 74 slices and a scan time of approximately 10 minutes. Image voxel size was 0.234 x 0.234 x 1 mm_3. Figure 6.1 shows a representative high-spatial resolution MR image of the proximal femur from this study.

6.2.3 Image Processing

Proximal femur trabecular bone images where coil corrected, registered, and analyzed (Figure 6.2). The images were coiled-corrected using a fully automatic coil corrected by nonparametric non-uniform intensity normalization(137) Image registration was performed using a mutual information registration algorithm (implemented with ITK) with a gradient decent optimizer and linear interpolator to determine the translation and rotation required to align the follow-up image to the baseline image(136). The transform which aligned the follow-up image to the baseline image was applied to the follow-up image with a Bspline

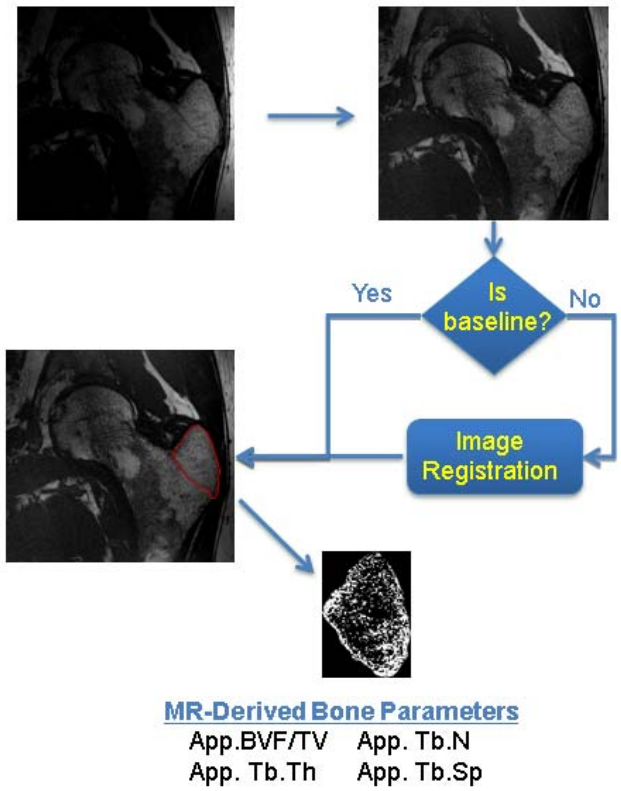

Figure 6.2: Schematic of image processing performed in this study.

approximator. Bspline approximation was previously shown to maintain the integrity of the bone parameters(136).

Trabecular bone structure analysis was then performed on the images using software developed at our institution implemented in IDL (Research Systems, Inc., Boulder, CO)(95). A VOI which included only trabecular bone and bone marrow contained between the epiphyseal line and the cortex of the greater trochanter (Figure 6.1), consisted of ten slices and was manually defined using a graphics cursor on a slice by slice basis. The same VOI was used on the baseline and registered follow-up images. An image intensity histogram based thresholding technique was used to binarize the VOI into trabecular bone and marrow phases. Previously described methods(95) were then used to compute the apparent trabecular bone structural parameters: App.BV/TV, App.Tb.Sp, App.Tb.Th, and App.Tb.N.

6.3 Results

Twenty of the twenty-four sets of images successfully registered (Figure 6.3). The average outputs from the registration of the 20 femurs were: X rotation = 1.02 $\pm$6.68^{o}, Y rotation = -1.69 $\pm$3.55^{o}, Z rotation = 0.25 $\pm$2.93^{o}, X translation = -1.06$\pm$3.1mm, Y translation = -0.92$\pm$5.00mm, and Z translation = -0.98$\pm$1.65mm. Four of the images sets failed to register due poor image quality.

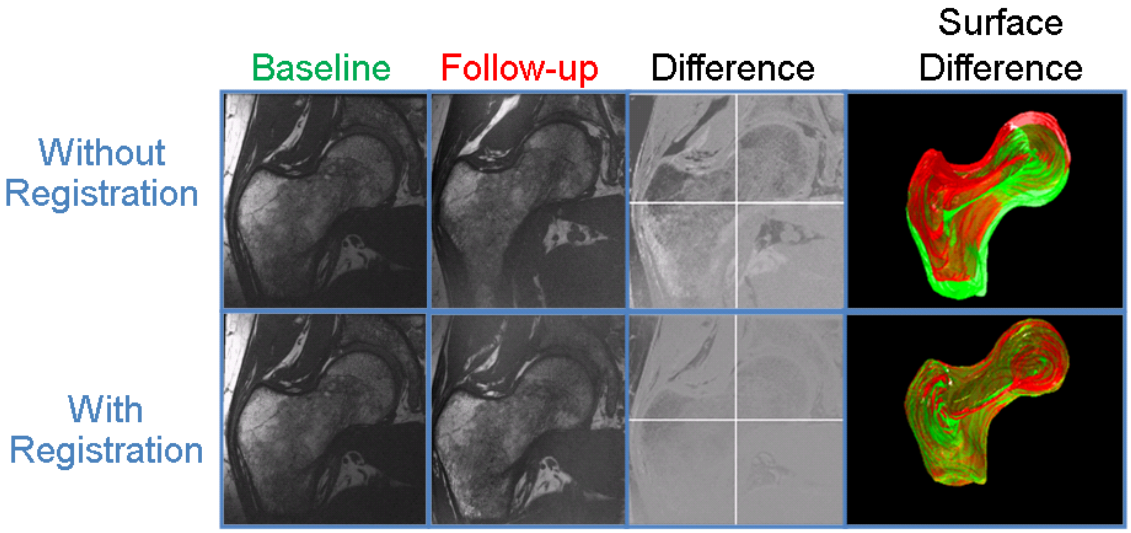

Figure 6.3: Comparison of follow-up with registration versus follow-up without registration. The difference image is subtraction of baseline and follow-up and the surface difference image is a 3D rendering of registered and non-registered proximal femur surfaces (green= baseline, red= follow-up).

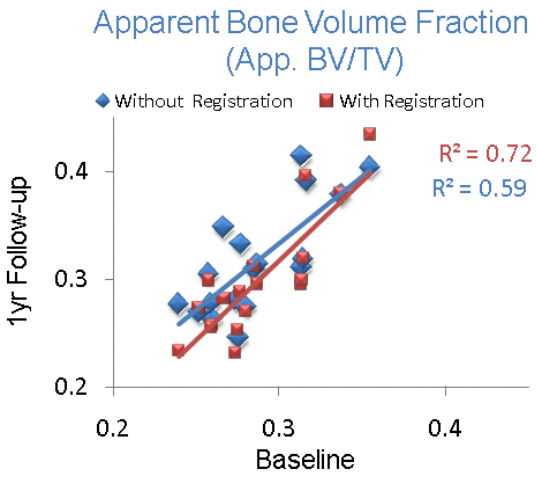

Coefficient of Determination R^2

	Without Registration	With Registration
App. BV/TV	0.59	0.72
App.Tb.N	0.48	0.68
App.Tb.Th	0.25	0.71
App.Tb.Sp	0.42	0.62

Figure 6.4: (left) Graph demonstrating the improvement in Coefficient of Determination (R2) for Apparent bone Volume Fraction. The registration has removed VOI misalignment as a source of error in the data.
Table 6.1 (right) Improvements in the Coefficient of Determination were observed for all of the bone parameters.

Bone parameters were successfully calculated for baseline and follow-up images using the same VOI. Figure 6.4 shows the improved correlation between baseline and follow-up with registration. If there are no changes between baseline and follow-up

occur we'd expect to see an R^2 value of 1. If there are changes between the two time points due to the treatment or disease progression, then the R^2 will deviate from a value of 1. However, if there are measurement errors such as biological variation or VOI misalignment the R^2 will also deviate from a value of 1. Figure 6.4 demonstrates that because image registration removes measurement error and the R^2 value App.BV/TV is improved. This trend was consistent across all bone parameters (table 6.1) and we can conclude the registration improves the measurement precision.

To further illustrate how the image registration improves the precision of trabecular bone measurements, one set of femurs was examined in detail. Figure 6.5 shows that without registration the difference between the baseline and follow-up App.BV/TV is 6.5% while the difference between the baseline and follow-up images with image registration is only 0.2%. Figure 6 shows this same image set slice by slice moving from anterior to posterior and the follow-up with registration, the aligned follow-up up image, results in App. BV/TV that follows the same trend as the baseline. The difference between the red line, the follow-up without image registration and the green line, follow-up with registration demonstrates the measurement error that is removed in the data.

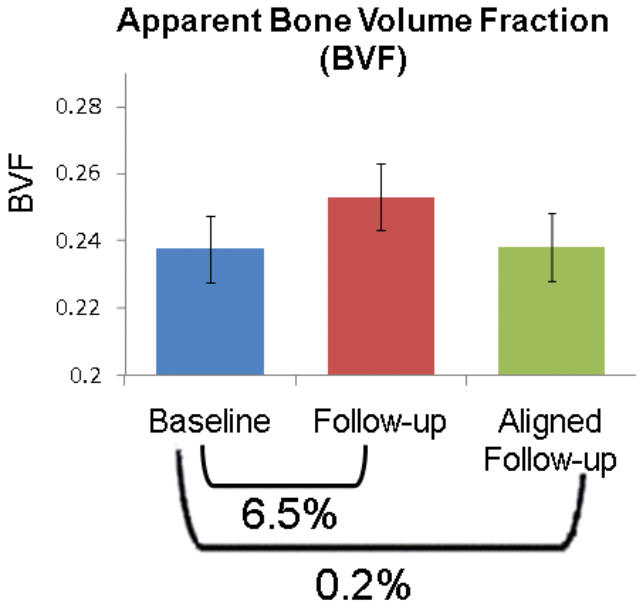

Figure 6.5: Difference in App. BV/TV in baseline and follow-up with and without registration for one subject.

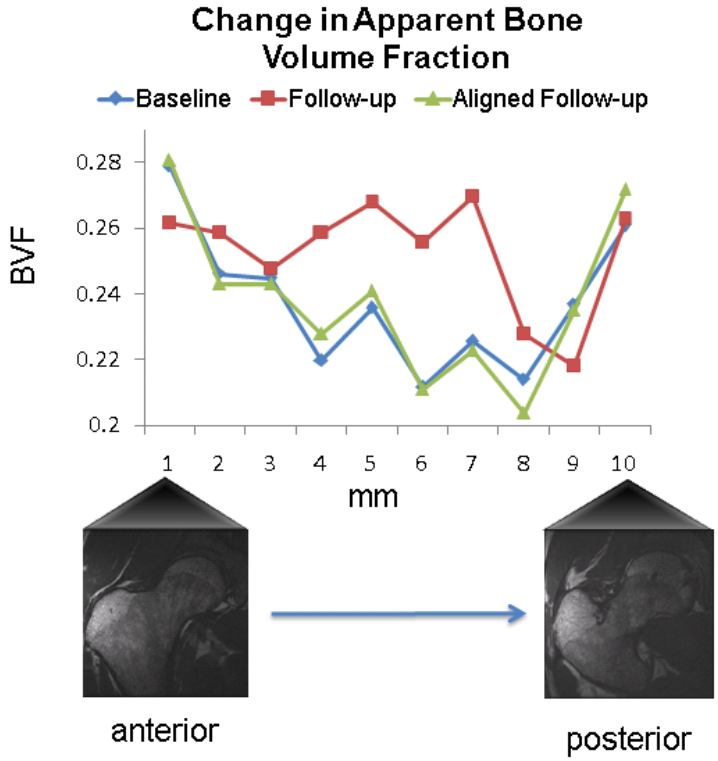

Figure 6.6: (right) Change in App. BV/TV, slice by slice moving from anterior to posterior. The difference between the red line, the App. BV/TV without image registration and the green line, the App BV/TV with image registration represents the error removed due to an aligned VOI.

6.4 Discussion and Conclusion

The study of the progression of a disease or the efficacy of a treatment based on proximal femur MRI requires the proper analysis of corresponding regions of interest in the baseline and follow-up images. This work is the first time that image registration has been implemented in a longitudinal study investigating changes in MR-derived trabecular bone structure.

In this work we have demonstrated the feasibility of using a mutual information based method to accurately register longitudinal MR images of the proximal femur. Twenty of the twenty-four sets of images successfully registered as determined by visual inspection of difference images and surface renderings. Four images failed to register due to poor image quality (low SNR) or motion artifacts (figure 6.7). Poor image quality and motion artifacts are also typical exclusion criteria in clinical studies. Therefore it is reasonable to conclude that the image registration is successful for all images of acceptable image quality.

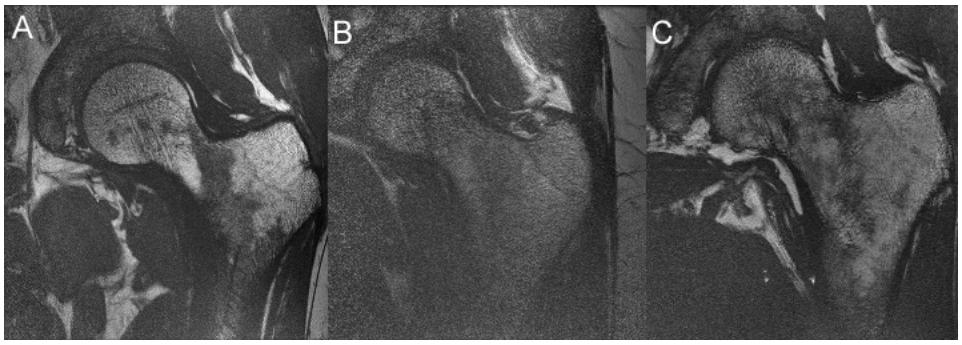

Figure 6.7: Example of a MR image of the proximal femur with (A)good image quality, (B) low SNR, and (C) motion. Poor image quality and motion artifacts similar to B and C are typical exclusion criteria in clinical studies and cause registration to fail.

Results suggest an improvement in the correlation and precision of trabecular bone structure parameters with image registration. The coefficient of determination (R^2) between baseline and follow-up measurements for all trabecular bone parameters

improved demonstrating the removal of error due to mis-aligned analysis regions. By looking at the trabecular bone parameters slice by slice, the improvement in the precision becomes more evident as shown in figure 6.6

Due to the complex shape of the femur repositing between scans at different time points is very difficult and inherent variations in the trabecular structure remain a significant source of error in longitudinal studies. This study demonstrates the feasibility of image registration in a clinical study investigating trabecular bone changes of the proximal femur and qualifies the improvement in correlation and precision due to proper selection of analysis regions between time points. Results suggest that the registration method is robust enough for longitudinal studies of the knee, wrist, and tibia.

Chapter 7

Automatic prospective registration of high resolution trabecular bone images of the tibia

7.1 Introduction

MRI scans of the distal tibia for the assessment of trabecular bone are performed according to manual prescriptions by specially trained MR technologists. The location, size, and orientation of the scanning volume requires input and adjustments by a MR technologist. A typical scanning session begins with the acquisition of a localizer san which provides an overview of the major anatomical features of the distal tibia (See figure 7.1) such as the tibia, talus, and the tibiotalar joint. The technologist then uses this localizer scan to visually prescribe the location and ortienation of the subsequent series of high resolution scans. This manual prescription is relatively time consuming taking several minutes, especially if the patient has an unusual position in the scanner. It also requires additional training for the MR technologist. Due to the nature of the localizer, technologists are not always able to fully explore all degrees of freedom, such as 3D rotations. This manual scan prescription is not entirely reproducible because it suffers from both intra and inter-operator variability in defining the extent of anatomical coverage or the slice orientation. Consequently MR scans of the distal dibia often yield scan orientations and coverage that vary from one patient to another. Therefore, there is a need for an automated MR scan prescription which allows for faster and more reporducible scans of the same region at different points in time.

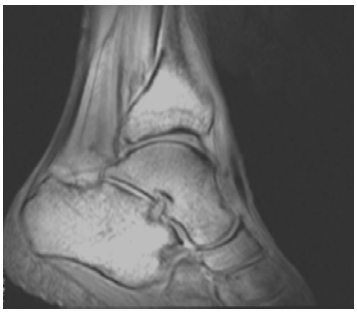

Figure 7.1: Typical localizer scan that initiates a MR examination of the distal

Longitudinal MR studies conducted to assess changes in bone quality in the tibia impose strict requirements on the reproducibility of data acquired(95,120) and the same region must be consistently analyzed between baseline and follow-up image acquisition. Due to the imprecise manual prescription currently performed by technologists, additional registration is needed post acquisition by manually matching slices.

Techniques to improve image registration precision by prospective registration, adjusting scanning parameters prior to image acquisition, have been reported recently in literature(138,139). A prospective registration technique for proton magnetic resonance spectroscopy of brain longitudinal examinations to track disease progression(123) has been developed. This technique utilizes a mutual information registration algorithm(89) to register images in a baseline and follow-up exam. The output of the registration algorithm, three translations and three Euler angles, is used to redefine the region to be imaged and thus to acquire a follow-up oblique imaging volume identical to the baseline volume. This pre-registration has provided improved region overlaps as well as generally decreased short-term measurement variability and improved workflow. Much work has been done to optimize and validate prospective registration in MR brain images(140-142), including methods to prospectively register brain images to an atlas(143) and to register brain spectroscopy images.(123,139) However, no such techniques have been applied to musculoskeletal imaging. All methods to register musculoskeletal images, such as the radius and tibia, for bone structure analysis have been performed post acquisition.(95,144)

When imaging trabecular bone in osteoporosis, the regional variations in structure of bone are inherent and follow-up images registered to the baseline images would have

profound impact on the quantitative evaluation of trabecular bone architecture. A study performed by Gomberg et al.(120) investigating the error sources in MRI-based trabecular bone structural parameters found the two main sources of variation to be patient motion and failure to match the ROI. They found that even if the ROI is offset by one slice, App. BV/TV can vary by a median error of 1%. An implementation of prospective registration to musculoskeletal MRI longitudinal studies would be of significant importance for characterizing trabecular bone. Prospective registration would reduce the need for an additional manual post-processing step that requires substantial expertise. It would therefore reduce the post processing time and subjectivity while maintaining the precision of trabecular bone measurements such as apparent bone volume fraction (App.BV/TV), apparent trabecular separation (App.Tb.Sp), apparent trabecular thickness (App.Tb.Th) and apparent trabecular number (App.Tb.N).

In this work, a software algorithm for the automatic prescription of a follow-up scan based on a baseline scan of the distal tibia is presented. The method is an extension of existing algorithms for post acquisition image registration and orientation. Rather than reorienting or matching slices after data acquisition to match scanned regions for analysis, the method presented here automatically provides a guide to the scanner to acquire a precise follow-up scan.

7.2 Methods

7.2.1 Registration Approach

We used an extension of the technique as presented by Hancu et al.(123) by implementing a mutual information measure to rigidly register baseline and follow-up low resolution images prior to acquiring high resolution scans (figure 7.2). The

transformation involves a rotation matrix, characterized by three Euler angles, and a translation vector composed of three translation parameters. The rotation matrix and the translation vector define the movement of a point from the follow-up to the baseline image. A conjugate gradient descent method(145) was implemented to search for the six parameters that define the rotation matrix and translation vector which optimize the mutual information measure. The transformation is then input into the scanner and used to acquire subsequent high resolution scans of the distal tibia.

7.2.2 MR Imaging

The right distal tibia of five healthy volunteers (average age of 26$\pm$3 years old) were scanned with their informed consent in accordance with the regulations of the Committee of Human Research at the University of California, San Francisco. All scans for each subject were performed on the same day. Subjects were removed from the scanner and repositioned between baseline and follow-up scans. To ensure a consistent clinical position between scans, a leg holder and pads were used in scanning which helped to limit rotation to small angles ($<10^{o}$). The longitudinal landmark line was aligned with the subject's lower leg and the transverse landmark line was aligned at the medial malleolus of the tibia.

All MR images were acquired axially on a 3-T Signa Scanner (GE Healthcare, Milwaukee, WI, USA) with a modified multi-acquisition SSFP sequence (Steady State Free Procession) applying a maximum intensity projection of two images (MI-SSFP).(146) A Nova Medical (Wilmington, MA, USA) four-coil surface phased array receiver coil was used. The scanning procedure is depicted in figure 7.2. After a three-plane localizer, two baseline scans were obtained. The first baseline scan was a low

spatial resolution scan in the axial plane with a 256x256 matrix, 8cm FOV, 0.5mm slice thickness, 64 slices, 60º flip angle, 17/6.5 ms TR/TE, and a scan time of approximately 4 minutes. The second baseline scan, intended for quantitative analysis and comparison, was a high spatial resolution with a 512x384 matrix, 8 cm FOV, 0.5 mm slice thickness, 64 slices, 60º flip angle, 17/6.5 ms TR/TE, and approximately 16 minutes of scan time (figure 7.3).

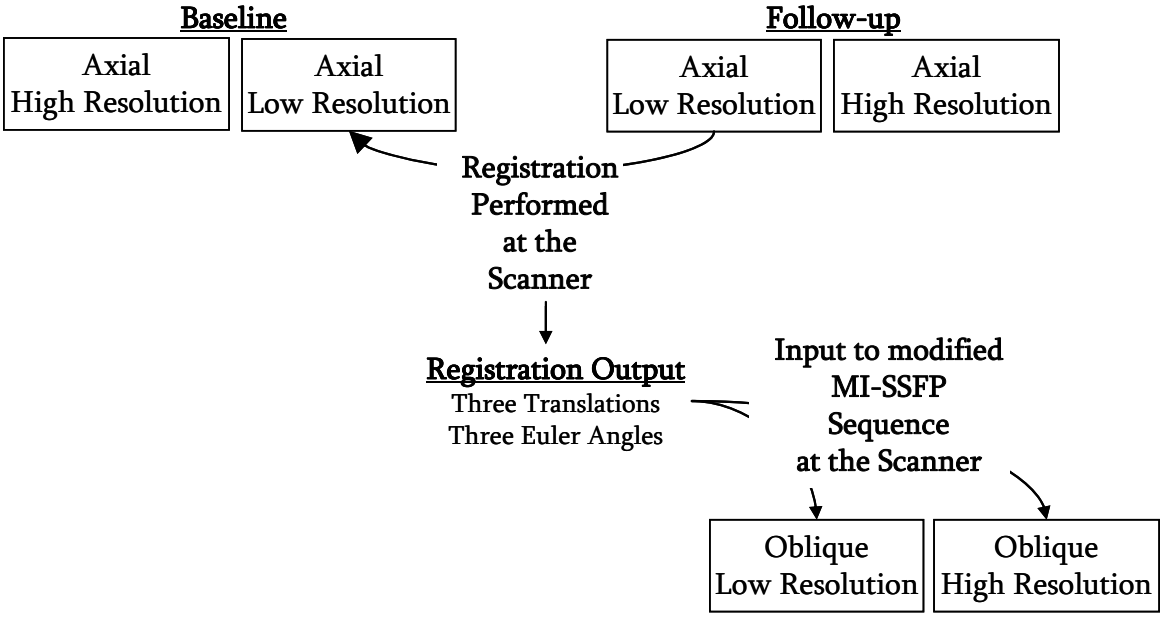

Figure 7.2: Diagram depicting the scanning procedure implemented in this study. The high resolution baseline and follow-up scans were used for trabecular bone analysis.

The volunteers were then removed from the scanner and repositioned for the follow up scans. After a three plane localizer, four follow-up scans were obtained. The first two follow-up scans used the same protocols as the first two baseline scans, one low spatial resolution follow-up scan for registration (~4 minute scan time) and a high spatial resolution scan for quantitative

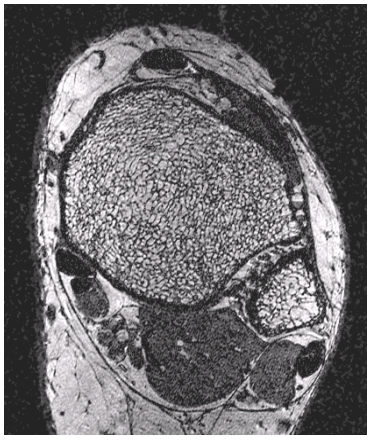

Figure7.3: Representative high spatial resolution (0.156 x 0.156 x 0.5mm^3) image of the distal tibia using a modified MI-SSFP sequence.

trabecular bone structure analysis and comparison (~16 minute scan time). The low resolution axial baseline and follow-up scans were then registered using the mutual information based rigid registration scheme described previously. The registration was performed while the patient remained in the scanner and took less than one minute, including the time to upload the baseline and follow-up volumes.

The final two follow-up scans required a modification of the MI-SSFP sequence to allow for the input of the six registration parameters (three translations and three rotations) output by the mutual information registration algorithm. Oblique scans were acquired with the same parameters as the first two follow-up scans except for input parameters from the registration. The prescription of these oblique scans had the same tibia coverage and slice orientation as the baseline axial images.

7.2.3 Modification of MI-SSFP Sequence

In order to allow the MI-SSFP sequence to accept rotations set manually by a user, a modification is required. Three new control variables (CVs) representation rotation in the x-axis, “myalpha”, the y-axis, “mybeta”, and the z-axis, “mygamma”, were created. Additionally a control variable named “read_inputs” acting as a flag to read in the rotations from a text file was created. Additional code was added to rotate the current scan prescription by the angles specified by myalpha, mybeta, and mygamma. Within the pulse sequence, rotation matrices for positive counterclockwise angles are about the positive coordinate axis for a right handed coordinate system. When the pulse sequence is downloaded with the “read_inputs” flag set to “1”, the pulse sequence reads in the three Euler angles from a text file named “Reg_prescription.dat” located in /usr/g/mrsc/register/ and sets the values of myalpha, mybeta, and mygamma respectively.

Alternatively, myalpha, mybeta, and mygamma can be set manually using "display CVs" and keeping "read_inputs" set to "0". The rotation matrix for the acquisition is then additionally rotated by myalpha, mygamma, and my beta.

7.2.4 Registration Algorithm Validation

To validate the registration algorithm, the output of the registration algorithm was compared to known values. One of the low-resolution images of one of the baseline scans was rotated and translated by a known amount selected with a random number generator. The rotation was limited to $\pm$ 8^{o} and the translation was limited to $\pm$ 10 mm. The baseline volume and the transformed volume were then registered and the registration error was computed as the difference between the known translation and the output of the registration algorithm. This procedure was repeated 50 times.

7.2.5 Registration Performance Evaluation

Visual inspection of 3D surface renderings and subtraction images aided in evaluating the success of the prospective registration with tibial images. Using an in-house developed software based on MATLAB (The MathWorks, Inc., Natick, MA), the inner cortical shell of the tibiae were segmented semi-automatically with a Bezier-spline and edge detection based method on a slice by slice basis. Segmented contours were then stacked to create a 3D surface. This was performed on the baseline and follow-up low spatial resolution images which were then visualized together in a 3D surface rendering. Subtraction images were created by subtracting the low spatial resolution follow-up volumes from the low spatial resolution baseline volumes. Subtraction images were

created for both follow-up image with the prospective registration and the follow-up image without registration. To quantify the improvement in image alignment seen in the subtraction images, the sum of the squares was calculated for each slice in the volume and then averaged across the volume.

7.2.6 Trabecular Bone Analysis

Tibial trabecular bone structure analysis was performed using software developed at our institution using IDL (Interactive Data language, Research Systems, Inc., Boulder, CO). Due to the use of surface coils, a correction for the spatial variation in the coil detection sensitivity was required for accurate image analysis. The images were coil-corrected with a low-pass-filter based coil sensitivity correction.(95) A volumetric region of interest (ROI) was manually defined using a graphics cursor. Moving proximally from the slice where the growth plate ends (endplate), the volumetric ROI consisted of twenty axial slices of the volume and included only trabecular bone and bone marrow. Each volumetric ROI requires between 10 and 20 minutes (30-60 seconds per slice) to accurately define. The ROI for the high resolution baseline image and follow-up image without registration were then registered manually by visually matching corresponding slices. The same ROI was used on the follow-up with prospective registration as for the baseline image and did not require the additional ROI definition and manual ROI registration. The resulting ROI was divided into two ten-slice thick regions due to inherent changes in trabecular bone structure with distance from the end plate. After the ROI had been defined and aligned, an image intensity histogram based thresholding technique was used to binarize the ROI into trabecular bone and marrow phases.(95)

Previously described methods(129) were then used to compute the apparent trabecular structural parameters: App.BV/TV, App.Tb.Sp., App.Tb.Th., and App.Tb.N. To determine the effects of using the prospective registration on trabecular parameters, the data was analyzed using a repeated-measures analysis of variance procedure.(147) This statistical procedure was chosen to help distinguish between the variability between the experimental subjects, the variability due to different post-processing methods, and the variability of the measurements within the same subject. The reproducibility of the technique was verified by calculating the short term coefficient of variation.(130)

7.3 Results

Table 7.1 presents the results of the registration validation by showing the registration errors (mean $\pm$ standard deviation) as determined by subtracting known transformations from registration outputs. The average error in rotations was ~0.2^{o} and in translations was ~1.1 mm which are within reasonable accuracy for tibia registration.

Table 7.1: Registration errors (mean + standard deviation) were determined by subtracting the registration output from the known transformation. The errors are shown in translations (Δx, Δy, and Δz) and rotations (θx, θy, and θz) as well as the average displacement $\Delta S3D=(\Delta x+\Delta y+\Delta z)/3$ and average rotation angle $\Delta\theta=(\theta x+\theta y+\theta z)/3$.

	Δx(mm)	Δy(mm)	Δz(mm)	ΔS_{3D}(mm)	θx(°)	Θy(°)	θz(°)	$\Delta\theta$(°)
Registration Error	1.0$\pm$1.1	1.0$\pm$0.8	0.8$\pm$0.7	1.1$\pm$0.6	0.3$\pm$0.2	0.2$\pm$0.2	0.2$\pm$0.2	0.2$\pm$0.1

By image subtraction and 3D surface rendering of the segmented tibiae, the improvement in image alignment can be assessed. Figure 7.4 shows representative results of the prospective registration. The improvement from the registration can be seen by looking at the subtraction images (figure 7.4c and 7.4f) and corresponding tibia segmentations (figure 7.4d and 7.4g). Displayed next to the subtraction images are the

corresponding low resolution follow-up images without registration (figure 7.4b) and with prospective registration (figure 7.4e). The baseline low resolution scan is also shown for comparison (figure 7.4a). It can be seen in the results that the second follow up scan is more closely oriented with the baseline scans. For example, in figure 7.4c the edges of the cortical bone are misaligned with higher intensity in the subtraction image, and clear separation of the red and green tibial renderings in figure 7.4d is visible. In figure 7.4f, the high intensity differences within the tibial edge are reduced, and there is considerably more overlap in the red and green tibial renderings in figure 7.4g.

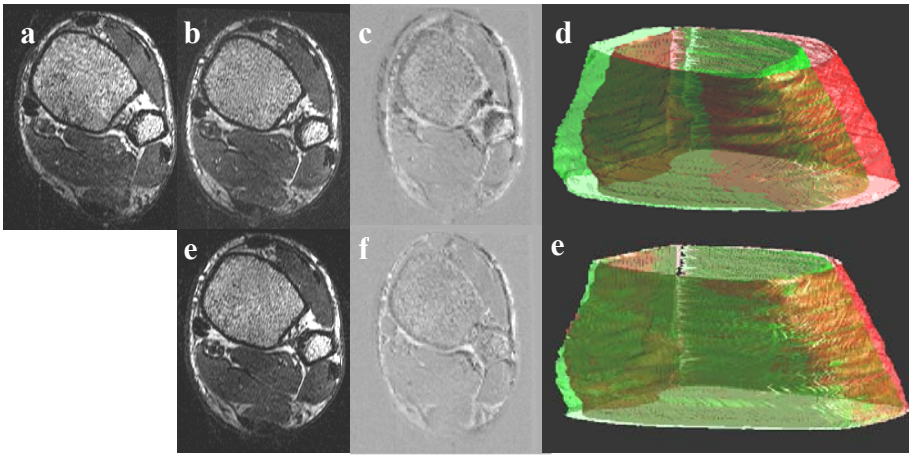

Figure 7.4: Visual comparison of prospective registration versus follow-up without registration for low spatial resolution images (0.313 x 0.313 x 0.5mm3) of the tibia. (a) Axial slice of baseline image (b) Axial slice of follow-up image without registration (c) Subtraction of a and b (d) Rendering of non-registered tibiae (green=low resolution baseline, red=low resolution follow-up) (e) Axial slice of follow-up image with prospective registration (f) Subtraction of a and e (g) Rendering of prospectively registered tibiae (green=low resolution baseline, red=low resolution follow-up)

Figure 7.5: The sum of the squares of the subtraction images created from low resolution images was calculated for each slice and then averaged across all slices. The sum of the squares was lower for the prospective registration subtraction images for each of the five tibiae.

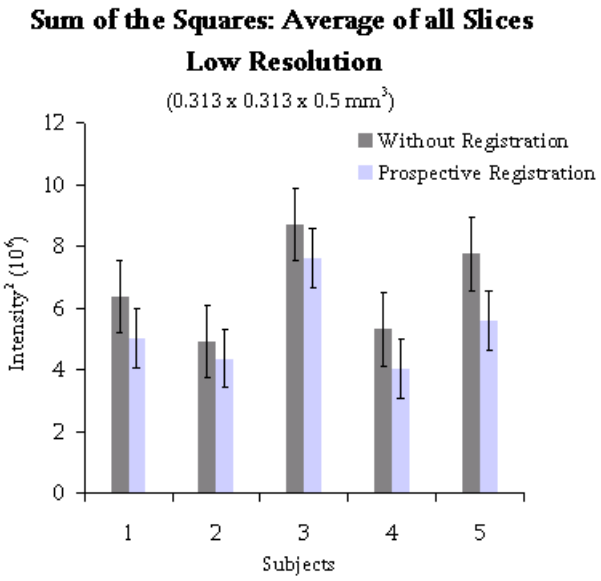

To quantify the dispersion seen in the subtraction images, the sum of the squares was calculated for each slice. The graph in figure 7.5 shows the average of the sum of the squares across all slices for the volume for each of the five subjects. Sum of the squares was lower for the follow up images with prospective registration by an average of 19.37% $\pm$ 0.07.

Our study did not observe differences between the trabecular bone structure parameters calculated from the post-scan manual registration and the prospective registration images. Figure 7.6 shows the trabecular bone parameters calculated for one of the tibiae. There is very little variation in the parameters between images. The results of a repeated-measures analysis of variance indicate there is no significant difference between the trabecular bone parameters calculated from the prospective registration images and those calculated from the post-scan manual registration ($p>0.05$).

Additionally, our study also found little difference in the coefficient of variation when evaluating the post-scan registration and the prospective registration for the four parameters in the two different bone regions. All values were within a 2-4.5% (figure 7.7) range, which are within values previously reported.(95)

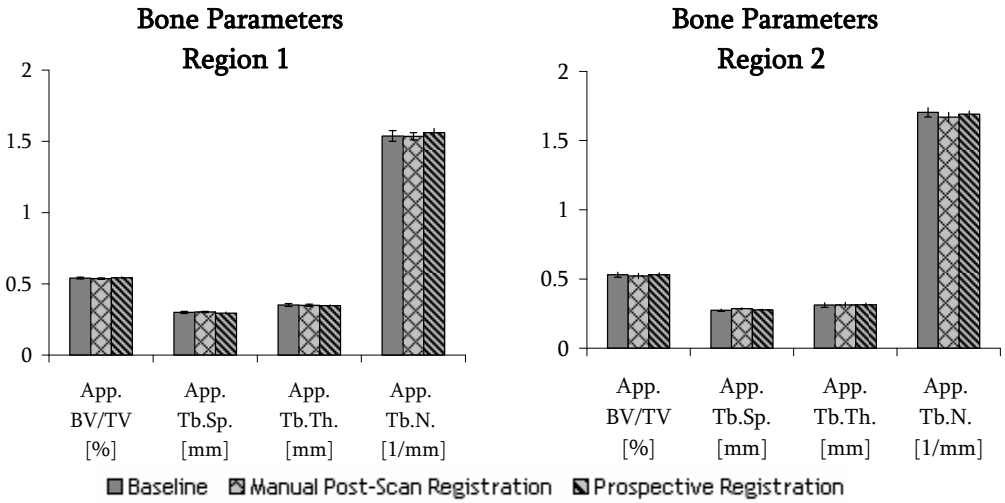

Figure 7.6: The raw data for the trabecular bone parameters for one of the tibiae in both regions is shown. Very little variation in the parameters was found between images which demonstrates that the trabecular bone parameters found with the prospective registration are just as accurate as those found using the manual post-scan registration technique.

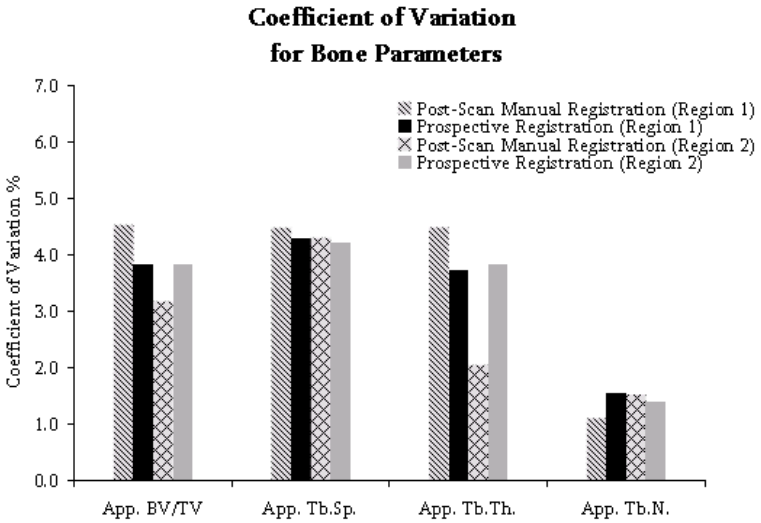

Figure 7.7: The coefficient of variation values were within a 2-4.5% range for all four trabecular bone parameters in the two bone regions.

7.4 Discussion and Conclusion

In this work we have demonstrated the feasibility of using a mutual information based method to prospectively register longitudinal MR images of tibia scans. We have developed a unique MI-SSFP sequence which allows for the input of the registration results to scan oblique registered high spatial resolution tibia images.

The coefficient of variation of the trabecular bone structure parameters is within the same range for both registration types and the repeated-measures analysis of variance indicates that there is no significant difference in trabecular bone parameters between baseline and follow-up images for both registration types. These findings demonstrate that the trabecular bone structure parameters found with the prospective registration are just as accurate as those found using the established post-scan manual registration technique.(95)

The use of automatic prospective registration ensures that the ROI is placed on the same slice for both the baseline and follow-up. Automatic prospective registration also has benefits by eliminating the need for subjectively finding the longitudinal reference location (endplate location) for all follow-up scans. In addition, the use of prospective registration at clinical sites will ensure that the same region is scanned in the baseline and follow-up. Often there is a discrepancy in the region scanned and the images cannot be utilized for quantitative comparison.

Automatic prospective registration allows for a time savings and an easy analysis of multiple ROIs, as the regions defined on the baseline scans can also be applied directly to the registered follow-up images. Automatic prospective registration adds four minutes to the baseline scan time and five minutes (four minutes of scan time and one minute for the registration) to the follow-up scan time. However it eliminates the need for an

additional ROI to be manually generated for the follow-up images, which allows for a 10 to 20 minute savings in post-processing time. For longitudinal studies, where hundreds of patients are being scanned and analyzed, the time savings in post-processing could be substantial.

The prospective registration algorithm implemented in this study was the same algorithm utilized by Hancu et al.(123) It is optimized for magnetic resonance spectroscopy studies with a mutual information metric, a rigid body transformation, and a conjugate gradient descent optimizer. Although the results from implementing this prospective registration technique are just as accurate as the results from the current post-scan manual registration technique, the algorithm may produce better results if optimized for musculoskeletal imaging. Since the registration is intra-modality, an intensity-based metric such as a normalized cross-correlation metric(148) or a mean squares metric(149) may be more appropriate. Additionally, musculoskeletal images contain joints surrounded by soft tissue that deform depending on the subject position. This deformable soft tissue makes rigid registration more challenging for musculoskeletal images compared to brain images. The registration can be improved by cropping the image so that the entropy is only calculated in a region with minimal soft tissue. This would minimize the effects of the non-rigid movement of the soft tissue on the registration of bone. However, an automatic method for removing soft tissue for musculoskeletal images is not straightforward due to lack of defined edges and similar intensities for both hard and soft tissues.

Automatic retrospective registration, registration after the images have been acquired, may be an alternative to prospective registration. However, prospective

registration requires no interpolation of the data which is required in automatic retrospective registration. All interpolation methods introduce artifacts to images to some degree and images with sharp-edge details, such as high-resolution trabecular bone images, are much more affected.(53) Prospective registration also ensures that the correct region is being acquired at scan time. Retrospective registration will fail if there is a large difference in the regions scanned and therefore little overlap between the baseline and follow-up images.

Prospective registration may have a bigger impact on hip images since the reproducible positioning of the subjects is not as easy as when imaging the tibia. Carpenter et al.(150) performed a study investigating the reproducibility of bone structure parameters in the proximal femur. They suggested that the high coefficients of variation, ranging from 6.5% to 13.5% may be partially due to patient repositioning. Additionally, the images of the proximal femur were acquired with a slice thickness of 1mm, double the slice thickness in this study, which may contribute to additional partial volume effects. Prospective registration may be able to ensure consistent partial volume effects between time points by allowing the selection of the same slice. More experiments need to be conducted to investigate if prospective registration can minimize patient repositioning effects when imaging the proximal femur.

This study proves that it is possible to implement prospective registration to a musculoskeletal application. Prospective registration ensures that the same region is analyzed in both the baseline and follow-up images, saves post processing time, preserves the reproducibility of the trabecular bone parameters, and requires no interpolation. The

results suggest that it may be robust enough to be used in different musculoskeletal imaging applications including the hip.

Chapter 8

Automatic prospective registration extension to Sagittal and Coronal Imaging Planes

8.1 Introduction

The automatic prospective registration in MR imaging for an axial patient orientation presented in Chapter 7 is fairly straight forward because the direction of the axes in the image coordinate system and the scanner coordinate system coincide. However prospective registration for alternative patient positions, such as sagittal and coronal, requires an additional mapping step (see figure 8.1). The patient orientation for MR images of trabecular bone depend on the anatomical site being imaged. For example, while the distal tibia and distal radius typically require axial scans, trabecular bone imaging of the knee, the distal femur, and the hip, the proximal femur, requires a coronal scan. Additionally, due to patient comfort or a desire to image the trabecular bone in an alternative orientation, these standard orientations are subject to change. For example, sagittal imaging of the distal radius is required when the wrist is positioned horizontally in the scanner and sagittal imaging of the knee is frequently desired to minimize partial volume effects. Therefore, the ability to implement prospective registration in a variety of orientations is desired. In this chapter, the prospective registration methods for these alternative patient positions are outlined and described in detail.

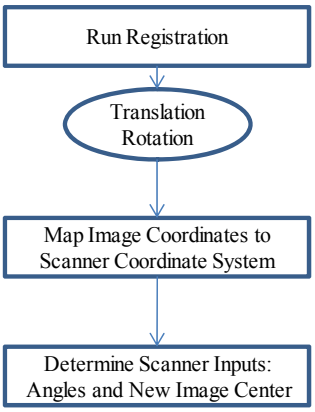

Figure 8.1: Flow chart of prospective registration method

While solutions have been proposed for the brain(123,151-153), very little published data exists on the implementation and feasibility of automatic scan prescription of the knee. The only method presented for the knee is based on active shape models(154,155). In this method, 3D deformable models of the femur, tibia, and patella are used to automatically detect these bones in a T1-weighted gradient echo sequence. Points on the surface of these bones constitute a set of landmarks which are used to determine point to point correspondences between an initial mean shape model and the position locally adapted shape model. These correspondences can then be used to determine the appropriate orientation of subsequent image acquisitions. This method requires a training set of similar images in which landmarks and desired orientation of the subsequent acquisitions have been selected by a trained technologist. Additionally the algorithm does not change the number of slices according to the size of the patient/knee which often limits the anatomical coverage in large knees. The accuracy of the method in longitudinal studies assessing the progression of disease such as Osteoarthritis in which large anatomical changes to the bone can occur, has not been established. Due to large anatomical variation due to biological differences or disease, a universal method which determines the automatic alignment of follow-up images in a longitudinal study may not be possible. Rather a method similar to that in Chapter 7 which prescribes the follow-up image based on the baseline image may be more robust.

8.2 Methods

8.2.1 Image, Patient, and Scanner Coordinate Systems

In order to accurately translate the rigid transformation output of the registration algorithm, three rotations and three translations, it is important to precisely describe how the image coordinates match up to the scanner coordinates. There exist three different coordinate systems, the image coordinate system, the patient (anatomical) coordinate system, and the scanner coordinate system.

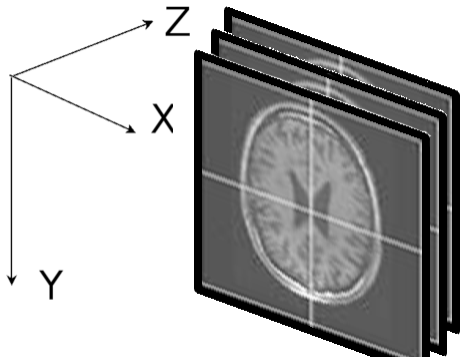

Figure 8.2: Image coordinate system. The direction of cosines in the dicom header indicates what x,y, and z correspond to in patient (anatomical) coordinates

Image Coordinate System

The image coordinate system refers to the order of the pixels (figure 8.2) within the image. Side-to-side is the x direction, up/down is the y direction and the slice order is the z direction. The upper left corner of the first slice represents the origin of the image and has the coordinates (0,0,0) in the image coordinate system.

Patient Coordinate System

The patient coordinate system refers to the standard anatomical terms of location (Anterior/Posterior, Superior/Inferior, and Right/Left). All naming is based on positions relative to the body in a standing (standard anatomical) position with arms at the side and palms facing forwards (thumbs out). Posterior in medical anatomy refers to the "back" of the subject and Anterior refers to the “front” of the subject. The head end is referred to as the superior end, while the feet are referred to as the inferior end. The left side and right side of a subject are the outermost points between the two "sides" of the subject.

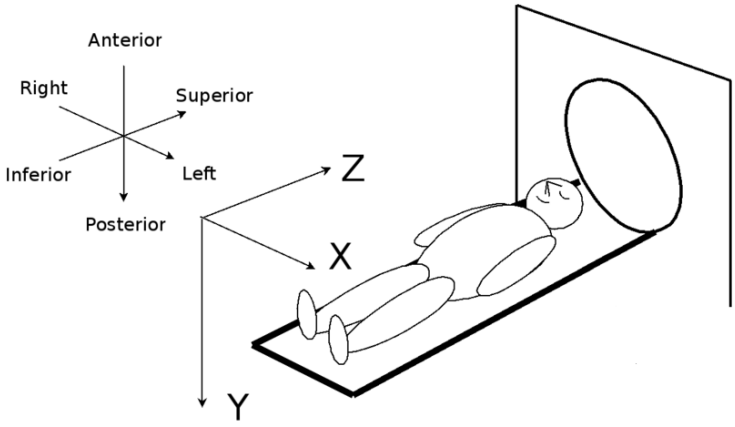

Figure 8.3: Drawing depicting directions of x, y, z in an axial MR image for a patient positioned supine head first. Positive x,y,z in an image corresponds to left, posterior, superior respectively in patient coordinates.

Scanner Coordinate System

The scanner coordinate system refers to the location of a point inside the scanner where x is positive toward the right side of the scanner, y is positive toward the top of the scanner, and z is positive towards the back of the scanner (figure 8.3). The scanner coordinate system is often referred to as RAS because it corresponds to a patient placed in the scanner in a supine head-first position. When a patient is placed in this position, the right hand of the patient corresponds to the positive x axis of the scanner, the anterior side of the patient corresponds to the positive y axis of the scanner, and the superior side of the patient corresponds to the positive z axis of the scanner.

8.2.2 Mapping Image Coordinates to Patient Coordinates

The direction of the x,y,z axes within the MR image is defined fully by the patient's orientation in the scanner. If a patient lies in a supine head first position, the direction of the axes in the image coordinate system and the scanner coordinate system will coincide. The direction cosines (the Image Orientation tag) in the image dicom header helps to map the image coordinate system to the patient coordinate system.

Mathematically, the direction cosines refers to the cosine of the angle between any two unit vectors (figure 8.4).

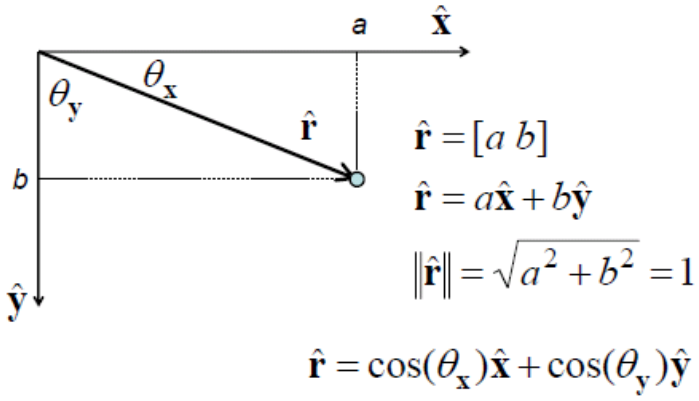

Figure 8.4: Direction Cosines: The components of a unit vector (**a** and **b**) are the cosines of the angles the vector makes with the basis directions.

The Image Orientation tag is an orientation matrix with 2 rows and 3 columns.

$$\text{orientation matrix} = \begin{bmatrix} a & b & c \\ d & e & f \\ g & h & i \end{bmatrix} \tag{8.1}$$

The first row [a b c] corresponds to the x axis in an image and the second row [d e f] corresponds to the y axis in the image. The first column of the matrix $\begin{bmatrix} a \\ d \\ g \end{bmatrix}$ corresponds to the R/L direction, the second column of the matrix $\begin{bmatrix} b \\ e \\ h \end{bmatrix}$ corresponds to the A/P direction, and the third column of the matrix $\begin{bmatrix} c \\ f \\ i \end{bmatrix}$ corresponds to the S/I direction. To determine which anatomical direction corresponds to the x axis in the image, we will look at the first row of the orientation matrix. If the image is an axial image (head first, supine) then

the x axis in the image will correspond to the R/L anatomical direction and the first row of the orientation matrix will be [1 0 0]. Similarly the y axis will correspond to the A/P anatomical direction and the second row of the matrix will be [0 1 0]. The z axis will correspond to the S/I direction and the third row of the matris will be [0 0 1]. The Image Orientation coordinates are often referred to as LPS because increasing to the left, poserior, and superior are all positive. Note that the directions are not the same as the scanner RAS coordinate system.

For head first supine the orientation matrices will be:

$$\text{Axial orientation matrix} = \begin{bmatrix} 1 & 0 & 0 \\ 0 & 1 & 0 \\ 0 & 0 & 1 \end{bmatrix} \qquad \text{Sagital orientation matrix} = \begin{bmatrix} 0 & 1 & 0 \\ 0 & 0 & 1 \\ 1 & 0 & 0 \end{bmatrix}$$

$$\text{Coronal orientation matrix} = \begin{bmatrix} 0 & 0 & 1 \\ 1 & 0 & 0 \\ 0 & 1 & 0 \end{bmatrix}$$

Each row can be thought of as a unit vector defining the anatomical orientation of the axis. When the scan is oblique, the values in the vector (ex: [-0.174323 0 -0.984688]) correspond to the unit vector which is -0.174323 in the R/L direction, 0 in the A/P direction, and -0.984688 in the S/I direction.

8.2.3 Mapping Image Coordinates to Scanner Coordinates

Image registration is performed in the image coordinate system where the output transformation results in a rotation and translation in x,y,z. To implement the prospective registration, the transformation needs to be converted into scanner coordinates. However, the scanner coordinate system remains constant (RAS) whenever the patient position (ie supine/prone or head-first/feet first), the scan plane changes (axial, sagittal, or coronal),

the gradient direction, or slice order switches, but the mapping of image coordinates to patient coordinates changes. Therefore it is necessary to use the image orientation matrix to determine how the patient is oriented in the scanner, and how the transform maps to the scanner coordinates.

Therefore in order to put the translation (T) and rotation (R) from image coordinates (the output of the registration algorithm) to scanner coordinates (T' and R') which are needed as inputs to the scanner we need to apply a matrix $M_{scanner}$:

$$\begin{pmatrix} T_x' \\ T_y' \\ T_z' \end{pmatrix} = \boldsymbol{M}_{scanner} \begin{pmatrix} T_x \\ T_y \\ T_z \end{pmatrix} \qquad \boldsymbol{R}(\alpha,\beta,\gamma)' = \boldsymbol{M}_{scanner}\boldsymbol{R}(\alpha,\beta,\gamma) \tag{8.2}$$

Where:

$\begin{pmatrix} T_x \\ T_y \\ T_z \end{pmatrix}$ denotes the translation (T) in image coordinates and $\begin{pmatrix} T_x' \\ T_y' \\ T_z' \end{pmatrix}$ denotes the translation (T') in scanner coordinates;

$\boldsymbol{R}(\alpha,\beta,\gamma)$ denotes the rotation (R) in image coordinates and $\boldsymbol{R}(\alpha,\beta,\gamma)$ 'denotes the rotation (R') in scanner coordinates;

$\boldsymbol{M}_{scanner}$ denotes the mapping from image coordinates to scanner coordinates and depends on the patient position and scan plane.

For supine, head first, axial positioning the mapping is very straight forward because the scanner coordinates coincide with the image coordinate system (X relates to R/L, Y relates to A/P, and Z relates to S/I). However, because the scanner is in RAS and the image coordinates is in LPS, the signs in X(R/L) and Y(A/P) need to be flipped.

$M_{scanner}$ for supine, head first, **axial** $= \begin{bmatrix} -1 & 0 & 0 \\ 0 & -1 & 0 \\ 0 & 0 & 1 \end{bmatrix}$ (8.3)

$M_{scanner}$ for other orientations is not as straightforward. For sagittal orientation X in image coordinates relates to A/P, Y relates to S/I, and Z relates to R/L. Again, because the scanner is in RAS and the image coordinates is in LPS, the signs in X and Y need to be flipped.

$$M_{scanner} \text{ for supine, head first, } \textbf{saggital} = \begin{bmatrix} 0 & 0 & 1 \\ -1 & 0 & 0 \\ 0 & -1 & 0 \end{bmatrix} \tag{8.4}$$

For coronal orientation X in image coordinates relates to S/I, Y relates to R/L, and Z relates to A/P. Again, because the scanner is in RAS and the image coordinates is in LPS, the signs in X and Y need to be flipped.

$$M_{scanner} \text{ for supine, head first, } \textbf{coronal} = \begin{bmatrix} -1 & 0 & 0 \\ 0 & 0 & 1 \\ 0 & -1 & 0 \end{bmatrix} \tag{8.5}$$

8.2.4 Formatting Scanner Inputs

Now that the transform has been mapped to scanner coordinates, it needs to be input into the scanner. To adjust the translation for a scanned region, an operator adjusts the center location of the scan. To adjust the rotation for a scanned region, an operator adjusts the angles for the gradients. Therefore the input to the scanner is composed of three angles and a new image center.

In the scanner coordinate system, the transform that results from the registration algorithm can be given by:

$$P' = R'(P - C) + (C + T') \tag{8.6}$$

where C is the center of rotation, P is the point to be transformed, P' is the transformed point, T' is the translation, and R' is the rotation matrix. For the scanner, R' is constructed when the operator inputs the three angles, C corresponds to the image center. This equation can be re-written as

$$P' = R'P + [C + T' - R'C] \quad (8.7)$$

and we call Offset the expression

$$\text{Offset} = [C + T' - R'C]. \quad (8.8)$$

The transformation is now

$$P' = R'P + \text{Offset} \quad (8.9)$$

and the relationship between Translation and offset is

$$\text{Offset} = [I - R'] C + T' \quad (8.10)$$

To determine the new image center, P is set to the current image center and C is set to the scanner's center of rotation, the isocenter where C = (0,0,0). The equation for the new image center can the be re-written as

$$P' = [I - R'] P + T' \quad (8.11)$$

and the resulting P' can be used to input the new image center into the scanner.

8.2.5 MR Imaging

The right knee of two healthy volunteers was scanned with their informed consent in accordance with the regulations of the Committee of Human Research at the University of California, San Francisco. The volunteers were removed from the scanner and repositioned between baseline and follow-up scans. To ensure a consistent clinical position between scans, pads were used in scanning which helped to limit rotation to small angles ($<10^{o}$).

MR images were acquired sagittally and coronally for the first and second volunteer respectively. These images were acquired on a 3-T Signa Scanner (GE Healthcare, Milwaukee, WI, USA) with a transmit/receive quadrature knee coil (Clinical MR Solutions, Brookfield, WI). After a three-plane localizer, two baseline scans were obtained. The first baseline scan was a low spatial resolution scan with a 3D water excitation low-resolution spoiled gradient-echo (SPGR) pulse sequence (a 160x160 matrix, 10cm FOV, 1mm slice thickness, 52 slices, 18º flip angle, 10/1.52 ms TR/TE, and a scan time of approximately 1 minute 30 sec). The second baseline scan, intended for quantitative analysis and comparison, was a 3D water excitation high-resolution spoiled gradient-echo (SPGR) pulse sequence with asset parallel imaging (512x512 matrix, 10cm FOV, 1mm slice thickness, 52 slices, 18º flip angle, 20/6.28 ms TR/TE, and a scan time of approximately 6 minutes) which is commonly used in knee morphologic imaging. The volunteer was then removed from the scanner and repositioned for the follow-up scans. After a three plan localizer, an image was acquired with a low spatial resolution scan with the same pulse sequence and parameters as the low spatial resolution baseline scan. The low resolution baseline and follow-up scans were then registered using the mutual information based rigid registration scheme described previously. The registration was performed while the patient remained in the scanner.

The follow-up scan required a modification to the high resolution SPGR sequence to allow for the input of rotation angles and new image center which is determined from the output (translation and rotation) of the mutual information registration algorithm. Oblique scans were acquired with the same parameters as the high resolution baseline

scans except for rotation and new image center input parameters. The prescription of the oblique scan had the same knee coverage and slice orientation as the baseline image.

8.3 Results

The registration algorithm was able to successfully register both the low spatial resolution sagittal and coronal images and provide accurate inputs to the MR scanner. The prospective registration and took less than two minutes, including the time to upload the baseline and follow-up volumes and inputting the new rotations and new center in the MR scanner.

For the sagittal image, the registration resulted in a translation of 11.2mm, 5.66mm,-1.86mm and in a rotation of 0.76^{o}, -0.84^{o}, -0.24^{o} in x, y, and z respectively. This resulted in a new image center of R76.5, A28.4, and S22.5. For the coronal image, the registration resulted in a translation of -1.76mm, 0.42mm, and -3.46mm and in a rotation of 9.24^{o}, -2.14^{o}, 6.56^{o} in x, y, and z respectively. This resulted in a new image center of L54.7, A50.1, and S23.7.

Difference images were created by subtraction follow-up from baseline images. Visual inspection of the difference images between the non-registered low resolution images and the registered high resolution images clearly demonstrates an improvement in image alignment(figure 8.5 and figure 8.6).

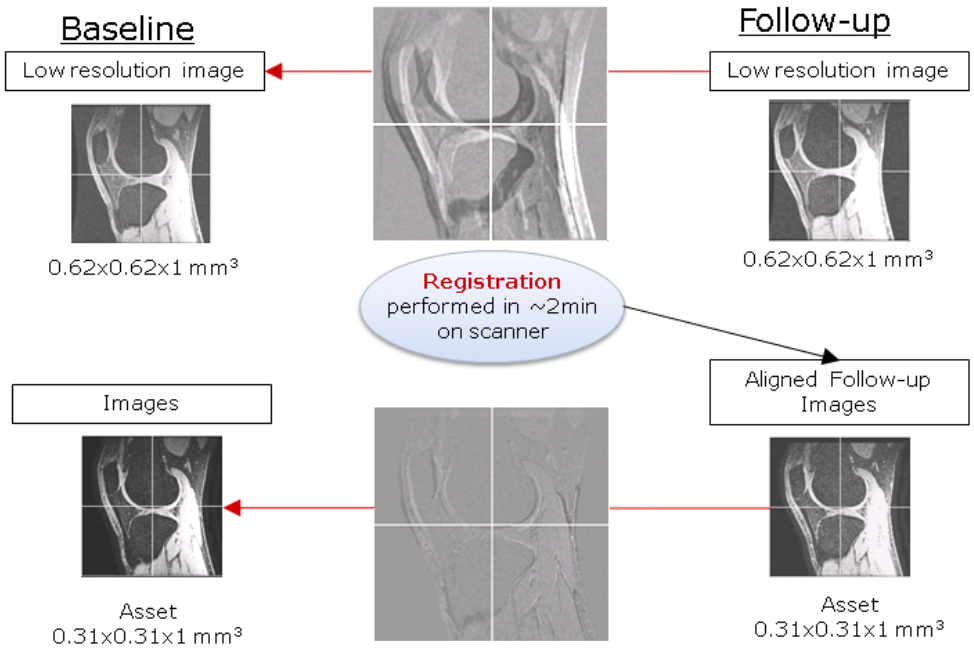

Figure 8.5: Visual results from sagittal prospective registration. A follow-up low resolution sagittal image was registered to a baseline low resolution sagittal images and output of the registration was used to acquire a new oblique follow-up image. The center images are difference images between the non-registered low resolution images (top image) and the registered high resolution images (bottom image).

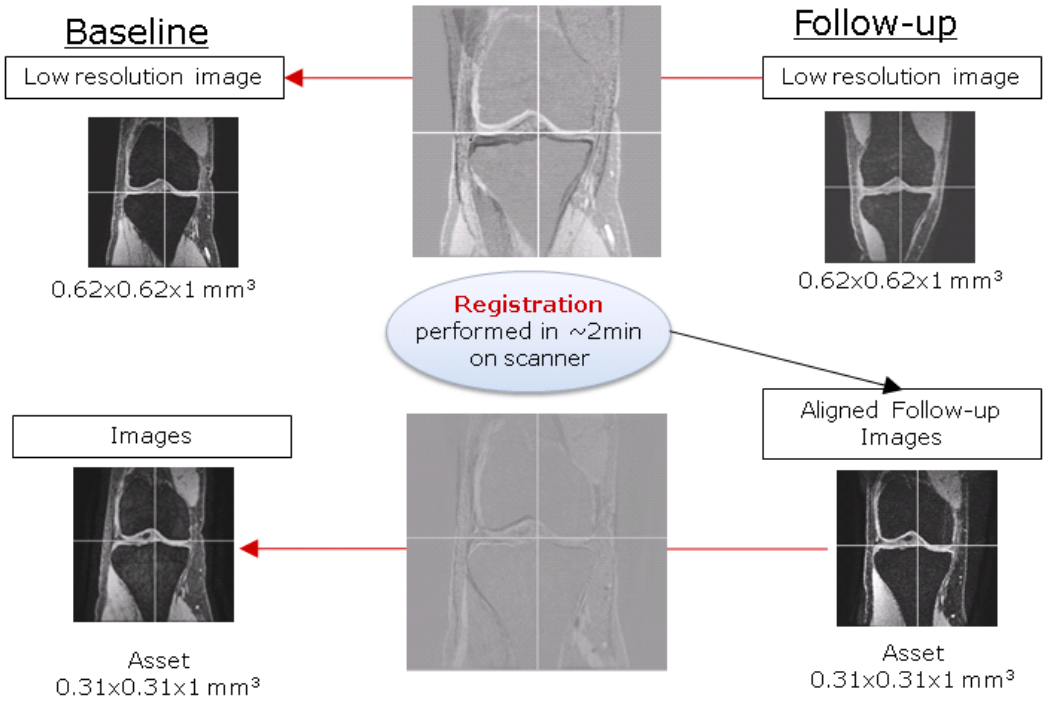

Figure 8.6: Visual results from coronal prospective registration displayed in the same fashion as the figure above.. The center images are difference images between the non-registered low resolution images (top image) and the registered high resolution images (bottom image).

In both figure 8.5 and 8.6 the difference image between the low resolution baseline and follow-up scans shows a clear separation in both the femur and tibia. The higher intensities in the non-registered difference images represent regions where the bones do not over lap. The difference images with registration do not have the high intensity regions because the bones over lap.

8.4 Discussion and Conclusion

Traditionally the orientation and position of MR images of the knee in longitudinal studies are prescribed manually by a trained technologist. The quality and consistency of the positioning and orientation of follow-up images rely of the technologist's skill and experience. This process is often time-consuming and inconsistent. Therefore automatic prescription of the orientation and position of follow-up knee MR images is highly desired. This chapter extended the prospective registration method presented in chapter 6 to sagittal and coronal orientations. The technical details in the conversion of registration outputs to scanner inputs are outlined as well as a demonstration of the feasibility of the method in knee scans.

The prospective registration method was demonstrated in both a sagittal and coronal acquisition of the knee. Visual inspection of difference images demonstrated the improved alignment in the registered follow-up images and that the same regions were scanned in both the baseline and follow-up images.

The method presented here can be added to the beginning of any scanning protocol. Once the registration has been performed and the registered follow-up image acquired, it can then be used to prescribe any pulse sequence. For example, a high

resolution MI-SSFP acquisition which is required for trabecular bone analysis can then be acquired using the registered image to prescribe the desired scan region.

Chapter 9

Conclusions

9.1 Summary

This thesis developed robust methods for the registration of musculoskeletal images to enhance the study and assessment of bone. The primary contributions of this thesis include:

- Direct comparison of tissue mineral density measurements between ex vivo μCT and SRμCT imaging methods using multi modality image registration
- Development of a method to leverage multi modality automatic registration between high-resolution trabecular bone MR images and HR-pQCT image to enhance the study of cortical porosity
- Implementation and optimization of single modality automatic retrospective registration of high-resolution trabecular bone MR images
- Evaluation of robustness, performance, and reproducibility of automatic retrospective registration of high-resolution trabecular bone MR images
- Application of automatic retrospective registration to real clinical longitudinal datasets demonstrating an improvement in the measurement accuracy of trabecular structure changes
- Development of prospective registration for trabecular bone imaging and extension to multiple imaging planes

This thesis demonstrates the impact of image registration in the analysis of musculoskeletal images of bone. Image registration has been shown to improve the accuracy, reproducibility, and precision of longitudinal and comparative bone studies. In studies comparing tissue mineral density (TMD) measurements from SRμCT and μCT imaging techniques, image registration allows for the direction comparison of values which provides additional information for the development of an accurate TMD correction. Image registration also allows for different image techniques such as MR and HR-pQCT to be combined, providing additional information about the nature of cortical porosity. In longitudinal MR studies assessing the efficacy of treatment or monitoring disease progression, image registration ensures the same region is analyzed across time points and improves the accuracy of results.

9.1.1 Registration of SRμCT and μCT trabecular bone images

Chapter 3 evaluates μCT TMD measurements by a comparison to synchrotron SR μCT. A inter-modal rigid registration method was developed and allowed for a direct spatial comparison of TMD distributions. The image registration methodology proposed in this study was able to successfully align SRμCT and μCT images. Results suggested that b-spline approximation as a final interpolator is best able to preserve grayscale values. Voxel overlap measures and visual inspection both demonstrated the successful alignment. With registration there was a 49% - 70% improvement in the percentage of voxel overlap. Gaussian smoothing on increasing scales was applied to the μCT images and its effects on TMD measurements compared to SRμCT values was evaluated. The correlation between SRμCT and μCT mean TMD values was highly improved with smoothing of the μCT images ($r = 0:85$; $p < 0.0002$) compared to without smoothing ($r =$

0:45; $p < 0.2$). This implies that noise removal can contribute to increased reliability of TMD estimates from μCT images.

9.1.2 In vivo evaluation of the presence of bone marrow in cortical porosity

Chapter 4 presents the first study examining cortical porosity in vivo in postmenopausal osteopenic women and to combine data from two different imaging modalities to further examine the nature of cortical porosity. The radius of 49 and the tibia of 51 postmenopausal osteopenic women (age 56+3.7) were scanned using both HR-pQCT and MR imaging. A normalized mutual information registration algorithm was used to obtain a three dimensional rigid transform which aligned the MR image to the HR-pQCT image. The aligned images allowed for the visualization of bone marrow in cortical pores. From the HR-pQCT image, the percent cortical porosity, the number of cortical pores, and the size of each cortical pore were determined. By overlaying the aligned MR and HR-pQCT images, the percent of cortical pores containing marrow, the number of cortical pores containing marrow, and the size of each cortical pore containing marrow was measured. The percent cortical porosity ranged from 2.1% to 9.2% in the tibia and 0.4% to 5.0% in the radius. The percent cortical pores containing marrow ranged from 1.6% to 21.0% in the tibia and 4.96% to 41.75% in the radius. While the amount of cortical porosity did not vary greatly between subjects, the type of cortical pore, containing marrow versus not containing marrow, varied highly between subjects. Additionally, the number of cortical pores containing marrow did not depend on the amount of porosity and there was no relationship between cortical pore size and the presence of bone marrow. The data suggest that cortical pore spaces contain components

of varying composition, and that there may be more than one mechanism for the development of cortical porosity.

9.1.3 Image registration of MR images for the analysis of trabecular bone parameters

Chapter 5 investigated feasibility of automatic image registration of MR high-spatial resolution proximal femur trabecular bone images as well as the effects of gray-level interpolation and volume of interest (VOI) misalignment on MR-derived trabecular bone structure parameters. For six subjects in a short-term study, a baseline scan and a follow-up scan of the proximal femur were acquired on the same day. For 10 subjects in a long-term study, a follow-up scan of the proximal femur was acquired one year after the baseline. An automatic image registration technique, based on mutual information, utilized a baseline and a follow-up scan to compute transform parameters that aligned the two images. In the short-term study, these parameters were subsequently used to transform the follow-up image with three different gray-level interpolators. Nearest-neighbor interpolation and b-spline approximation did not significantly alter bone parameters, while linear interpolation significantly modified bone parameters ($p<0.01$). Improvement in image alignment due to the automatic registration for the long term and short term study was determined by inspecting difference images and 3D renderings. This work demonstrates the first application of automatic registration, without prior segmentation, of high-spatial resolution trabecular bone MR images of the proximal femur. Additionally, inherent heterogeneity in trabecular bone structure and imprecise positioning of the VOI along the slice (anterior-posterior) direction resulted in significant changes in bone parameters ($p<0.01$). Results suggest that automatic mutual information registration using b-spline approximation or nearest-neighbor gray-level interpolation to

transform the final image ensures VOI alignment between baseline and follow-up images and does not compromise the integrity of MR-derived trabecular bone parameters. Chapter 6 extended the technique and methods developed in Chapter 5 to a longitudinal clinical study assessing the efficacy of drug treatment on trabecular bone of the proximal femur in postmenopausal osteopenic women. The coefficient of determination (R^2) between baseline and follow-up measurements for all trabecular bone parameters improved demonstrating the removal of error due to mis-aligned analysis regions. This work is the first time that image registration has been implemented in a longitudinal clinical study investigating changes in MR-derived trabecular bone structure.

9.1.4 Prospective registration of MR images of trabecular bone

Chapter 7 develops a method for automatic prospective algorithm for a MRI longitudinal study of trabecular bone of the tibia and compared it to a post-scan manual registration. Qualitatively, image alignment due to the prospective registration is shown in 2D subtraction images and 3D surface renderings. Quantitatively, the registration performance is demonstrated by calculating the sum of the squares of the subtraction images. Results show that the sum of the squares is lower for the follow up images with prospective registration by an average of 19.37% + 0.07 compared to follow up images with post-scan manual registration. Our study found no significant difference between the trabecular bone structure parameters calculated from the post-scan manual registration and the prospective registration images ($p>0.05$). All coefficient of variation values for all trabecular bone structure parameters were within a 2-4.5% range which are within values previously reported in the literature. Results suggest that this algorithm is robust enough to be used routinely in different musculoskeletal imaging applications.

Chapter 8 extended the prospective registration method presented in chapter 7 to sagittal and coronal orientations. The technical details in the conversion of registration outputs to scanner inputs are outlined as well as a demonstration of the feasibility of the method in knee scans. The prospective registration method was demonstrated in both a sagittal and coronal acquisition of the knee. Visual inspection of difference images demonstrated the improved alignment in the registered follow-up images and that the same regions were scanned in both the baseline and follow-up images.

9.2 Future Directions

9.2.2 Extension of registration techniques to additional musculoskeletal applications

Registration of high-resolution in vivo trabecular bone images of the tibia, radius, and proximal femur has been demonstrated in this thesis. However, registration may also be useful in additional musculoskeletal applications beyond the quantification of trabecular bone structure. MR image is frequently used to assess the progression of osteoarthritis, a disease which deteriorates the cartilage of the knee, hip and shoulder. Alignment of knee, hip, and shoulder images for the quantitative analysis of cartilage in studies assessing osteoarthritis disease progression may help improve the accuracy of clinical results.

9.2.2 Atlas based prospective registration of musculoskeletal MR images

Prospective registration is a useful tool to ensure consistent positioning between baseline and follow-up scans. However, a method to scan each individual in the same orientation at single time point would help improve the accuracy of clinical measurements between subjects. One approach to this would be to register a low

resolution scan to an atlas, an image information database obtained using imaging of many subjects which were scanned in the desired orientation. The rigid portion of the transform resulting from the registration to an atlas could then be used to prescribe the remainder of an exam. The difficulty in this approach is achieving an acceptable atlas and successful registration under the conditions of large anatomical variation present in the population. In particular, for individuals with gross anatomical differences in the shape of their bones due to osteophytes or boney growths. One option may be to select more than one atlas that represents different clinical groups.

9.2.3 Quantifying trabecular bone changes using non-rigid registration

While current longitudinal studies assessing trabecular structure average trabecular bone parameters within a particular region, it would be interesting to describe local trabecular structure changes. A non-rigid registration that results in a non-linear transformation between time points would help describe the changes in local structure. Deformation fields which show the mapping of each voxel from one time point to another may provide a more descriptive evaluation of temporal trends.

Bibliography

1. Siris ES, Miller PD, Barrett-Connor E, Faulkner KG, Wehren LE, Abbott TA, Berger ML, Santora AC, Sherwood LM. Identification and fracture outcomes of undiagnosed low bone mineral density in postmenopausal women: results from the National Osteoporosis Risk Assessment. Jama 2001;286(22):2815-2822.
2. US Department of Health and Human Services. Bone Health and Osteoporosis: A Report of the Surgeon General. US Department of Health and Human Services, Office of the Surgeon General 2004.
3. Kuehn BM. Better osteoporosis management a priority: impact predicted to soar with aging population. JAMA 2005;293(20):2453-2458.
4. World Health Organization. Assessment of fracture risk and its application to screening for postmenopausal osteoporosis. Report of a WHO Study Group. WHO Tech Rep Ser 1994;843:1–129.
5. Frost HM. Absorptiometry and "osteoporosis": problems. J Bone Miner Metab 2003;21(5):255-260.
6. Marshall D, Johnell O, Wedel H. Meta-analysis of how well measures of bone mineral density predict occurrence of osteoporotic fractures. BMJ 1996;312(7041):1254-1259.
7. Majumdar S, Genant HK, Grampp S, Newitt DC, Truong VH, Lin JC, Mathur A. Correlation of trabecular bone structure with age, bone mineral density, and osteoporotic status: in vivo studies in the distal radius using high resolution magnetic resonance imaging. J Bone Miner Res 1997;12(1):111-118.
8. Majumdar S, Newitt D, Jergas M, Gies A, Chiu E, Osman D, Keltner J, Keyak J, Genant H. Evaluation of technical factors affecting the quantification of trabecular bone structure using magnetic resonance imaging. Bone 1995;17(4):417-430.
9. Wehrli FW, Gomberg BR, Saha PK, Song HK, Hwang SN, Snyder PJ. Digital topological analysis of in vivo magnetic resonance microimages of trabecular bone reveals structural implications of osteoporosis. J Bone Miner Res 2001;16(8):1520-1531.
10. Wehrli FW, Hwang SN, Ma J, Song HK, Ford JC, Haddad JG. Cancellous bone volume and structure in the forearm: noninvasive assessment with MR microimaging and image processing. Radiology 1998;206(2):347-357.
11. Boutry N, Cortet B, Dubois P, Marchandise X, Cotten A. Trabecular bone structure of the calcaneus: preliminary in vivo MR imaging assessment in men with osteoporosis. Radiology 2003;227(3):708-717.
12. Chesnut CH, 3rd, Majumdar S, Newitt DC, Shields A, Van Pelt J, Laschansky E, Azria M, Kriegman A, Olson M, Eriksen EF, Mindeholm L. Effects of salmon calcitonin on trabecular microarchitecture as determined by magnetic resonance imaging: results from the QUEST study. J Bone Miner Res 2005;20(9):1548-1561.
13. Fraser WD. The burden of osteoporosis and the case for disease management. Disease Management and Health Outcomes 2004;12(6):409-418.
14. Gourlay M, Richy F, Reginster JY. Strategies for the prevention of hip fracture. Am J Med 2003;115(4):309-317.

15. Ettinger MP. Aging bone and osteoporosis: strategies for preventing fractures in the elderly. Arch Intern Med 2003;163(18):2237-2246.
16. Black DM, Cummings SR, Karpf DB, Cauley JA, Thompson DE, Nevitt MC, Bauer DC, Genant HK, Haskell WL, Marcus R, Ott SM, Torner JC, Quandt SA, Reiss TF, Ensrud KE. Randomised trial of effect of alendronate on risk of fracture in women with existing vertebral fractures. Fracture Intervention Trial Research Group. Lancet 1996;348(9041):1535-1541.
17. Cummings SR. How drugs decrease fracture risk: lessons from trials. J Musculoskelet Neuronal Interact 2002;2(3):198-200.
18. Beck TJ, Looker AC, Ruff CB, Sievanen H, Wahner HW. Structural trends in the aging femoral neck and proximal shaft: analysis of the Third National Health and Nutrition Examination Survey dual-energy X-ray absorptiometry data. J Bone Miner Res 2000;15(12):2297-2304.
19. Ciarelli MJ, Goldstein SA, Kuhn JL, Cody DD, Brown MB. Evaluation of orthogonal mechanical properties and density of human trabecular bone from the major metaphyseal regions with materials testing and computed tomography. J Orthop Res 1991;9(5):674-682.
20. Augat P, Reeb H, Claes LE. Prediction of fracture load at different skeletal sites by geometric properties of the cortical shell. J Bone Miner Res 1996;11(9):1356-1363.
21. Dempster DW, Lindsay R. Pathogenesis of osteoporosis. Lancet 1993;341(8848):797-801.
22. Kleerekoper M, Villanueva AR, Stanciu J, Rao DS, Parfitt AM. The role of three-dimensional trabecular microstructure in the pathogenesis of vertebral compression fractures. Calcif Tissue Int 1985;37(6):594-597.
23. Burstein AH, Reilly DT, Martens M. Aging of bone tissue: mechanical properties. J Bone Joint Surg Am 1976;58(1):82-86.
24. Jepsen KJ. The aging cortex: to crack or not to crack. Osteoporos Int 2003;14 Suppl 5:S57-62; discussion S63-66.
25. Genant HK, Gluer CC, Lotz JC. Gender differences in bone density, skeletal geometry, and fracture biomechanics. Radiology 1994;190(3):636-640.
26. Aguado F, Revilla M, Villa LF, Rico H. Cortical bone resorption in osteoporosis. Calcif Tissue Int 1997;60(4):323-326.
27. Greenspan SL, Beck TJ, Resnick NM, Bhattacharya R, Parker RA. Effect of hormone replacement, alendronate, or combination therapy on hip structural geometry: a 3-year, double-blind, placebo-controlled clinical trial. J Bone Miner Res 2005;20(9):1525-1532.
28. Roschger P, Rinnerthaler S, Yates J, Rodan GA, Fratzl P, Klaushofer K. Alendronate increases degree and uniformity of mineralization in cancellous bone and decreases the porosity in cortical bone of osteoporotic women. Bone 2001;29(2):185-191.
29. Rho JY, Roy ME, 2nd, Tsui TY, Pharr GM. Elastic properties of microstructural components of human bone tissue as measured by nanoindentation. J Biomed Mater Res 1999;45(1):48-54.

30. Courtney AC, Hayes WC, Gibson LJ. Age-related differences in post-yield damage in human cortical bone. Experiment and model. J Biomech 1996;29(11):1463-1471.
31. Boyce TM, Bloebaum RD. Cortical aging differences and fracture implications for the human femoral neck. Bone 1993;14(5):769-778.
32. Jaasma MJ, Bayraktar HH, Niebur GL, Keaveny TM. Biomechanical effects of intraspecimen variations in tissue modulus for trabecular bone. J Biomech 2002;35(2):237-246.
33. Meunier PJ, Boivin G. Bone mineral density reflects bone mass but also the degree of mineralization of bone: therapeutic implications. Bone 1997;21(5):373-377.
34. Muller R, Van Campenhout H, Van Damme B, Van Der Perre G, Dequeker J, Hildebrand T, Ruegsegger P. Morphometric analysis of human bone biopsies: a quantitative structural comparison of histological sections and micro-computed tomography. Bone 1998;23(1):59-66.
35. Ito M, Nakamura T, Matsumoto T, Tsurusaki K, Hayashi K. Analysis of trabecular microarchitecture of human iliac bone using microcomputed tomography in patients with hip arthrosis with or without vertebral fracture. Bone 1998;23(2):163-169.
36. Borah B, Ritman EL, Dufresne TE, Jorgensen SM, Liu S, Sacha J, Phipps RJ, Turner RT. The effect of risedronate on bone mineralization as measured by micro-computed tomography with synchrotron radiation: correlation to histomorphometric indices of turnover. Bone 2005;37(1):1-9.
37. Peyrin F, Salome M, Nuzzo S, Cloetens P, Laval-Jeantet AM, Baruchel J. Perspectives in three-dimensional analysis of bone samples using synchrotron radiation microtomography. Cell Mol Biol (Noisy-le-grand) 2000;46(6):1089-1102.
38. Muller R, Hahn M, Vogel M, Delling G, Ruegsegger P. Morphometric analysis of noninvasively assessed bone biopsies: comparison of high-resolution computed tomography and histologic sections. Bone 1996;18(3):215-220.
39. Muller R, Hildebrand T, Hauselmann HJ, Ruegsegger P. In vivo reproducibility of three-dimensional structural properties of noninvasive bone biopsies using 3D-pQCT. J Bone Miner Res 1996;11(11):1745-1750.
40. Fernandez-Seara MA, Wehrli SL, Wehrli FW. Diffusion of exchangeable water in cortical bone studied by nuclear magnetic resonance. Biophys J 2002;82(1 Pt 1):522-529.
41. Ma J, Wehrli FW, Song HK. Fast 3D large-angle spin-echo imaging (3D FLASE). Magn Reson Med 1996;35(6):903-910.
42. Krug R, Han ET, Banerjee S, Majumdar S. Fully balanced steady-state 3D-spin-echo (bSSSE) imaging at 3 Tesla. Magn Reson Med 2006;56(5):1033-1040.
43. Techawiboonwong A, Song HK, Magland JF, Saha PK, Wehrli FW. Implications of pulse sequence in structural imaging of trabecular bone. J Magn Reson Imaging 2005;22(5):647-655.
44. Banerjee S, Han ET, Krug R, Newitt DC, Majumdar S. Application of refocused steady-state free-precession methods at 1.5 and 3 T to in vivo high-resolution

MRI of trabecular bone: simulations and experiments. J Magn Reson Imaging 2005;21(6):818-825.
45. Hwang SN, Wehrli FW. Experimental evaluation of a surface charge method for computing the induced magnetic field in trabecular bone. J Magn Reson 1999;139(1):35-45.
46. Maintz JB, Viergever MA. A survey of medical image registration. Med Image Anal 1998;2(1):1-36.
47. Fitzpatrick J, Hill D, Maurer C. Image registration. Handbook of Medical Imaging, Vol 2:Medical Image Processing and Analysis: SPIE Press; 2000.
48. Knowlton R. Clinical applications of image registration. Handbook of Medical Imaging:Processing and Analysis. San Diego: Academic Press; 2000. p 613-622.
49. Ng L, Ibanez L. Medical Image Registration:Concepts and Implementation. Insight into Images. Wellesley, Massachusetts: A K Peters; 2004. p 239-306.
50. Mortenson M. Geometric Transformations for 3D Modeling. New York: Industrial Press Inc.; 2007.
51. Parker J, Kenyon R, Troxel D. Comparison of Interpolating Methods for Image Resampling. IEEE Trans Med Imaging 1983;MI-2(1):31-39.
52. Wolberg G. Digital Image Warping. New York: IEEE Computer Society Press; 1990.
53. Lehmann TM, Gonner C, Spitzer K. Survey: interpolation methods in medical image processing. IEEE Trans Med Imaging 1999;18(11):1049-1075.
54. Parrot RW, Stytz MR, Amburn P, Robinson D. Towards Statistically Optimal Interpolation for 3-D Medical Imaging. IEEE Engineering in Medicine and Biology 1993;12:49-59.
55. Thevenaz P, Unser M. Optimization of mutual information for multiresolution image registration. IEEE Trans Image Process 2000;9(12):2083-2099.
56. Studholme C, Hill DLG, Hawkes DJ. An Overlap Invariant Entropy Measure of 3D Medical Image Alignment. Pattern Recognition 1999;32(1):71-86.
57. Studholme C. Measures of 3D Medtical Image Alignment, PhD Dissertation: University of London; 1997.
58. Nocedal J, Wright S. Numerical Optimization. New York: Springer series in operations research: Springer-Verlag; 1999.
59. Press W, Flannery B, Teukolsky S, Vetterling W. Numerical Recipes in C. Cambridge: Cambridge University Press; 1992.
60. Chappard C, Basillais A, Benhamou L, Bonassie A, Brunet-Imbault B, Bonnet N, Peyrin F. Comparison of synchrotron radiation and conventional x-ray microcomputed tomography for assessing trabecular bone microarchitecture of human femoral heads. Med Phys 2006;33(9):3568-3577.
61. Ito M, Ejiri S, Jinnai H, Kono J, Ikeda S, Nishida A, Uesugi K, Yagi N, Tanaka M, Hayashi K. Bone structure and mineralization demonstrated using synchrotron radiation computed tomography (SR-CT) in animal models: preliminary findings. J Bone Miner Metab 2003;21(5):287-293.
62. Nuzzo S, Peyrin F, Cloetens P, Baruchel J, Boivin G. Quantification of the degree of mineralization of bone in three dimensions using synchrotron radiation microtomography. Med Phys 2002;29(11):2672-2681.

63. Kazakia GJ, Burghardt AJ, Cheung S, Majumdar S. Assessment of bone tissue mineralization by conventional x-ray microcomputed tomography: comparison with synchrotron radiation microcomputed tomography and ash measurements. Med Phys 2008;35(7):3170-3179.
64. Wells WM, 3rd, Viola P, Atsumi H, Nakajima S, Kikinis R. Multi-modal volume registration by maximization of mutual information. Med Image Anal 1996;1(1):35-51.
65. Maes F, Vandermeulen D, Suetens P. Comparative evaluation of multiresolution optimization strategies for multimodality image registration by maximization of mutual information. Med Image Anal 1999;3(4):373-386.
66. Studholme C. http://rview.colin-studholme.net
67. Koenderink JJ. The structure of images. Biol Cybern 1984;50(5):363-370.
68. Cooper DM, Thomas CD, Clement JG, Turinsky AL, Sensen CW, Hallgrimsson B. Age-dependent change in the 3D structure of cortical porosity at the human femoral midshaft. Bone 2007;40(4):957-965.
69. Bell KL, Loveridge N, Reeve J, Thomas CD, Feik SA, Clement JG. Super-osteons (remodeling clusters) in the cortex of the femoral shaft: influence of age and gender. Anat Rec 2001;264(4):378-386.
70. Bell KL, Loveridge N, Power J, Garrahan N, Meggitt BF, Reeve J. Regional differences in cortical porosity in the fractured femoral neck. Bone 1999;24(1):57-64.
71. Cooper DM, Turinsky AL, Sensen CW, Hallgrimsson B. Quantitative 3D analysis of the canal network in cortical bone by micro-computed tomography. Anat Rec B New Anat 2003;274(1):169-179.
72. Jordan GR, Loveridge N, Bell KL, Power J, Rushton N, Reeve J. Spatial clustering of remodeling osteons in the femoral neck cortex: a cause of weakness in hip fracture? Bone 2000;26(3):305-313.
73. Bell KL, Loveridge N, Jordan GR, Power J, Constant CR, Reeve J. A novel mechanism for induction of increased cortical porosity in cases of intracapsular hip fracture. Bone 2000;27(2):297-304.
74. Power J, Loveridge N, Lyon A, Rushton N, Parker M, Reeve J. Osteoclastic cortical erosion as a determinant of subperiosteal osteoblastic bone formation in the femoral neck's response to BMU imbalance. Effects of stance-related loading and hip fracture. Osteoporos Int 2005;16(9):1049-1056.
75. Martin RB, Pickett JC, Zinaich S. Studies of skeletal remodeling in aging men. Clin Orthop Relat Res 1980(149):268-282.
76. Yeni YN, Brown CU, Wang Z, Norman TL. The influence of bone morphology on fracture toughness of the human femur and tibia. Bone 1997;21(5):453-459.
77. Currey JD. The effect of porosity and mineral content on the Young's modulus of elasticity of compact bone. J Biomech 1988;21(2):131-139.
78. Schaffler MB, Burr DB. Stiffness of compact bone: effects of porosity and density. J Biomech 1988;21(1):13-16.
79. McCalden RW, McGeough JA, Barker MB, Court-Brown CM. Age-related changes in the tensile properties of cortical bone. The relative importance of changes in porosity, mineralization, and microstructure. J Bone Joint Surg Am 1993;75(8):1193-1205.

80. Kasra M, Grynpas MD. Static and dynamic finite element analyses of an idealized structural model of vertebral trabecular bone. J Biomech Eng 1998;120(2):267-272.
81. Ochoa JA, Heck DA, Brandt KD, Hillberry BM. The effect of intertrabecular fluid on femoral head mechanics. J Rheumatol 1991;18(4):580-584.
82. Kasra M, Grynpas MD. On shear properties of trabecular bone under torsional loading: effects of bone marrow and strain rate. J Biomech 2007;40(13):2898-2903.
83. Liebschner MA, Keller TS. Hydraulic strengthening affects the stiffness and strength of cortical bone. Ann Biomed Eng 2005;33(1):26-38.
84. Cowin SC. Bone poroelasticity. J Biomech 1999;32(3):217-238.
85. Liebschner MA, Keller TS. The importance of permeability constand in hydraulic strengthening of cortical bone. 1999; ASME Summer Bioengineering Conference. Big Sky, Montana.
86. Kazakia GJ, Hyun B, Burghardt AJ, Krug R, Newitt DC, de Papp AE, Link TM, Majumdar S. In vivo determination of bone structure in postmenopausal women: a comparison of HR-pQCT and high-field MR imaging. J Bone Miner Res 2008;23(4):463-474.
87. Buie HR, Campbell GM, Klinck RJ, MacNeil JA, Boyd SK. Automatic segmentation of cortical and trabecular compartments based on a dual threshold technique for in vivo micro-CT bone analysis. Bone 2007;41(4):505-515.
88. Organization WH. Assement of fracture risk and its application to screening for postmenopausal osteoporosis. Report of a WHO Study Group. WHO Tech Rep Ser 1994.
89. Viola P, Wells WM. Alignment by maximization of mutual information. Int JourComp Vis 1997;24(2):137-154.
90. Maes F, Collignon A, Vandermeulen D, Marchal G, Suetens P. Multimodality image registration by maximization of mutual information. IEEE Trans Med Imaging 1997;16(2):187-198.
91. Studholme C, Hill DL, Hawkes DJ. Automated three-dimensional registration of magnetic resonance and positron emission tomography brain images by multiresolution optimization of voxel similarity measures. Med Phys 1997;24(1):25-35.
92. Laib A, Hauselmann HJ, Ruegsegger P. In vivo high resolution 3D-QCT of the human forearm. Technol Health Care 1998;6(5-6):329-337.
93. Davis KA, Burghardt AJ, Link TM, Majumdar S. The effects of geometric and threshold definitions on cortical bone metrics assessed by in vivo high-resolution peripheral quantitative computed tomography. Calcif Tissue Int 2007;81(5):364-371.
94. Vincent L. Morphological grayscale reconstruction in image analysis: applications and efficient algorithms. IEEE Trans Image Process 1993;2(2):176-201.
95. Newitt DC, Van Rietbergen B, Majumdar S. Processing and Analysis of In Vivo High-Resolution MR Images of Trabecular Bone for Longitudinal Studies: Reproducibility of Structural Measures and Micro-Finite Element Analysis Derived Mechanical Properties. Osteoporos Int 2002;13:278-287.

96. Reilly GC, Knapp HF, Stemmer A, Niederer P, Knothe Tate ML. Investigation of the morphology of the lacunocanalicular system of cortical bone using atomic force microscopy. Ann Biomed Eng 2001;29(12):1074-1081.
97. McCreadie BR, Hollister SJ, Schaffler MB, Goldstein SA. Osteocyte lacuna size and shape in women with and without osteoporotic fracture. J Biomech 2004;37(4):563-572.
98. Cummings SR, Black DM, Thompson DE, Applegate WB, Barrett-Connor E, Musliner TA, Palermo L, Prineas R, Rubin SM, Scott JC, Vogt T, Wallace R, Yates AJ, LaCroix AZ. Effect of alendronate on risk of fracture in women with low bone density but without vertebral fractures: results from the Fracture Intervention Trial. JAMA 1998;280(24):2077-2082.
99. Iwamoto J, Sato Y, Takeda T, Matsumoto H. Hip fracture protection by alendronate treatment in postmenopausal women with osteoporosis: a review of the literature. Clin Interv Aging 2008;3(3):483-489.
100. Liberman UA, Weiss SR, Broll J, Minne HW, Quan H, Bell NH, Rodriguez-Portales J, Downs RW, Jr., Dequeker J, Favus M. Effect of oral alendronate on bone mineral density and the incidence of fractures in postmenopausal osteoporosis. The Alendronate Phase III Osteoporosis Treatment Study Group. N Engl J Med 1995;333(22):1437-1443.
101. Borah B, Dufresne T, Nurre J, Chmielewski P, Phipps R, Wagner L, Bouxsein M, Zebaze R, Seeman E. Risedronate reduces intracortical porosity in women with osteoporosis. 2009; European Calcified Tissue Society. Vienna, Austria.
102. Neuman WF, Neuman MW. The Chemical Dynamics of Bone. Chicago: University of Chicago Press; 1958.
103. Trabowitz S, Davis S. The bone marrow matnix. . In: CRC, editor. The human bone marrow: anatomy, physiology, and pathophysiology Boca Raton, Fla; 1982. p 43-76.
104. Piney A. The anatomy of the bone marrow. BMJ 1922;2:792-795.
105. Mitchell DG, Rao VM, Dalinka M, Spritzer CE, Axel L, Gefter W, Kricun M, Steinberg ME, Kressel HY. Hematopoietic and fatty bone marrow distribution in the normal and ischemic hip: new observations with 1.5-T MR imaging. Radiology 1986;161(1):199-202.
106. Vogler JB, 3rd, Murphy WA. Bone marrow imaging. Radiology 1988;168(3):679-693.
107. Vande Berg BC, Malghem J, Lecouvet FE, Maldague B. Magnetic resonance imaging of the normal bone marrow. Skeletal Radiol 1998;27(9):471-483.
108. Yeung DK, Griffith JF, Antonio GE, Lee FK, Woo J, Leung PC. Osteoporosis is associated with increased marrow fat content and decreased marrow fat unsaturation: a proton MR spectroscopy study. J Magn Reson Imaging 2005;22(2):279-285.
109. Liney GP, Bernard CP, Manton DJ, Turnbull LW, Langton CM. Age, gender, and skeletal variation in bone marrow composition: a preliminary study at 3.0 Tesla. J Magn Reson Imaging 2007;26(3):787-793.
110. Robson MD, Gatehouse PD, Bydder M, Bydder GM. Magnetic resonance: an introduction to ultrashort TE (UTE) imaging. J Comput Assist Tomogr 2003;27(6):825-846.

111. Holmes JE, Bydder GM. MR imaging with ultrashort TE (UTE) pulse sequences: Basic principles. Radiography 2005;11:163-174.
112. Bell KL, Loveridge N, Power J, Garrahan N, Stanton M, Lunt M, Meggitt BF, Reeve J. Structure of the femoral neck in hip fracture: cortical bone loss in the inferoanterior to superoposterior axis. J Bone Miner Res 1999;14(1):111-119.
113. Feik SA, Thomas CD, Clement JG. Age-related changes in cortical porosity of the midshaft of the human femur. J Anat 1997;191 (Pt 3):407-416.
114. Thomas CD, Feik SA, Clement JG. Regional variation of intracortical porosity in the midshaft of the human femur: age and sex differences. J Anat 2005;206(2):115-125.
115. Bousson V, Meunier A, Bergot C, Vicaut E, Rocha MA, Morais MH, Laval-Jeantet AM, Laredo JD. Distribution of intracortical porosity in human midfemoral cortex by age and gender. J Bone Miner Res 2001;16(7):1308-1317.
116. Cummings SR, Melton LJ. Epidemiology and outcomes of osteoporotic fractures. Lancet 2002;359(9319):1761-1767.
117. Assessment of fracture risk and its application to screening for postmenopausal osteoporosis. Report of a WHO Study Group. World Health Organ Tech Rep Ser 1994;843:1-129.
118. Krug R, Banerjee S, Han ET, Newitt DC, Link TM, Majumdar S. Feasibility of in vivo structural analysis of high-resolution magnetic resonance images of the proximal femur. Osteoporos Int 2005;16(11):1307-1314.
119. Carpenter D, al. e. Analyzing Trabecular Bone Structure in the Proximal Femur with High-Resolution Parallel Magnetic Resonance Imaging. International Bone Densitometry Workshop, Kyoto, Japan 2006.
120. Gomberg BR, Wehrli FW, Vasilic B, Weening RH, Saha PK, Song HK, Wright AC. Reproducibility and error sources of micro-MRI-based trabecular bone structural parameters of the distal radius and tibia. Bone 2004;35(1):266-276.
121. Takao M, Sugano N, Nishii T, Tanaka H, Masumoto J, Miki H, Sato Y, Tamura S, Yoshikawa H. Application of three-dimensional magnetic resonance image registration for monitoring hip joint diseases. Magn Reson Imaging 2005;23(5):665-670.
122. Magland J, Vasilic B, Lin W, Wehrli FW. Automatic 3D Registration of Trabecular bone images using a collection of regional 2D registrations. Proceedings of the 14th International Society of Magnetic Resonance Medicine 2006.
123. Hancu I, Blezek DJ, Dumoulin MC. Automatic repositioning of single voxels in longitudinal 1H MRS studies. NMR Biomed 2005;18(6):352-361.
124. Blumenfeld J, Carballido-Gamio J, Krug R, Blezek DJ, Hancu I, Majumdar S. Automatic prospective registration of high-resolution trabecular bone images of the tibia. Ann Biomed Eng 2007;35(11):1924-1931.
125. Rajapakse CS, Magland JF, Wehrli FW. Fast prospective registration of in vivo MR images of trabecular bone microstructure in longitudinal studies. Magn Reson Med 2008;59(5):1120-1126.
126. Banerjee S, Choudhury S, Han ET, Brau AC, Morze CV, Vigneron DB, Majumdar S. Autocalibrating parallel imaging of in vivo trabecular bone microarchitecture at 3 Tesla. Magn Reson Med 2006;56(5):1075-1084.

127. Insight Toolkit, http://www.itk.org/.
128. Thévenaz P, Blu T, Unser M. Image Interpolation and Resampling. Handbook of Medical Imaging, Processing and Analysis. San Diego Ca, USA: Academic Press; 2000. p 393-420.
129. Majumdar S, Genant HK. Assessment of trabecular structure using high resolution magnetic resonance imaging. Stud Health Technol Inform 1997;40:81-96.
130. Gluer CC, Blake G, Lu Y, Blunt BA, Jergas M, Genant HK. Accurate assessment of precision errors: how to measure the reproducibility of bone densitometry techniques. Osteoporos Int 1995;5(4):262-270.
131. Brown TD, Ferguson AB, Jr. Mechanical property distributions in the cancellous bone of the human proximal femur. Acta Orthop Scand 1980;51(3):429-437.
132. Nazarian A, Muller J, Zurakowski D, Muller R, Snyder BD. Densitometric, morphometric and mechanical distributions in the human proximal femur. J Biomech 2007;40(11):2573-2579.
133. Morgan EF, Keaveny TM. Dependence of yield strain of human trabecular bone on anatomic site. J Biomech 2001;34(5):569-577.
134. Issever AS, Vieth V, Lotter A, Meier N, Laib A, Newitt D, Majumdar S, Link TM. Local differences in the trabecular bone structure of the proximal femur depicted with high-spatial-resolution MR imaging and multisection CT. Acad Radiol 2002;9(12):1395-1406.
135. Link TM, Vieth V, Langenberg R, Meier N, Lotter A, Newitt D, Majumdar S. Structure analysis of high resolution magnetic resonance imaging of the proximal femur: in vitro correlation with biomechanical strength and BMD. Calcif Tissue Int 2003;72(2):156-165.
136. Blumenfeld J, Studholme C, Carballido-Gamio J, Carpenter D, Link TM, Majumdar S. Three-dimensional image registration of MR proximal femur images for the analysis of trabecular bone parameters. Med Phys 2008;35(10):4630-4639.
137. Folkesson J, Krug R, Goldenstein J, Issever A, Fang C, Link T, Majumdar S. Evaluation of correction methods for coil-induced intensity inhomogeneities and their influence on trabecular bone structure parameters from MR images. Med Phys 2008;36(4):1267-1274
138. Chu W-J ea. Reproducibility of 1H Spectroscopic Imaging of the Human Hippocampus. 2004.
139. Hartmann SL, Dawant BM, Parks MH, Schlack H, Martin PR. Image-guided MR spectroscopy volume of interest localization for longitudinal studies. Comput Med Imaging Graph 1998;22(6):453-461.
140. Gedat E, Braun J, Sack I, Bernarding J. Prospective registration of human head magnetic resonance images for reproducible slice positioning using localizer images. J Magn Reson Imaging 2004;20(4):581-587.
141. Itti L, Chang L, Ernst T. Automatic scan prescription for brain MRI. Magn Reson Med 2001;45(3):486-494.
142. Benner T, Wisco JJ, van der Kouwe AJ, Fischl B, Vangel MG, Hochberg FH, Sorensen AG. Comparison of Manual and Automatic Section Positioning of Brain MR Images. Radiology 2006;239(246-254).

143. van der Kouwe AJ, Benner T, Fischl B, Schmitt F, Salat DH, Harder M, Sorensen AG, Dale AM. On-line automatic slice positioning for brain MR imaging. Neuroimage 2005;27(1):220-230.
144. Magland J, Vasilic B, Lin W, Wehrli FW. Automatic 3D Registration of Trabecular Bone Images Using a Collection of Regional 2D Registrations. Proceedings of the 14th International Society of Magnetic Resonance Medicine 2006.
145. Atkinson K. An Introduction to Numerical Analysis. Chichester: Wiley; 1989.
146. Bangerter NK, Hargreaves BA, Vasanawala SS, Pauly JM, Gold GE, Nishimura DG. Analysis of multiple-acquisition SSFP. Magn Reson Med 2004;51(5):1038-1047.
147. Glantz SA. Primer of Bio-Statistics. United States of America: McGraw-Hill Companies, Inc.; 1997.
148. Rizzo G, Pasquali P, Gilardi MC, Cerutti S, Bettinardi V, Lucignani G, Scotti G, Fazio F. Multimodality biomedical image integration: use of a cross-correlation technique.; 1991. p 219-220.
149. Woods RP, Grafton ST, Holmes CJ, Cherry SR, Mazziotta JC. Automated image registration: I. General methods and intrasubject, intramodality validation. J Comput Assist Tomogr 1998;22:141-154.
150. Carpenter D, Krug R, Banerjee S, Majumdar S. Analyzing Trabecular Bone Structure in the Proximal Femur with High-Resolution Parallel Magnetic Resonance Imaging. International Bone Densitometry Workshop, Kyoto, Japan 2006.
151. Itti L, Chang L, Ernst T. Automatic scan prescription for brain MRI. Magn Reson Med 2001;45(3):486-494.
152. Gedat E, Braun J, Sack I, Bernarding J. Prospective registration of human head magnetic resonance images for reproducible slice positioning using localizer images. J Magn Reson Imaging 2004;20(4):581-587.
153. van der Kouwe AJ, Benner T, Fischl B, Schmitt F, Salat DH, Harder M, Sorensen AG, Dale AM. On-line automatic slice positioning for brain MR imaging. Neuroimage 2005;27(1):222-230.
154. Lecouvet FE, Claus J, Schmitz P, Denolin V, Bos C, Vande Berg BC. Clinical evaluation of automated scan prescription of knee MR images. J Magn Reson Imaging 2009;29(1):141-145.
155. Bystrov D, Pekar V, Young S, Dries S, Heese H, Muiswinkel A. Automated Planning of MRI Scans of the Knee Joint. 2007. Proc SPIE Medical Imaging. p 6144-6158.

Publishing Agreement

It is the policy of the University to encourage the distribution of all theses, dissertations, and manuscripts. Copies of all UCSF theses, dissertations, and manuscripts will be routed to the library via the Graduate Division. The library will make all theses, dissertations, and manuscripts accessible to the public and will preserve these to the best of their abilities, in perpetuity.

Please sign the following statement:

I hereby grant permission to the Graduate Division of the University of California, San Francisco to release copies of my thesis, dissertation, or manuscript to the Campus Library to provide access and preservation, in whole or in part, in perpetuity.

Janet Goldstein 10/19/2009

Author Signature Date